Development of Calix[4]arene-Functionalized Microcantilever Array Sensing System for the Rapid, Sensitive and Simultaneous Detection of Metal Ions in Aqueous Solutions

By

© Abdullah Alodhayb

A thesis submitted to the School of Graduate Studies

in partial fulfillment of the requirements for the degree of

Doctor of Philosophy

Department of Physics and Physical Oceanography

Memorial University of Newfoundland

March, 2016

St. John's Newfoundland

Dedication

To my Mother and Father

To my wife Norah

To my son Nasser

To my daughter Alreem

To my brothers and sisters

Abstract

The work described in this thesis was conducted with the aim of: 1) investigating the binding capabilities of calix[4]arene-functionalized microcantilevers towards specific metal ions and 2) developing a new16-microcantilever array sensing system for the rapid, and simultaneous detection of metal ions in fresh water.

Part I of this thesis reports on the use of three new bimodal calix[4]arenes (methoxy, ethoxy and crown) as potential host/guest sensing layers for detecting selected ions in dilute aqueous solutions using single microcantilever experimental system. In this work it was shown that modifying the upper rim of the calix[4]arenes with a thioacetate end group allow calix[4]arenes to self-assemble on Au(111) forming complete highly ordered monolayers. It was also found that incubating the microcantilevers coated with 5 nm of Inconel and 40 nm of Au for 1 h in a 1.0 M solution of calix[4]arene produced the highest sensitivity. Methoxy-functionalized microcantilevers showed a definite preference for Ca^{2+} ions over other cationic guests and were able to detect trace concentration as low as 10^{-12} M in aqueous solutions. Microcantilevers modified with ethoxy calix[4]arene displayed their highest sensitivity towards Sr^{2+} and to a lesser extent Ca^{2+} ions. Crown calix[4]arene-modified microcantilevers were however found to bind selectively towards Cs^{+} ions. In addition, the counter anion was also found to contribute to the deflection. For example methoxy calix[4]arene-modified microcantilever was found to be more sensitive to $CaCl_2$ over other water-soluble calcium salts such as $Ca(NO_3)_2$, $CaBr_2$ and

CaI_2. These findings suggest that the response of calix[4]arene-modified microcantilevers should be attributed to the target ionic species as a whole instead of only considering the specific cation and/or anion.

Part II presents the development of a 16-microcantilever sensor setup. The implementation of this system involved the creation of data analysis software that incorporates data from the motorized actuator and a two-axis photosensitive detector to obtain the deflection signal originating from each individual microcantilever in the array. The system was shown to be capable of simultaneous measurements of multiple microcantilevers with different coatings. A functionalization unit was also developed that allows four microcantilevers in the array to be coated with an individual sensing layer one at the time. Because of the variability of the spring constants of different cantilevers within the array, results presented were quoted in units of surface stress unit in order to compare values between the microcantilevers in the array.

Acknowledgements

I would first like to express my sincere appreciation and gratitude to my supervisor Dr. Luc Beaulieu for giving me the opportunity to work on this interesting project. His continuous support, enthusiasm, and understanding have greatly contributed to the completion of this thesis. This work would not have been completed without his intellectual and insightful guidance.

My appreciation and immeasurable thanks are also extended to our collaborator, Dr. Paris Georghiou's group in the Chemistry Department at Memorial University. Without their contribution, this work would have been difficult to complete. I would especially like to thank Dr. Paris Georghiou and Dr. Shofiur Rahman to whom I will be forever indebted for countless hours of stimulating and fruitful discussions.

While working in this project, I was fortunate to meet and work with many motivated and cooperative colleagues and lab-mates. In particular, I am grateful to Hanin Algaidi, Mona Braim, Dr. Saydur Rhaman and Suhad Sbeih for their support and discussions. They made my experience as a graduate student enjoyable and rewarding.

I would also like to thank my supervisory committee, Dr. Kristin Poduska and Dr. Qiying Chen for reading my thesis and providing valuable suggestions.

Many thanks also go to Joy Simmons and Dr. Todd Andrews for all of their great efforts to help graduate students to succeed by answering students'a questions and help them to

focus on their studies. Gordon Whelan is also thanked for his hard work in machining my experimental design.

I must also acknowledge the financial support by the ministry of Education in Saudi Arabia through the scholarship. The Saudi Cultural Bureau in Canada is also greatly appreciated for their support to students.

Finally, there are many friends to thank for their continual support and encouragement which have a great impact on my success in my PhD studies. My deepest appreciation and thanks to Abdulaziz Alanazi, Saad Alanazi, Zead Alfaiz, Hamad Alkuraiji, Jamal Alnofiy, Mahmood Aljabri, Ayad Aljohani, Hamza Algaidi, Mohammed Alqashami, Majed Sager, Hadi Alsharmmah, Ali Albukytan, Mohammed Alodhayb, Majed Alodhayb, Mefli Rasheedi and Waleed Almuriri. For those who are not listed, you are always on my mind and your support is always appreciated.

Table of Contents

List of Symbols and Acronyms

MEMS: Microelectromechanical systems.

PSD: position sensitive detector (PSD).

μm: Micrometers = 10^{-6} meters.

nm: Nanometers = 10^{-9} meters.

N/m: Newtons per meter.

kHz: kilohertz.

DNA: Deoxyribonucleic acid.

SAM: Self assembled monolayer.

S : The PSD signal.

σ_{ij}: Surface stress tensor.

γ: Surface energy.

ε_{ij}: Elastic strain tensor.

δ_{ij}: The Kronecker delta.

$\Delta\sigma$: Change in surface stress.

δ: Deflection of the microcantilever.

E : Young's modulus.

υ : Poisson's ratio.

t : Microcantilever thickness.

L : Microcantilever thickness.

σ_f: Film stress.

t_f: Film thickness.

M_f: Bending moment on the film.

M_s: Bending moment on the substrate

b_f: Film width.

t_s: Substrate thickness.

R: The radius of the curvature of the microcantilever.

E^* : The effective (biaxial) modulus.

Δh : The beam displacement on the PSD surface.

θ: The deflection angle of the laser beam.

$\emptyset$: The deflection angle of the microcantilever.

s : The distance between the microcantilever and the PSD.

l : The effective length of the PSD.

n_s : The refractive index of the solution.

n_g : The refractive index of the solution.

φ : The angle of incidence of the light beam.

d_a : The distance between the microcantilever beam and the inner glass.

d_s : The distance between the outer glass surface and the PSD.

d_g : The thickness of the glass window.

RMS: Root mean square.

K : Complexation constant.

List of Figures

List of Tables

Chapter 1 Introduction and Background

The rapid developments in many of life aspects through industrial and agricultural activities have greatly contributed to the improvement of human life. These developments have however altered the environmental stability by introducing pollutants and contaminants into the environment. The health hazards associated with the presence of these pollutants in the environment has caused a growing global concern about the safety of living organisms in our ecosystems. Fortunately, this concern has led to extensive efforts towards developing methods and devices that can effectively play a crucial role in environmental monitoring. One significant environmental consideration is the health of our water systems, and especially freshwater supplies which are required to be clean and as free of pollutants as possible. The accurate determination of the constituents of water is a key aspect of environmental monitoring and is of fundamental importance for both humans and the environment. One class of water contaminants is heavy metal ions (e.g. Pb^{2+}, Cd^{2}, Zn^{2+}, Hg^{2+}, Cu^{2+}, Fe^{2+}) whose presence in fresh water is a concern due to their toxicity to humans and aquatic life forms [1,2]. Their ability to bioaccumulate and form complexes have also contributed to the cause for concern [3]. Heavy metal ions are introduced into the environment by either natural or anthropogenic means such as volcanic activities, waste dumping, industrial activities, and agricultural chemical run offs [4]**.** Mining of heavy metals has progressively increased the presence of heavy metals in the environment [5]. While some of these metals such as Fe and Zn are essential for the functionality of the human body, other heavy metals such as Pb and Cd

are hazardous even at low concentrations [6]. Human exposure to heavy metals can occur by several routes including consumption, inhalation and skin contact. It has been long confirmed that the presence of heavy metals with excessive levels in freshwater sources could result in harmful effects to both aquatic organisms and human health. Several diseases and disorders such as diarrhea, psychosis and kidney dysfunction have been reported to be causes by exposure or consumption of heavy metals beyond tolerance limits [5]. The occurrence of these diseases is attributed to the fact that the intake of heavy metals into the human body and aquatic organisms leads to a change of the biochemistry and metabolism of the body by forming stable chemical bonds with the body's biomolecules such as proteins [2]. The formation of such bonds results in the malfunctioning of the body's biomolecules which can consequently lead to the creation of diseases and disorders [5]. Toxicological effects of these metal ions depend on their concentration, their interaction with other species in the ecosystem, as well as their chemical properties [7]. Although the aforementioned statements emphasized the importance of monitoring and detecting heavy metals, the detection of other non-heavy metals such as Calcium is also significant for environmental and clinical applications [8,9]. As a result, much research has been devoted to developing sensitive, selective and reliable methods and techniques for detecting trace concentrations of metal ions in water [10-12]. As will be discussed in the following section, the current methodologies for detecting metal ions in fresh water are expensive, time-consuming, and potentially prone to errors. The development of alternative techniques which can offer sensitive, low cost, reliable, in-situ and portable detection of metals in fresh water is thus sought.

1.1 Current Approaches for Detection of Metal Ions in Water Samples

The presence of toxic metals in water supplies poses serious concerns to humans and the environment making their detection and determination crucial. There are several quantitative methods that have been used for the detection and analysis of metal ions in fresh water. The most common and widely used conventional techniques are atomic absorption spectroscopy [13], inductively coupled plasma optical emission spectrometry [14], laser induced breakdown spectroscopy [15], X–ray absorption spectroscopy [16], as well as anodic stripping voltammetry [10]. Among these detection methods, atomic absorption spectroscopy (AAS) is a well-established and powerful analytical technique which has been shown to quantify over 60 elements in both solution and solid samples [13]. These laboratory-based techniques are sensitive and have low detection limits [17]. Despite their excellent sensitivity, these techniques suffer several disadvantages and drawbacks. The requirement of long and tedious sample preparation procedure is one of these drawbacks. Collected samples are often subjected to a series of treatment and calibration procedures before being tested which is time-consuming and require skilled and trained professionals [18]. These techniques are also expensive, sophisticated and lack *in-situ* analysis capabilities [19]. The limitations associated with current methods necessitate the need of adopting alternative techniques that are simple to operate and can provide real time, *in-situ* detection of metal ions in fresh water. Recent developments have witnessed the employment of sensing-based techniques in the hopes of satisfying the aforementioned desirable proprieties for the detection of metal ions [11,19,20]. The

use of some of these sensing devices in the detection of heavy metals relies on the immobilization of highly selective recognizing elements such as macrocyclic compounds [21], organic chelators [22], and proteins [11] on the sensor's surface. The subsequent interactions between the recognition molecules with the target analyte are then transduced into an electrical, mechanical, or optical signal. An overview of the recent applications of sensing technologies used in the detection of metal ions is outlined in the following section.

1.2 Chemical Sensors

The term sensor is very broad and can be used to describe many different devices, depending on the application of interest. Sensors can be classified into different types based on either the type of recognition layer and transduction mechanism or type of parameters to be measured by the sensor device [24]. Such broad classification has led to the generation of many types of sensors such as biological sensors (e.g. enzyme biosensors), physical sensors (e.g. temperature sensors), and proximity sensors. The classification of sensors is diverse but the uniting factor of all these classifications is the use of the recognition element and the transducer to generate a signal. In general, a sensor is defined as an analytical device that generates a useful processable signal (e.g. optical or electrical), in response to the input stimuli. Sensors can be biologically or chemically modified with a recognition element (e.g. antibodies, enzymes or macrocyclic compounds) so that they can be used for the detection and analysis of the target stimulus

(e.g. antigen, bacteria or metal ions). Sensors consist of two main components: a recognition element and a transducer. A schematic representation of the key elements of a sensor is shown in Figure 1.1. The recognition element is the component on which the interactions between receptor and the target molecules take place. The main role of the recognition layer is to provide binding sites for the analyte of interest. The transducer, which is in intimate contact with the recognition element, converts the binding or interactions events on the recognition element into a measurable signal, such as a current and/or a voltage. Such signals are often detected and processed by means of electronics or computer software. One of the earliest reported and commercialized forms of sensors is enzyme-based sensors, used to measure the concentration of glucose in fluid [23]. In this sensor, the enzyme glucose oxidase is immobilized onto a polarographic oxygen electrode and the detection is based on an amperometric transducing mechanism. This type of sensor is an excellent example of a commercially available sensor showing how the coupling between an appropriate recognition element and transducer results in a successful and useful device.

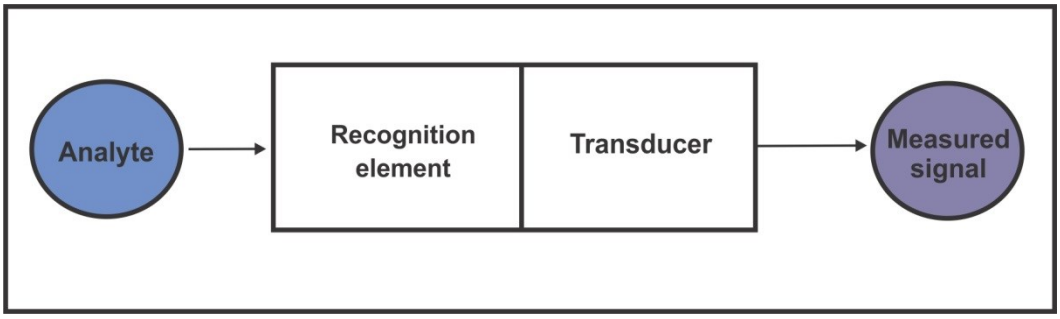

Figure 1.1: A schematic representation of the structure of a sensor.

The transduction mechanism of sensors is based on four common methods, namely electrochemical, optical, thermal and piezoelectric [24]. In electrochemical sensors, the chemical recognition element is coupled into an electrode transducer. Electrochemical transducers transfer the chemical events into an electrical signal either current (amperometric) or potential (potentiometric). These resulting signals are proportionally related to the concentration of the analyte. Nomngongo *et al.* [25] developed an enzyme-modified amperometric sensing device for the detection of the heavy metals cadmium, lead and copper with very high sensitivity. For optical sensors, the underlying principle is that the optical properties such as fluorescence and absorbance change in response to the interactions between the recognition layer and the target analytes. The detection of signal changes is often accomplished by using a semiconductor photodiode, after which the optical signal is transformed into an electrical one. The employment of optical sensors for fast and cost-efficient measurements of heavy metal has been recently witnessed [26]. In thermal sensors, a thermistor is utilized as a transducer which undergoes a change in temperature upon receptor-analyte interactions. Piezoelectric sensors function by making use of the piezoelectric principle, in which the anisotropic crystals such as quartz produce an electrical signal upon applying a mechanical stress and vice versa. The binding of target analyte to the receptor's binding sites cause a change in mass which consequently changes the resonant frequency. Measurements of the frequency change are then used for analyzing the binding events. Huang *et al.* [27] reported on the construction of a melanin-coated piezoelectric sensor for the real-time detection of metal ions with enhanced sensitivity.

Despite the presence of several analytical instruments and devices, the exciting opportunities that sensors offer have directed much research towards the development of metal ion detectors based on sensing technology. The interdisciplinary nature of research into sensors has brought together expertise from a diverse range of scientific disciplines such as chemistry, physics, biochemistry, biology and engineering. This has led to the rapid enhancement in sensing technology and to the employment of sensors in a wide range of applications in vastly different fields including medical diagnostics, environmental surveillance, food industry and the pharmaceutical industry [28,29].

The continuing development of sensing technology has also led to the emergence of a new class of sensors called microelectromechanical systems (MEMS). In these systems, microfabrication technology is exploited for the generation of miniaturized devices on which micromechanical and electrical components are integrated [30]. This technology is also often referred to as lab-on-a chip systems due to the integration of all of the MEMS components into a small chip, often silicon chips. The fabrication of MEMS devices and structures is performed using integrated circuits (IC) fabrication techniques including etching, deposition and lithography [31]. MEMS structures are primarily made of silicon but other materials such as polymer, glass and quartz may be used in fabricating such devices. The employment of micromachining technology in the production of MEMS devices has inspired numerous researchers to work on developing and introducing inexpensive, small in size and efficient technologies into the market [31]. One MEMS-based detection platform which has significantly benefited from the

unprecedented advancement in microfabrication and miniaturization technology is *microcantilever sensors*.

1.3 Microcantilever Sensors

The realization of the possibility of using microcantilevers as versatile sensing tools was observed during AFM experiments, in which microcantilevers are used for probing surface properties. The advent of the atomic force microscopy (AFM) has revolutionized the way materials are imaged and ultimately led to the use of microcantilevers as transducers capable of detecting numerous chemical and physical phenomena [32,33]. Unlike AFM cantilevers which have a tip used to image the sample, microcantilever sensors are tipless. As demonstrated in Figure 1.2, microcantilevers are free standing beams held at one end and free at the other. They are typically formed in either a rectangular or V-shape and can be fabricated from silicon, silicon nitride or polymers. Due to its desirable electrical and mechanical properties [34], silicon has been extensively applied in the construction of MEMS devices and particularly microcantilevers. An important feature of silicon is that it allows the fabrication of structures with precise dimensions, which have a key influence on the microcantilever sensitivity. For example, thin and long microcantilevers have greater sensitivity than thicker and smaller counterparts.

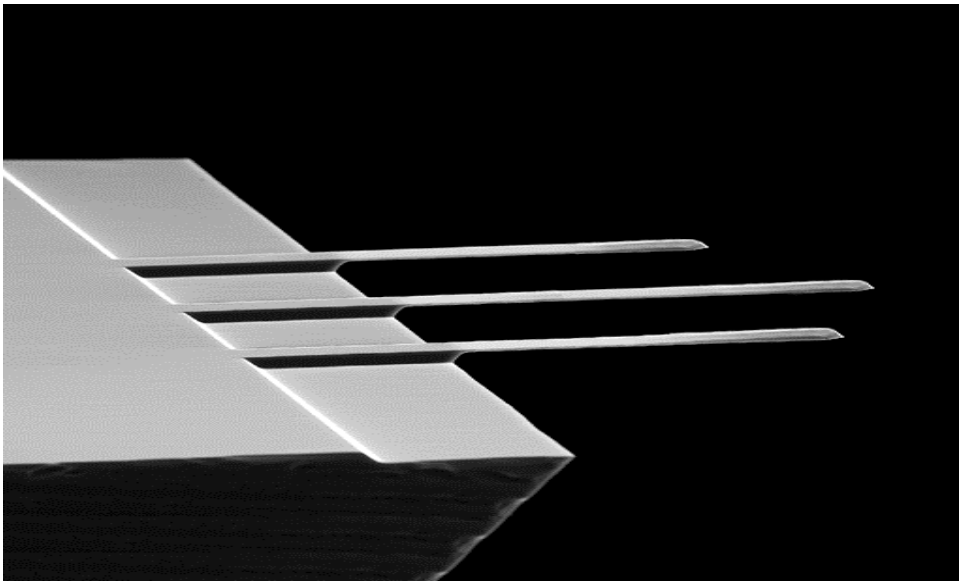

Figure 1.2: An SEM image of a microcantilever sensor. [Reprinted with permission from MikroMasch].

The process of fabricating silicon microcantilevers is often accomplished using either bulk or surface micromachining [35]. The difference between these two fabrication methods is the way the microcantilever beam is realized. The final microcantilever structure is constructed in the former method by etching the silicon substrate whereas in the latter method, the layers deposited on top of the silicon substrate are etched. The bulk micromachining method (depicted in Figure 1.3), with which silicon-based microcantilevers are typically fabricated, encompasses three main steps: preparation of the substrate, patterning of the microcantilever, and release of the device. Substrate preparation includes the deposition of the material composing the microcantilever (e.g. Si) on a sacrificial layer (e.g. silicon wafer). The final thickness of the microcantilever is determined by the thickness of the silicon layer on the silicon wafer. This silicon layer,

also known as silicon on insulator (SOI), is used as a protective layer to ensure the accuracy of the desired thickness of the device layer during the etching process [32]. The pattern of the microcantilever is completed using photolithography (UV lithography). The final phase involves the etching the backside of the silicon wafer and the etch stop layer therefore the release of the microcantilever. This step is often accomplished by using an antistrophic etchant such as KOH [32,35].

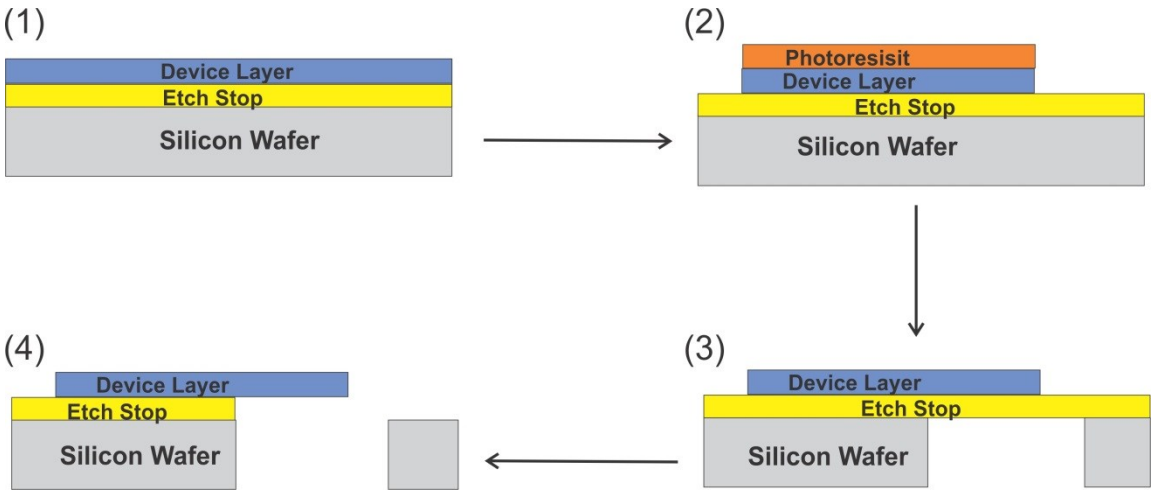

Figure 1.3: Bulk Micromachining process: (1) the deposition of the etch stop layer on the silicon wafer followed by the device material; (2) patterning of the microcantilever by UV lithography; (3,4) the release of the microcantilever by first etching the silicon wafer then the removal of the etch stop layer.

Microcantilever sensors possess several advantages over other types of sensors such as high sensitivity, cost-efficiency, small size, ease of fabrication in large arrays, and simple manipulation. Their small dimensions which typically range from 350 to 750 μm long, 30 to 50 μm wide and 0.5 to 1 μm thick with a nominal spring constant ranging from 0.03 to

0.5 N m^{-1} contribute greatly to their sensitivity. Having such appealing properties have allowed microcantilever sensors to be successfully applied in many proof-of-purpose applications in different fields. Biomedical applications include using microcantilevers in detecting cancer [36], Human Immunodeficiency Virus (HIV) [37,38] and drug discovery [39]. Chemical and biochemical applications include using microcantilever sensors in detecting change in pH [40], explosives [41], DNA hybridization [42], proteins and antigen-antibody interactions [43]. Effective biological detection of *E.coil* bacterial has also been successfully performed with microcantilever sensors [44]. Recent developments in supramolecular chemistry have extended the use of microcantilever sensors to include the detection of metal ions [45].

1.3.1 Microcantilever Sensor Array

The majority of the reported research on microcantilever sensors has been conducted using single microcantilevers. Most of the experimental sensing platforms were designed to accommodate two single microcantilevers to act as active and reference microcantilevers. To assure the reproducibility of the results, cantilever sensor experiments are often repeated several times, which is a time consuming and expensive process. Although repeating the sensing experiments may examine the reproducibility, ensuring the existence of comparable experimental conditions is not often trivial or even possible. The limitations of using single microcantilevers paralleled with the the rapid advancement in micromachining technology have led to the development of

microcantilever arrays. A scanning electron microscopy (SEM) image of a microcantilever array is depicted in Figure 1.4.

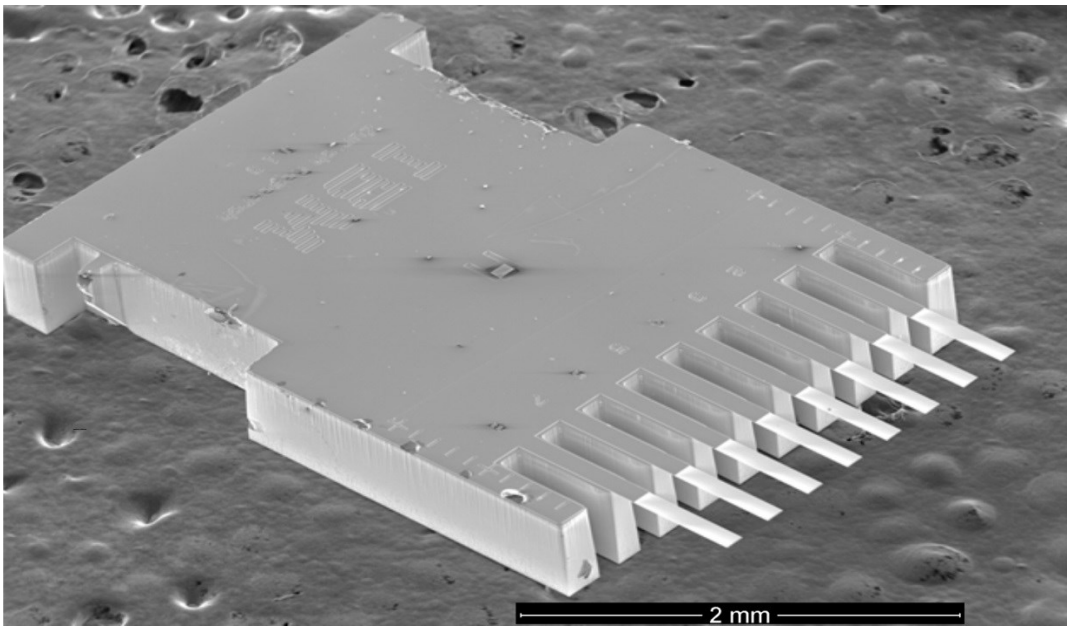

Figure 1.4: Scanning electron microscopy (SEM) image of the microcantilever sensor array.

Microcantilever arrays allow for the parallel alignment of both active and reference microcantilevers within the same chip which ensures that all microcantilevers within the chip are subjected to the same preparation conditions. The use of arrays also allows for the functionalization of a multiple of different active sensing layers which, in turn, eliminates the need to test the response of different sensing layers separately, as is the case for single microcantilevers. By measuring the response of multiple similar or different sensing layers using the microcantilever arrays, a substantial cost and time savings can be achieved.

The utilization of microcantilever sensor arrays as sensing platforms for bimolecular and chemical detection has been recently witnessed [46,47]. The compelling features as well as the impressive performance exhibited by microcantilever sensor arrays may cause a shift from the use of single microcantilevers to the use of arrays.

1.3.2 Microcantilever Surface Functionalization

The main operating principle behind microcantilever sensors is based on the formation of a self-assembled monolayer of a receptive material on the microcantilever surface. The importance of microcantilever surface functionalization stems from the fact that both the sensitivity and selectivity of the microcantilever are predominantly determined by the functionalization layer. Uniformity, stability, and compactness are some of the major proprieties that the receptor layer on the microcantilever sensor should possess. Target analyte of interest can then preferentially bind with the receptive molecules. Thus the microcantilever sensor needs to be properly functionalized before it can be used for the detection of physical, chemical or biological phenomena.

Functionalizing the microcantilever surface is normally conducted in our laboratory via the following steps: cleaning the microcantilevers, depositing a thin gold film, and incubating in the functionalization solution. Each step must be completed appropriately and carefully in order to ensure that the microcantilever still possesses its physical properties. Studies conducted in our group and by others [48] have revealed that the microcantilever response can change drastically depending on the cleaning methodology.

Thus it is of great importance to optimize the cleaning methodology in order to obtain microcantilever sensors with the highest sensitivity. In the present work, two different methodologies were tested where it was found that RCA cleaning gave the best results (see Chapter 4). The effect of the cleaning method was clearly seen on the reflected laser beam off the microcantilever surface. If the microcantilever was cleaned simply with ethanol, as an example, the beam spot was widely scattered appearing large in size making it difficult for the position sensitive detector (PSD) to detect. On the other hand, the use of the RCA method was found to produce highly focused laser spot which is indicative of the cleanness of the surface. The second step of the functionalization process was depositing a thin adhesive layer of Inconel followed by a thin gold film. Gold has been used extensively for attaching the receptive molecules because it is inert and does not oxidize which helps prevent receptor molecules from desorbing from the microcantilever surface. Most importantly, gold has been reported to form a strong bond with alkanethiols, permitting the formation of thiol based self-assembled sensing layers onto the surface. Depositing a thin film can be accomplished via several techniques such as thermal evaporation and sputter deposition. In the former technique, in which the sample is placed in a vacuum, the material evaporates from a hot source and then condenses on the substrate forming a thin film of the material. In the latter method, which is used in our work and is discussed in greater details in chapter 3, the target atoms (e.g. Au) are ejected from a target and deposited on the substrate due to collisions between the target and argon ions. Following the deposition of the thin gold film on the microcantilever surface, scanning probe microscopy such as AFM or STM was used to

characterize the morphology of the gold film on the microcantilever surface. This step was performed since it is known that the gold morphology has a great influence on the microcantilever sensitivity, reliability and reproducibility [48-51]. The next step involves incubating the Au coated microcantilever in a solution of receptor molecules for a certain period of time. The lower side of the microcantilever surface can either be passivated or left untreated. Passivation is often performed using a chemical treatment such as bovine serum albumin (BSA) [52] however such treatment requires additional sample preparation time. Instead, leaving the lower surface uncoated with bare silicon and using a reference microcantilever which is not sensitive to the target molecules is considered an effective alternative. Differential measurements are obtained by subtracting the reference signal from the active microcantilever measurements to exclude deflections due to thermal effects and non-specific interactions.

The surface functionalization of a microcantilever can be accomplished by several methods. In the case of single microcantilevers, the immersion of the microcantilever into a solution containing the receptor molecules is sufficient. However, when using microcantilever arrays where each or some of the microcantilevers are modified with different sensing layers, advanced functionalization strategies need be considered. One of these strategies is inkjet printing where a 3D positioning system is used allowing for a precise and controlled coating of each microcantilever within the array [53]. An alternative functionalization approach is to insert the microcantilevers into capillaries having a separation distance corresponding to the microcantilever spacing. These capillaries are filled with the solutions of the probe molecules. Despite the requirement of

skillful handling and precise alignment, the use of microcapillaries was employed in this work and has been found to be an efficient method of functionalization.

1.3.3 Modes of Operation and Detection Schemes

Microcantilever sensors are often operated in either static or dynamic mode. In *static mode*, the microcantilever deflection resulting from the adsorption and/or interaction of the target molecules with the receptive layer on the microcantilever surface is monitored (see Figure 1.5). This mode has been by far the most frequent employed mode in sensing experiments. Since this mode has been used during this work, a detailed description of this mode and its mechanism is provided in *Chapter 2*.

In the *dynamic mode* (shown in Figure 1.5), the mass load on the microcantilever causes the latter to oscillate at a new frequency. Such vibrations can be detected and translated into a useful signal. When molecular adsorption takes place on the microcantilever surface, its resonant frequency f decreases as a result of the addition in mass according to:

$$f = \frac{1}{2\pi}\sqrt{\frac{k}{m}} \tag{1.1}$$

where k is the spring constant and m is the effective mass of the microcantilever. For a rectangular microcantilever, the spring constant, which determines the microcantilever flexibility and effective mass can be expressed as [33]:

$$k = \frac{Ewt^3}{4L^3} \tag{1.2}$$

$$m = 0.243\rho L(wt) \tag{1.3}$$

where E is Young's modulus ($\approx 2 \times 10^{11}$ N m^{-2} for a silicon microcantilever), w, t, L are the microcantilever width, thickness and length respectively, ρ is the mass density, and *0.243* is a correction factor that accounts for the fact that the mass of the microcantilever is not uniform. A change in mass Δm can then be determined from the initial and final frequency as well as the initial mass of the microcantilever before adsorption:

$$\Delta m = \frac{k}{4\pi^2}\left(\frac{1}{f_0^2} - \frac{1}{f_1^2}\right) \tag{1.4}$$

where f_0 is the resonance frequency of the microcantilever before the mass addition and f_1 is the final resonance frequency. This equation clearly shows that the adsorbed mass can be estimated from the variation in the frequency of microcantilever.

Besides these two modes, a third mode can be used by coating the silicon microcantilever with a thin film layer. Having a different coefficient of thermal expansion between the metallic layer and silicon would cause the microcantilever sensor

to deflect when the temperature changes, as depicted in Figure 1.5. This mode is known as the *bimetallic or heat mode*. The deflection of a rectangular microcantilever due to the bimetallic effect can be calculated from the following expression [54]:

$$\delta_{Thermal} = \frac{3L^2(\alpha_s - \alpha_f)(t_s + t_f)}{K\ {t_s}^2}\ \Delta T \tag{1.5}$$

where K is expressed as:

$$K = 4 + 6\left(\frac{t_f}{t_s}\right) + 4\left(\frac{t_f}{t_s}\right)^2 + \left(\frac{E_f}{E_s}\right)\left(\frac{t_f}{t_s}\right)^3 + \left(\frac{E_f}{E_s}\right)\left(\frac{t_s}{t_f}\right) \tag{1.6}$$

where α_s and α_f are the thermal expansion coefficients of the substrate (silicon) and the film (gold), respectively, t_s and t_f are the thicknesses of the substrate and the film, respectively, E_s and E_f are Young's modulus of the substrate and the thin film, respectively, L is the microcantilever length, and ΔT is the change in temperature.

It has been reported that using microcantilever sensor, a temperature change as small as 10^{-5} K can be detected [54]. Utilizing the bimetallic effect, microcantilever sensors have also been demonstrated as an ultrasensitive calorimeter with a sensitivity as high as 10^{-15} J [55]. Although such high sensitivity obtained from the bimetallic phenomena can make microcantilever sensors sensitive calorimeters, it can contribute to parasitic microcantilever deflections caused by thermal fluctuations. This reinforces the

importance of using reference microcantilevers in all experiments so that such effects can be eliminated.

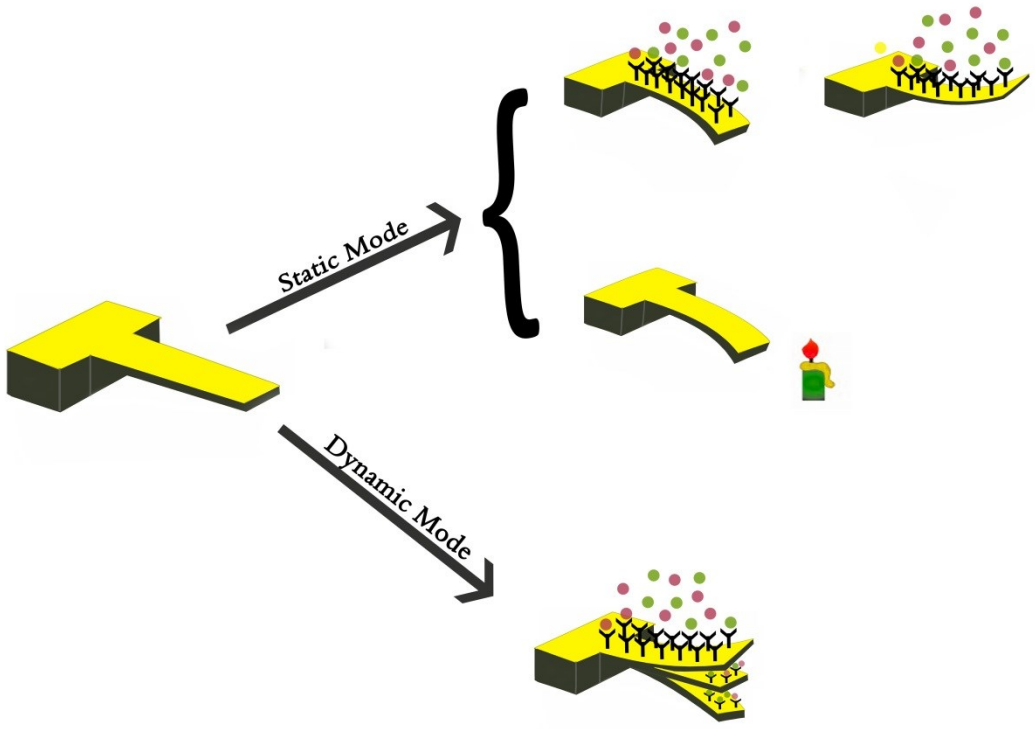

Figure 1.5: A schematic depiction of the two fundamental operation modes (static and dynamic) of microcantilever sensors. The bimetallic (heat) mode is classified as a type of static mode since the microcantilever deflects instead of vibrating when subjected to heat.

The microcantilever deflection and resonance frequency can be measured precisely using multiple approaches such as an optical beam deflection system, piezoresistance or capacitance. In the former method, a laser beam is focused at the free end of the

microcantilever which then reflects into a position sensitive detector (PSD). This system which was used in this study is used for monitoring the microcantilever deflection in an atomic force microscope (AFM). In the second approach, the microcantilever is integrated with a piezoresistor which undergoes a change in resistance when the microcantilever bends. A Wheatstone bridge placed at the base of microcantilevers is then used to measure the change in resistance. The advantage of this technique is that it is suitable for both static and dynamic measurements and can facilitate the read out of large arrays. However this method is confronted with the problem that the integration of the piezoresistive material into the microcantilever can affect its performance [56]. In the capacitance method, a change in the capacitance between two electrodes, one of which is the microcantilever, is measured. Such change results from the microcantilever bending which changes the distance between the two electrodes. This method is relatively simple and does not require complicated electronics and is useful for use with nano-sized microcantilevers. This method has however the limitation that maintaining a small distance between the two plates is very difficult [57]. Of all common methods of measuring the microcantilever deflection, the optical beam deflection system is the most widely used due to its comparative simplicity and accuracy.

1.3.4 Microcantilever Sensitivity and Selectivity

Selectivity and sensitivity are the two fundamental performance criteria of microcantilever sensors and should be optimized in order to increase their reliability and

robustness. This, in turn, would help pave the way for the future commercialization of microcantilever sensors. The sensitivity of the microcantilever sensor to molecular interactions and to changes in the surrounding environment can be substantially enhanced by optimizing its geometric design. The advancement in micromachining technology has made it feasible to fabricate microcantilever sensors with miniaturized size with high accuracy. This has increased the sensitivity of microcantilever sensors to unprecedented levels allowing detection limits in the femtomolar and attomolar ranges to be reached [58].

For dynamic mode sensing, the parameters that affect the response of microcantilever sensors are the resonance frequency f and the spring constant k. In order to maximize the sensitivity, microcantilever sensors should have both a high operational frequency and spring constant which can be obtained by having short length (5- 50 μm), low density and high Q-factor microcantilevers. Under these conditions, it has been possible to detect mass changes in the attogram range [59]. Gupta *et al.* [60] have successfully demonstrated the possibility of detecting single virus particles of femtogram mass using microcantilever sensors. In comparison with existing mass sensing technologies such as quartz crystal microbalancers (QCMs) and surface acoustic wave (SAW) which have mass sensitivities in the nano and picogram range, the mass sensitivity obtained with microcantilever sensors is higher by many orders of magnitude [61].

For microcantilever sensors operating in static mode, the length and thickness are the main characteristics affecting the microcantilever sensitivity. Longer (300-1000 μm) and

thinner microcantilevers (0.5-2 μm) which ensure low spring constant largely enhances the sensitivity in this mode (i.e. increasing the flexibility of the beam) (See Equation 1.2). It has been reported that using such longer and thinner microcantilevers for the detection of DNA hybridization that sensitivity on the order of 10^{-11} M can be achieved [38].

Efforts to increase the microcantilever sensitivity were also made by fabricating microcantilever sensors with a very low Young's modulus materials such as polymers [62]. Because of their low Young's modulus (~ 5 GPa) compared to silicon (~180 GPa), the stiffness of polymers is less than silicon-based microcantilevers which consequently increases the sensitivity. Despite the increased sensitivity, low cost and adaptable mechanical properties of polymer-fabricated microcantilevers, their instability and insufficient reflectivity can affect their performance. Unstable output signals from polymer microcantilevers were observed to be caused by moisture absorption in liquids or degassing in vacuum [63].

Another key factor that influences the microcantilever sensitivity is the sensing medium. There are several factors pertaining to the medium, which when carefully controlled can increase the microcantilever sensitivity. Flow rate, temperature and the geometry of delivery system of the target analyte are key parameters with very high influence on the microcantilever sensitivity. Rapid flow rates as well as changes in temperature can potentially induce parasitic microcantilever deflection. Although the effect of these factors can in principle be eliminated by the use of reference microcantilevers, it is nevertheless important to control these factors. With regards to the geometry of the

analyte delivery system, in a recent qualitative analysis performed in our group [64] it was found that the capture efficiency and thus sensitivity of microcantilever sensors are considerably influenced by the mechanism that presents the analyte to microcantilever sensors. The damping effect of liquids is another aspect that needs to be considered for sensitivity enhancement. The resonance frequency of a microcantilever in liquid can decrease by orders of magnitude compared to its resonance frequency in air. Compared to dynamic-mode microcantilevers, static mode-microcantilevers have very small resonance frequencies and would not be affected by the viscous properties of the medium and are thus suitable for operation in liquids. For this reason, static mode microcantilevers were used during the course of this work in which experiments were conducted in liquid.

Achieving extreme sensitivity and selectivity requires not only the optimization of the geometric design of the microcantilever sensors but also the optimization of the immobilization techniques. The key to achieving high chemical or biological selectivity using microcantilevers is the functionalization of the upper surface of the microcantilever with the proper receptive layer that demonstrates the highest affinity towards the target analyte. Microcantilever sensors can be chemically functionalized with a number of selective receptive coatings such as DNA probes, antibodies, aptamers and proteins. The immobilization of the receptor material should be efficient in order to increase the accessibility of the target analyte and to decrease the effect of non-specific bindings [65]. Selectivity and sensitivity can also be improved by optimizing the incubation time, as will be shown in *Chapter 5*. In summary, for surface stress sensing operated in static mode in a liquid environment with an optical beam detection scheme, the following

measures should be taken into account in order to increase the overall microcantilever sensitivity:

- The microcantilever sensor should have low spring constant which can be achieved by the use of long and thin microcantilevers.
- The microcantilever should be fabricated from silicon because of its well-defined material properties (Young's modulus, density and spring constant) which are important for the deflection and surface stress calibration.
- The deposition of gold on the microcantilever sensor would also provide a highly reflecting surface required for the optical beam deflection system.
- The Au-coated microcantilever should have no or at least very little initial bending which can prevent further surface stress from occurring due to subsequent molecular adsorption. This issue is addressed within the text of the thesis.

1.4 Motivation

Fresh water contains a variety of metal ions which are very important for environmental and health concern. Ca^{2+} is one of the divalent cations that is present in fresh water and normally originates from the dissociation of calcium chloride $CaCl_2$ in water. Calcium is essential for cellular metabolic processes which are important for the formation of the structural elements of most living organisms [66]. Ca^{2+} ions can also be introduced into fresh water from Ca-containing rocks and minerals, such as limestone ($CaCO_3$), gypsum

($CaSO_4 \bullet 2H_2O$), or bones. The concentration of Ca^{2+} ions in fresh water typically ranges between 0-100 mg/L. The presence of high concentrations of Ca^{2+} ions may not be considered as a health concern but low concentrations of Ca^{2+} ions (below 5 mg/L) in fresh water is potentially dangerous to many fish and fish habitant [67,68]. In a study conducted by Jeziorski *et al.* [69] on samples collected from 770 lakes in Ontario, Canada, it was found that 62% of the investigated lakes had Ca concentrations below 2 mg/L. Such low Ca levels are believed to affect the life span and the reproduction ability of several aquatic organisms and also have negative consequences on other organisms that have a high Ca demand. The concentration of Ca^{2+} in fresh water may drop significantly due to natural phenomenon such as acid rain or by industrial waste dumping. In contaminated water sites, Ca^{2+} ion has the possibility to combine with waste anions and form crystalline substances (e.g. SO_4^{2-} react with Ca^{2+} to form $CaSO_4$) which thus considerably reduces the concentration of free Ca^{2+} ion in fresh water. Despite the presence of several techniques for detecting calcium ions, the sensitivity of these techniques is limited [70,71]. Therefore, the hazardous effects of industrial activities to the environment stressed the need to make significant efforts towards reducing further harm to the environment.

One of the motivations of this work was inspired by an industrial activity performed in Newfoundland, Canada. The hydrometallurgy process (Hydromet Plant) at Long Harbour NL plans to use Voisey's Bay massive sulfide ore for processing cobalt, zinc and nickel and will generate a considerable amount of iron and sulphur residue (acid

generating) as byproducts. As shown in Figure 1.6, during the mining process where the ore is treated to recover precious metals, tailings are produced which are then pumped, in the above case, into Sandy Pond which has already been marked as a contaminated pond.

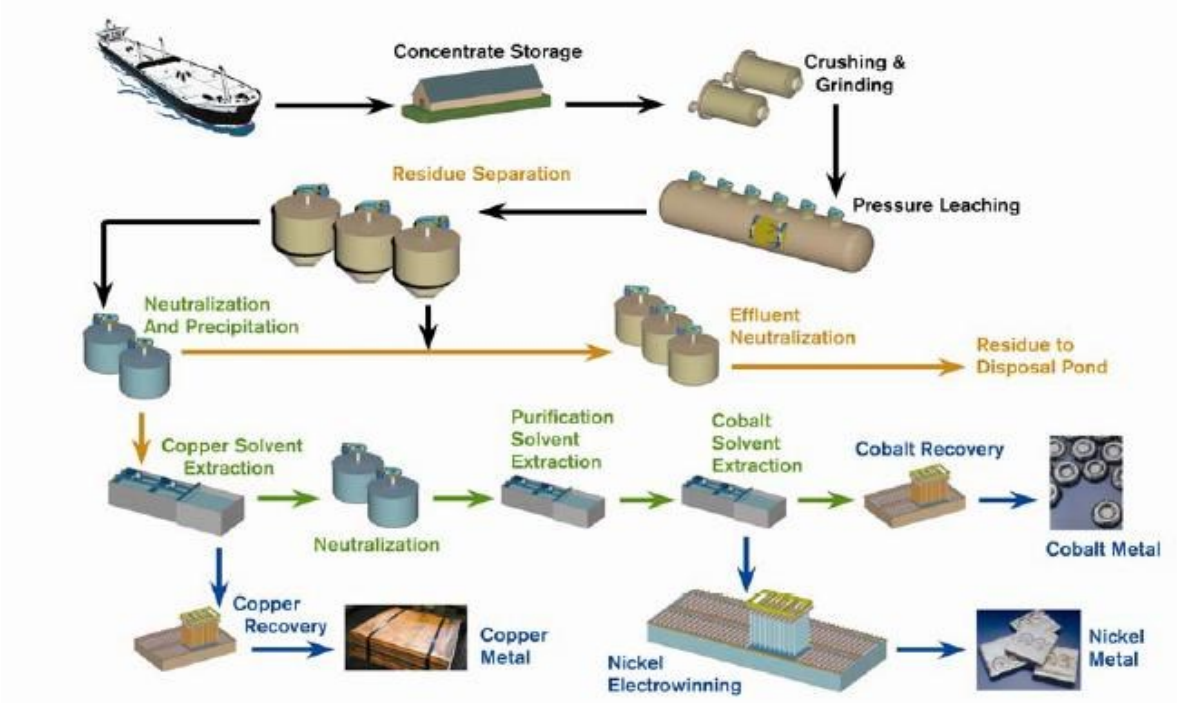

Figure 1.6: The process of Hydromet Plant at Long Harbour by Vale [72].

According to Vale [72], 381,000 tonnes per year of residues are anticipated to be produced and sent to Sandy pond. Such a high amount of acid generating residues creates the need for monitoring selected heavy metals to ensure that the amounts of metals introduced into the lake do not exceed safe levels. A real-time method of monitoring the effluent going into Sandy Pond is therefore desirable.

As discussed previously (see Section 1.1), there have been several approaches of measuring the amount of heavy metals in fresh water. Despite the fact that these techniques are capable of providing accurate measurements of the concentrations of metal ions in fresh water, they are time-consuming, expensive and lack *in-situ* monitoring capabilities. Most of the current detection methods require samples to be first collected and then sent to be analyzed which can potentially contaminate the samples resulting in inaccurate measurements. To circumvent such limitations, several sensing-based devices such as fluorescence-based sensors [73] immunosensors [74], and optical fiber sensors [75] were developed and employed as fast and reliable measurements of heavy metal ions. Despite the impressive development observed with these sensing techniques, newer, more novel and more adept detection techniques are needed to confront the limitations of the current sensing techniques. Chemically-modified microcantilever sensors were thus investigated in this work in the hopes of providing rapid, sensitive and selective monitoring of metal ions in fresh water.

1.5 Objective and Methodology

The objective of this work is to develop a methodology for the rapid and sensitive detection of concentrations of metal ions in fresh water using microcantilever sensors. Achieving this objective first requires the development and synthesis of new receptor molecules which can selectively bind to specific metal ions (e.g. Ca^{2+}). For this project a new type of sensing layer has been created by Dr. Georghiou's group in the Department of Chemistry, Memorial University using calixarene molecules. Modified calixarene molecules were immobilized onto the microcantilever surface forming a self-assembled monolayer (SAM). These calixarene molecules were chemically modified to be able to recognize and selectively bind with metal ions of interest. To be selective, these calixarenes should also be unresponsive to other accompanying cations and anions that may be present in the solution being tested. In order to evaluate the aforementioned criteria, calixarene molecules functionalized on the microcantilever surface were exposed to target molecules so as to test their affinity towards specific metal ions. In this project, we also aimed at investigating the binding interaction of three calixarene compounds with target ions simultaneously which thus can improve the precision and reliability of the results. Consequently, the design and development of a new microcantilever setup which will allow 16 microcantilevers to be functionalized with different sensing layers and to be monitored simultaneously has been a fundamental objective of this work. The achievement of the main objectives of this work has been attempted through the following phases:

- The synthesis of self-assembled monolayers (SAM) of calixarene molecules for use as sensing layers on Au microcantilevers. These molecules are also modified so that they can selectively bind to a variety of cationic and anionic target analytes. This objective has been completely performed by Dr. Georghiou's group in the Department of Chemistry.

- Investigating the immobilization of these calixarene compounds on Au-coated microcantilevers using scanning tunneling microscopy (STM). The aim of such studies was to assure that these new calixarene molecules were capable of adhering to Au surfaces and to test their stability in forming self-assembled monolayers on the Au-coated microcantilever surfaces and by the subsequent interaction with the target ions of interest.

- The third phase of this work included the investigation of the sensitivity of calixarene-functionalized microcantilevers towards specific target ions. The binding capabilities of these modified calixarenes were also tested by attempting to determine their selectivity by comparing microcantilever detection measurements of similar target anions and cations. This phase is very important as it helps to develop a deeper understanding of the reaction dynamics of calixarenes as chemical sensor layers on microcantilevers and also in the development of ultrasensitive target ion detectors which have numerous medical and environmental applications.

- One of the major undertakings of this work was the development of a new experimental platform which allows the simultaneous measurements of up to 16 functionalized microcantilevers. The development of the functionalization unit which facilities the simultaneous functionalization of microcantilevers within the array with different sensing layers has also been performed.

- In order to optimize the experimental conditions under which the sensitivity of calixarene-functionalized microcantilever can be amplified, an investigation of the effect of gold morphology as well as the functionalization time have been conducted.

1.6 Scope and Outline

Since this work endeavors to develop calixarene-modified microcantilever-based sensors for the detection of metal ions in fresh water, this thesis begins with an introduction and review of metals ions and their importance to the environment. An overview of the current technologies for detecting metal ions in water samples is also provided. Chapter 1 also presents the operating principle, detection schemes, and applications of microcantilever sensors. Chapter 2 provides a discussion of surface stress and molecular self-assembly, which are the major factors that govern the microcantilever response. The theory of surface stress which is the main cause of the mechanical deflection of microcantilever sensors during bimolecular adsorption will first be reviewed. The

concept of self-assembled monolayer (SAM) will also be discussed with an emphasis on thiol-based SAMs.

Following Chapters 1 and 2, this thesis is divided into two parts. Part I is concerned with the experimental results obtained with the single microcantilever system. Part II is devoted to a description of the development of the new microcantilever array system and the experimental results obtained with it.

Part I starts with a brief description about the single microcantilever system in Chapter 3. The experimental and characterization techniques such as sputter deposition, scanning tunneling microscopy (STM) and atomic force microscopy (AFM) are also described in this chapter. Chapter 4 gives an overview of the synthesis and structure of the three calixarene compounds used as the recognition layers on the microcantilever surface. The experimental procedures followed in the preparation of microcantilevers for sensing experiments is also presented in this chapter. Chapter 5 concludes Part I and outlines the experimental results obtained with the single microcantilever experimental platform following by a thorough discussion of these results. STM characterization of calixarene SAMs on the microcantilever surface is also demonstrated in this chapter. The synthesis schemes of the calixarene compounds presented in Chapter 4 and part of the experimental results shown in Chapter 5 have been previously reported in paper publications (please refer to the footnotes at the beginning of Chapters 4 and 5).

Chapter 6 marks the beginning of Part II and is intended to provide a detailed description of the new 16-microcantilever sensor system. Chapter 6 also discusses the development procedures, components and the calibration process of the new array-based experimental set up. Chapter 7 is dedicated to discussing the experimental measurements of the new experimental system. Chapter 8 presents a summary and conclusion of this work and offers recommendations for future works.

Chapter 2 Surface Stress and Molecular Self-Assembly

2.1 Surface Stress

The response of microcantilever sensors operating in static mode is principally attributed to the formation of a surface stress on the microcantilever surface. The interactions between the target molecules and the functionalized side of the microcantilever result in a change in surface stress between the functionalized surface and the uncoated surface of the microcantilever. This change in surface stress subsequently leads to the generation of a measurable microcantilever deflection. Hence it is of crucial importance to understand the mechanism and causes of the surface stress induced during molecular adsorption and interactions. Surface stress also plays a central role in the description and understanding of many surface phenomena and the structural processes at the atomic scale [76,77]. Several physical and chemical processes such as surface reconstruction, surface and adsorbate interactions and self-assembly organization have been proposed to be affected by surface stress [78-80]. Several studies have been devoted to identifying the conditions and factors controlling the generation of surface stress. These studies have benefited from the invention of advanced imaging techniques such as scanning probe microscopy (SPM) for gaining insight into the surface stress induced on solid surfaces [81,82]. In order to understand the physical origin of surface stress, both atomistic and thermodynamics

perspectives should be considered. Since surface stress can be formed on solid surfaces by different mechanisms, three different classifications are commonly used to describe the surface stress. Adsorption-induced surface stress is the first classification of surface stress and is defined as the mechanical stress formed on a surface because of the interactions with adsorbates. This type of surface stress has generated a growing interest because it is associated with the understanding of molecular interactions on surfaces. The second classification is the surface stress of thin films. During the deposition of thin films on solid substrates, surface stress can be formed due to the defects in the film (e.g., intrinsic stress) and/or differential thermal expansion (e.g., extrinsic stress) [83]. A detailed discussion of these two types of stress will be presented within the text as they are pertinent to the scope of this thesis. Surface stress of clean surfaces is a third classification of surface stress and has been given significant attention over other types of surface stress as it is attributed to the association with the structure and coordination of surface and bulk atoms [80,81,84]. The physical origin of surface stress at the atomic scale can be understood by the following argument. The surface atoms of a crystalline metal have a lower charge density (e.g., fewer neighboring atoms) than atoms at the bulk and consequently have different equilibrium interatomic spacing [76]. This difference in charge density and bonding configuration between surface atoms and bulk atoms causes the surface atoms to experience a force pointing towards the interior of the bulk. For transition and noble metals surfaces such as Au, surface atoms seek to increase the charge density by adopting a smaller equilibrium interatomic distance which increases the bonding strength between surface atoms [77]. The change in charge density between the

surface atoms and bulk atoms is the main driving force that causes surface reconstruction of metals. As discussed by Ibach [84], the redistribution of the electrons at the surface of transition and noble metals takes place as a result of the space between the surface atoms. Because of the missing bonds, a part of the bond charge at the surface is expected to flow into the space between surface atoms, as schematically depicted in Figure 2.1.

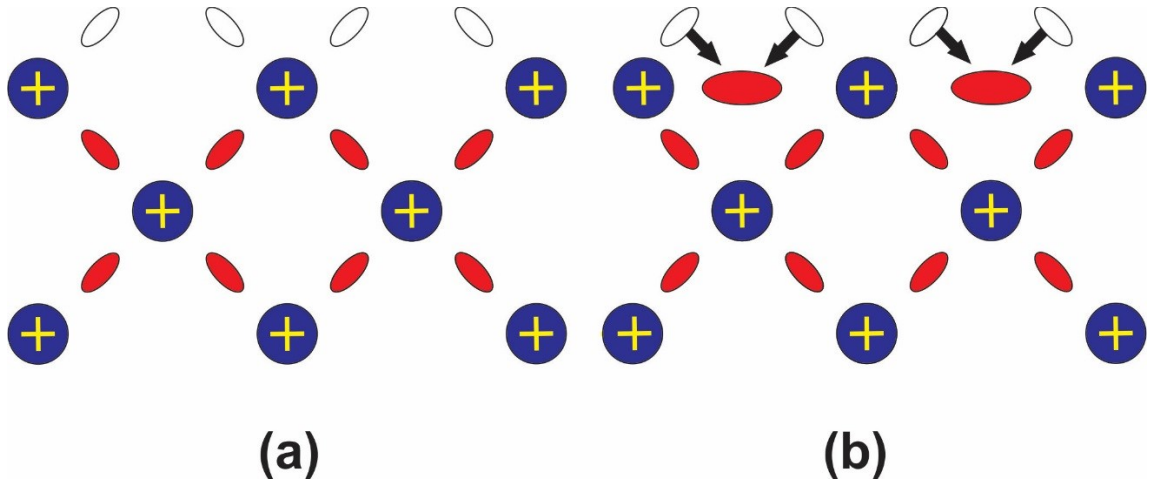

Figure 2.1: The simple model of the charge distribution that occurs in clean metals surfaces. (a) Bond charges, shown in white, before moving into the space between the surface atoms. (b) The redistribution of the bond charge as they move into the space between the first layers of atoms, leading to an increase in bond strength between surface atoms. [Adapted with permission from Reference 84].

This bond charge redistribution leads to an increase in bond strength between surface atoms and therefore a tensile surface stress is generated. This simple model explains the formation of the native tensile surface stress in many clean metals surfaces. It can also be

used to obtain a qualitative understanding of the surface stress at metal–electrolyte interfaces [77]. This type of reconstruction has been widely observed with Au (111) [85], Au (100) [86], and Pt (111) [87].

2.1.1 Stress and Strain

Stress σ is conventionally defined as the force (F) acting on a material per unit area (A) and is given as:

$$\sigma = \frac{F}{A} . \tag{2.1}$$

The generation of surface stress on a surface is generally accompanied by the induction of strain which is a measure of the change in length (ΔL) of a material relative to the original length (L) in response to the applied force express as:

$$\varepsilon = \frac{\Delta L}{L} . \tag{2.2}$$

Surface stress and strain are related to each other by Young's Modulus:

$$E = \frac{\sigma}{\varepsilon} . \tag{2.3}$$

This relationship is a fundamental quantity used in describing the mechanical properties of materials during elastic and plastic deformations [88].

Surface stress ($\boldsymbol{\sigma_{ij}}$) is a tensor that results from the forces acting at the material surface. Stress induced when the force is acting perpendicularly to the surface is called *normal stress* whose components (σ_{xx}, σ_{yy}, σ_{zz}) are commonly denoted by repeated subscripts. Tensile and compressive stresses are two notable types of normal stress. On the other hand, *shear stress* represents the forces that are parallel to the area on which it acts and has stress components with mixed subscripts (e.g. σ_{xy}, σ_{zy} ...). The components of the second rank surface stress tensor is written as:

$$\boldsymbol{\sigma_{ij}} = \begin{bmatrix} \sigma_{xx} & \sigma_{xy} & \sigma_{xz} \\ \sigma_{yx} & \sigma_{yy} & \sigma_{yz} \\ \sigma_{zx} & \sigma_{zy} & \sigma_{zz} \end{bmatrix}. \tag{2.4}$$

This tensor form of the surface stress can take a simpler form in certain cases. Surface atoms are free to relax in the direction perpendicular to the surface and as a result stress is not developed in this direction and hence $\sigma_{zz} = 0$. For high-symmetry surfaces in which the surface stress is isotropic, i.e. in the case where threefold and higher symmetry (111) or (100) surfaces are considered, the off-diagonal components vanish and the diagonal components are equal ($\sigma_{xx} = \sigma_{yy}$). In this case, the surface stress becomes a scalar quantity given by scalar $\boldsymbol{\sigma = \sigma_{xx} = \sigma_{yy}}$.

2.1.2 Thermodynamics of Surface Stress

In order to understand the thermodynamics at a solid surface, two fundamental surface properties must be discussed and clearly distinguished. According to Gibbs [89], the main characteristics of a solid surface are surface stress (σ_{ij}) and surface energy (γ), which are often mistakenly used interchangeably. Surface stress (σ_{ij}) is defined as the reversible work required to form a unit area of new surface by elastically stretching a pre-existing surface [77]. Surface energy (γ) is the reversible work per unit area required to create a surface. From an atomistic point of view, surface atoms have higher potential energy than bulk atoms and overcoming this difference is required in order to for bulk atoms to move to the surface. A measure of such energy difference defines the surface energy. Creating a new surface from which the surface energy originates requires splitting of a crystal or a cleaving process which thus indicates that the surface energy is principally induced by bond breaking (See Figure 2.2). Surface stress which is related to the elastic stretching of a pre-existing surface originates from bond stretching as illustrated in Figure 2.2. Thus changes in energy during plastic deformation of a surface area are related to surface energy whereas the surface stress is associated with energy changes during the elastic deformation of a surface [90].

For liquids, it is generally considered that the surface stress and surface energy are equal and are often referred to a term called *surface tension*. When a liquid surface is deformed (e.g. by expansion), atoms or molecules from the interior of the liquid flow to the surface in order to compensate for the change in the number of surface atoms. This indicates that

although the numbers of atoms in the surface have changed the area per molecule remains constant during the deformation and thus surface energy does not change. This type of deformation is called plastic.

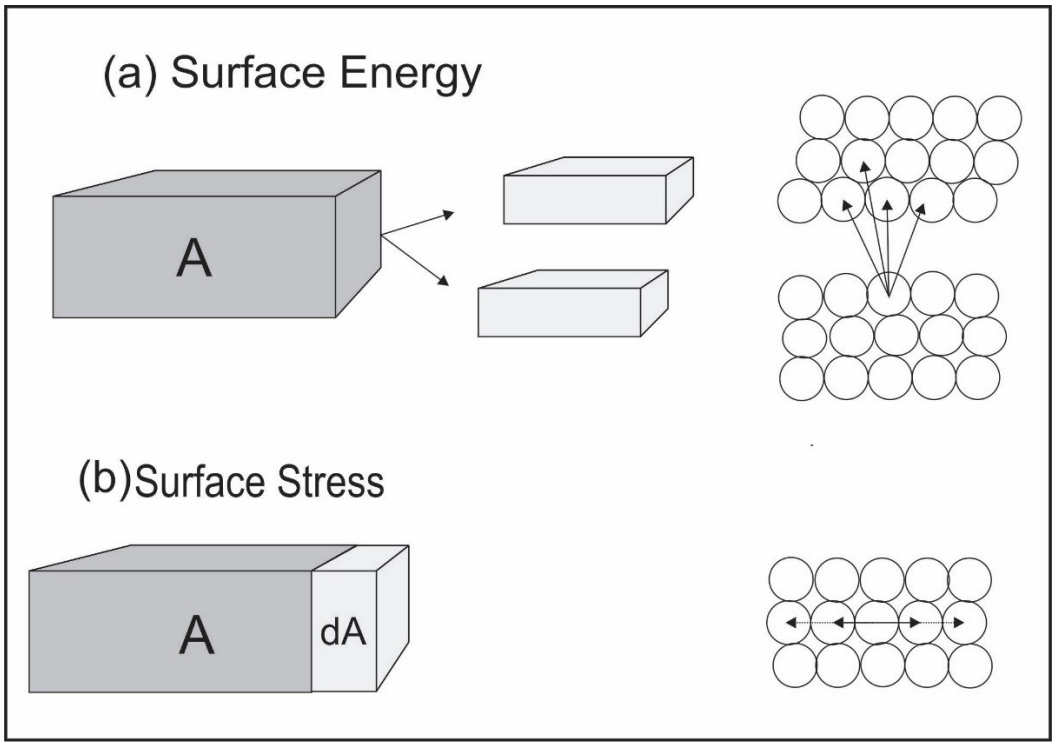

Figure 2.2: Schematic depiction of the concept of surface energy and surface stress. (a) The surface energy results from cutting a surface and thus by bond breaking. (b) The surface stress is the work required to create a unit area of a new surface by stretching a surface and thus is related to bond stretching. [Adapted with permission from Reference 90].

On the contrary, the number of atoms at a solid surface remains constant during surface stretching but the area per molecule is altered which leads to changing the surface energy.

Such a deformation is called elastic. The reason that the number of atoms at a solid surface remains the same during deformation is that the bulk atoms are not mobile thus no movement from the bulk would change the number of surface atoms. Based on the aforementioned definitions of surface stress and surface energy, it is obvious that these two notions are different and a distinction has to be made between them when studying solids.

Mathematical representations showing the relationship between surface stress and surface energy and work are presented as follows:

$$dw = \gamma \ dA \tag{2.5}$$

$$dw = A\sigma_{ij} d\varepsilon_{ij} \tag{2.6}$$

where dw is the isothermal reversible work performed to create a surface area A, dA is the infinitesimal elastic increase in surfaces area. The elastic strain tensor is defined as the ratio of change in surface area

$$d\varepsilon = \frac{dA}{A}. \tag{2.7}$$

Shuttleworth has developed a mathematical formula that relates the surface energy to the surface stress as [91],

$$\sigma_{ij} = \gamma\delta_{ij} + \frac{\partial\gamma}{\partial\varepsilon_{ij}} \tag{2.8}$$

where δ_{ij} is the Kronecker delta. The stain tensor ε_{ij} is often used to express the elastic deformation of a solid surface. As stated above, the surface stress can, in certain cases, be considered as a scalar quantity and thus Equation (2.8) may be rewritten as:

$$\sigma = \gamma + \frac{\partial \gamma}{\partial \varepsilon}. \tag{2.9}$$

The Shuttleworth equation states that the total surface stress ($\boldsymbol{\sigma}$) on a surface is the sum of the surface free energy (γ) and the dependency of the surface energy on elastic strain ($\frac{\partial \gamma}{\partial \varepsilon}$). For the case of liquid interfaces, the Shuttleworth equation reduces to $\sigma = \gamma$ since, as described above, the surface energy is equal to the surface stress and thus the second term on the right-hand side vanishes (e.g. no elastic strain is observed in liquids). For solid interfaces, the term $\partial\gamma/\partial\varepsilon$ does not vanish as surface stress and surface energy are distinct in this case. For solid-liquid interfaces, it has been proposed that $\frac{\partial \gamma}{\partial \varepsilon} \approx 0$ and thus change in surface stress is equivalent to the change is surface energy [76,92]. This case can be applied to microcantilever sensors being operated in liquid environment. The elastic strain is the ratio of change in the surface area and realizing that the microcantilever deflection is very small compared to its length, the contribution of the elastic strain is often neglected and thus the variation in surface stress and change in surface energy are equal [93].

2.1.3 Measurements of Surface Stress

Since the generation of surface stress on a surface is mainly driven by molecular interactions and thin film formation, measuring surface stress is crucial for the understanding and description of the adsorption and thin film processes and their properties. For example, the change in surface stress as a function of adsorption coverage can be used to estimate several quantities associated with the interaction of molecules on a solid surface such as binding constant [94], analyte concentration [95] and the Gibbs surface excess of adsorption [96]. Measuring the change in surface stress is challenging and becomes even much more difficult when measuring the absolute value of surface stress. Determining the absolute stress value comes mainly from theoretical methods because of the difficulty of evaluating absolute surface stress using experimental means.

There have been a number of theoretical and experimental approaches used for the determination of variations in surface stress [97-99]. First-principles calculations and semi-empirical methods have been widely used for calculating both surface stress and surface energy. Needs *et al.* [100] performed first-principles calculations for several clean and unconstructed fcc metal surfaces in an attempt to understand the physical origin of surface stress. They studied the contributions of kinetic energy, electrostatic interactions and exchange-correlation to the surface stress and surface energy of metals. The authors have found that for low-electron density metals, the kinetic energy contribution was the largest whereas for high-electron density metals all three factors had a significant contribution to the total surface stress and surface energy. Several experimental methods

have been employed for measuring the changes in surface stress and surface energy. The experimental determination of surface stress is generally performed by measuring the elastic strain induced by the surface stress on the underlying bulk layer. One of the experimental techniques for the measurement of surface stress is the use of electron diffraction to measure the reduction in lattice constant of small crystals in response to the development of surface stress [101]. Despite the reasonable agreement between theoretical values and results obtained using electron diffraction, this method is restricted by several limitations such as the difficulty of interpreting the electron diffraction peaks and the possible surface contamination caused by the experimental creation of particles [77]. Another experimental method used for calculating the absolute surface stress is the solubility method [102]. This method requires the preparation of small particles making it limited to only some materials. The challenge of accurately measuring the size of the particles is another drawback of this method [103]. Since there are several problems with the experimental determination of the absolute value of surface stress, the variation in surface stress has been alternatively used to express the surface stress. The bending plate method was proposed by Gerald Stoney [104] when he realized that a deposition of a thin film layer on one side of a thin beam caused the beam to bend. The formation of a thin film induces a surface stress and thus the difference in surface stress between the two opposing surfaces causes the bending of the beam. Stoney developed a mathematical relationship between the bending of a rectangular beam (δ) and the differential surface stress ($\Delta\sigma$) is given by:

$$\Delta\sigma = \frac{Et^2\delta}{3L^2\,(1-v)} \tag{2.10}$$

where E is the Young's modulus, t is the beam thickness, L is the beam length, and v is the Poisson's ratio.

In summary, the experimental determination of surface stress and surface energy on solid surfaces is often a challenging task. Despite the availability of several experimental techniques for the measurement of surface stress, there are several issues associated with the majority of these techniques. The applicability to only certain materials and the dependency of special assumptions are some of the drawbacks that limit the universal applicability and reliability of these techniques. The use of microcantilever sensors as an experimental tool for the accurate prediction of variations in surface stress has been alternatively considered [105,106]. A detailed discussion of the physics of microcantilevers as surface stress sensors will follow.

2.2 Microcantilever as a surface stress sensor

The confinement of a molecular interaction or adsorption to one side of a microcantilever surface leads to the development of a differential surface stress which causes the microcantilever deflection. The measurements of the deflection signal can be used to gain insight into the mechanisms involved during the molecular interaction and to develop a better understanding of the origin of the surface stress. The formation of a

surface stress on the microcantilever surface can be upward or downward depending on the type of the surface stress formed, as schematically demonstrated in Figure 2.3. An upward deflection (a concave surface curvature) is caused by a tensile stress which is formed by the attractive interactions between the molecules on the microcantilever surface, indicating that bond strengths between surface atoms are stronger than those of bulk atoms. A downward deflection (a convex surface curvature) is, on the other hand, caused by the repulsive interactions between the molecules over the microcantilever surface and is referred to as compressive stress.

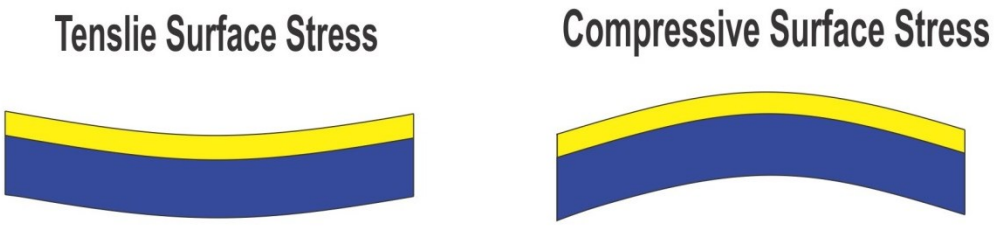

Figure 2.3: A schematic representation of the two types of surface stress induced during molecular adsorption or thin film deposition. In tensile surface stress, a concave curvature is formed because of the contraction in the top surface. A convex curvature is formed with the compressive surface due to the expansion of the top surface.

It is clear that surface stress is a crucial part of the micromechanical deflection and thus it has been the subject of intense investigation in order to gain a deeper understanding of the mechanism behind the microcantilever response [105,107,108]. Some investigations

attribute the formation of the surface stress on the microcantilever to electrostatic and steric interactions between adsorbates [109]. Besides being formed during molecular interactions, surface stress has also been observed during the thin film deposition and the formation of self-assembled monolayers (SAM) [49,110]. When such stress is large, it can reduce the magnitude of further surface stress to occur due to subsequent molecular adsorption. Thus controlling factors such as deposition temperature and gold thickness that influence the formation of surface stress is very important [50,111]. Experimental studies of the formation of the surface stress during thin film deposition are discussed in greater details in the experimental section of this thesis (see Chapter 5).

The deposition of thin films is a major source of the formation of surface stress onto microcantilever surface. As stated earlier, there are two types of surface stress in thin films: intrinsic and extrinsic stress. When a thin film such as gold is coated onto a silicon substrate, the mismatch in lattice parameter generates a differential surface stress between the two surfaces. This type of stress is referred as to *intrinsic stress,* which is a residual internal stress. The difference in the thermal expansion coefficient between the thin film and the substrate would also bend the microcantilever due to the formation of an *extrinsic stress during* changes in temperature [83]. The microcantilever sensor can be effectively used for the determination of the film stress that forms during thin film deposition.

The change of temperature experienced by the thin film and substrate during the deposition of a thin film can lead to the formation of a biaxial stress, which exists in the

plane of the film (x, y). Figure 2.4 shows the biaxial stress in a substrate coated with a thin film.

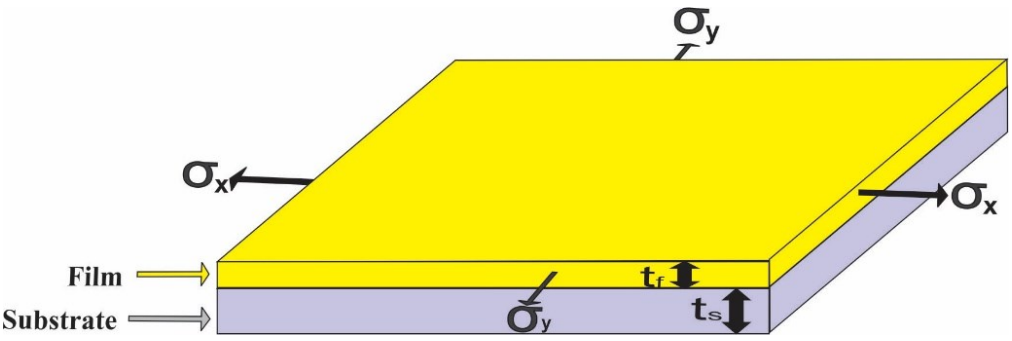

Figure 2.4: Biaxial stress formed by a thin film deposited on a substrate.

Biaxial stress can be induced by the differential thermal expansion between the thin film and the substrates. For example, if a thin film of Au is deposited onto a Si wafer and then bring them to a high temperature, the Si substrate will bend because it has a smaller thermal expansion coefficient than Au. The Au film which is attached to the Si substrate will be affected by the bending of the substrate and thus will be under a state of compressive stress. Such stress can be determined by finding the radius of curvature of the microcantilever sensor (i.e. deflection). Figure 2.5 shows the film under compressive stress on the bent substrate. The neutral plane located at the center of the substrate and shown in the figure represents the area of the substrate in which there is no stress.

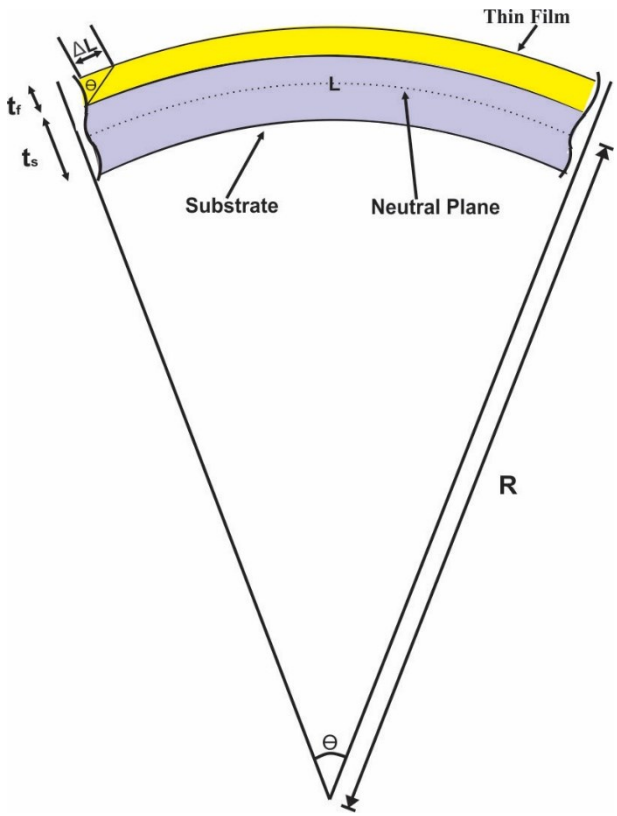

Figure 2.5: Cross-sectional view of a substrate experiencing compressive stress due to the deposition of a thin film.

The film stress σ_f is uniform across the film thickness due to the fact that the film thickness t_f is much smaller than that of the substrate t_s. The bending moment M_f produced by the stress in the film σ_f can be expressed as

$$M_f = \frac{b_f t_f t_s}{2} \sigma_f \tag{2.11}$$

where b_f is the film width and t_s is the substrate thickness. The relationship between the radius of curvature of the substrate and the substrate length can be written as:

$$\frac{1}{R} = \frac{2\Delta L}{L t_s} \tag{2.12}$$

where R is the radius of curvature of the substrate with respect to the neutral plane, L is the length of the substrate measured at the center, and $\frac{\Delta L}{L}$ represents the strain ε at the outer surface of the substrate. At the neutral plane, the elastic strain ε is zero but it increases linearly with distance n measured from this plane. Thus Equation (2.12) may be rewritten as:

$$\frac{1}{R} = \frac{2\varepsilon}{t_s} = \frac{\varepsilon_s(n)}{n} \tag{2.13}$$

In a 3D isotropic system, the relationship between stress and strain is represented by the following equations [112]:

$$\varepsilon_x = \frac{1}{E}(\sigma_x - v\sigma_y) \tag{2.14}$$

$$\varepsilon_y = \frac{1}{E}(\sigma_y - v\sigma_x) \tag{2.15}$$

$$\varepsilon_z = \frac{-v}{E}(\sigma_x + \sigma_y). \tag{2.16}$$

Combining Equations (2.14) and (2.15) yields:

$$\varepsilon_x + \varepsilon_y = \frac{1-v}{E}(\sigma_x + \sigma_y). \tag{2.17}$$

For a 2D isotropic system where $\varepsilon_x = \varepsilon_y$, this equation is reduced to :

$$\varepsilon_r = \frac{1-v}{E}\ \sigma_r \tag{2.18}$$

where $\varepsilon_r = \varepsilon_x + \varepsilon_y$ and $\sigma_r = \sigma_x + \sigma_y$. Using Equation (2.13) and Equation (2.18), it is possible to calculate the biaxial stress in the substrate:

$$\sigma_S(n) = \left(\frac{E}{1-v}\right)\varepsilon_s(n) = \ (\frac{E}{1-v})\frac{n}{R}. \tag{2.19}$$

By substituting this equation into Equation (2.11), the bending moment on the substrate can be expressed as:

$$M_s = b_s \int_{\frac{-t_s}{2}}^{\frac{t_s}{2}} n\sigma(n)\, dn = \left(\frac{E}{1-v}\right)\frac{b_s t_s^3}{12R}\ . \tag{2.20}$$

By substituting Equation (2.20) and equating M_s to M_f, the bixial stress on the film can be calculated from the following equation [106]:

$$\sigma_f = \left(\frac{E}{1-v}\right)\frac{t_s^2}{6Rt_f} \tag{2.21}$$

This equations clearly demonstrates the feasibility of determining the stress in the film by measuring the radius of curvature of the beam (R) (i.e. microcantilever), which can be obtained from the microcantilever deflection. The other parameters such as Poisson's ratio and Young's modulus are known for many materials, making the use of this equation with microcantilever sensors a versatile method of measuring stresses in thin films. The relationship between the radius of curvature and the microcantilever deflection is outlined in the following discussion.

Prior to the adsorption process on the microcantilever surface, the surface stress is assumed to be the same on both sides and thus no bending moment in the microcantilever would be induced. When molecular adsorption takes place on one surface of the microcantilever, a differential surface stress between the two surfaces will be formed, inducing a bending moment which causes the microcantilever to deflect. This deflection which may result as a response to either thin film deposition or molecular adsorption can be approximated as a circular arc with a radius of curvature R (See Figure 2.6) [112]:

$$\frac{d^2z}{dx^2} = \frac{1}{R} = \frac{M}{E^*I} \tag{2.22}$$

where z represents vertical deflection of the microcantilever, M is the microcantilever beam's bending moment, E^* is the effective (biaxial) modulus and I is the area moment

of inertia. Equation (2.22) is also known as the general differential equation of an elastic curve. The biaxial modulus E^* can be related to the Young's modulus E by:

$$E^* = \frac{E}{(1-v)} \tag{2.23}$$

where v is Poisson's ratio. For a rectangular microcantilever, the area moment of inertia may be expressed as [112]:

$$I = \frac{bt^3}{12} \tag{2.24}$$

where b and t are the microcantilever's width and thickness, respectively.

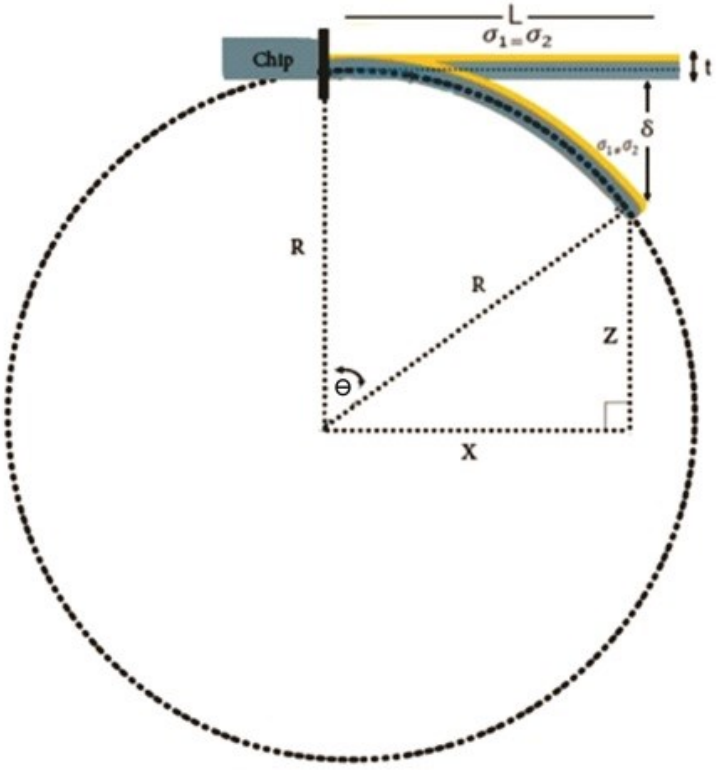

Figure 2.6: Schematic depiction of the microcantilever deflection. The shape of the bending can be approximated by a circular arc with a radius of curvature *R* [113].

Substituting Equations (2.11), (2.23), and (2.24) into Equation (2.22) results in the equation for the radius of curvature of the microcantilever in terms of the differential surface stress:

$$\frac{1}{R} = \frac{6(1-v)}{Et^2}\Delta\sigma \tag{2.25}$$

In order to simplify the quantitative analysis of a microcantilever deflection, several assumptions are usually made [77]. First it is assumed that the microcantilever deflection is very small compared to its length, which itself is larger than the width and thickness of the microcantilever. Based on this assumption, the radius of curvature of the microcantilever beam is assumed to be constant. The first integration of Equation (2.22) yields the slope of the deflection curve $\frac{dz}{dx}$, which, for a small cantilever deflection, is approximated to be equivalent to the deflection angle θ:

$$\frac{dz}{dx} \approx \tan\theta \approx \theta = \frac{Mx}{E^*I}. \tag{2.26}$$

The second integration of Equation (2.22) results in the microcantilever deflection δ at a position x:

$$\delta = \frac{Mx^2}{E^*I}. \tag{2.27}$$

The radius of curvature R can be related to the deflection angle of the microcantilever θ by:

$$R = \frac{L}{\theta}. \tag{2.28}$$

It can be inferred from Figure 2.6 that the radius of curvature R is related to microcantilever deflection δ [113,114]:

$$R = \sqrt{x^2 + z^2} = \frac{L^2}{2\delta} + \frac{\delta}{2} \approx \frac{L^2}{2\delta}\ . \tag{2.29}$$

Combining Equation (2.28) and Equation (2.29), we obtain

$$\theta = \frac{2\delta}{L}. \tag{2.30}$$

This equation shows the relationship between the deflection angle θ and the microcantilever deflection δ. Substituting Equation (2.29) into Equation (2.25), the relationship between the radius of curvature, microcantilever deflection and the differential surface stress can thus be obtained:

$$\delta = \frac{3\,(1-v)L^2}{Et^2}\Delta\sigma\ . \tag{2.31}$$

The difference between Equation (2.21) and Equation (2.31) is that the former is exclusively used to determine the surface stress that results from the deposition of thin

films and considers both the thickness of the film and that of the substrate. Equation (2.31) is used for the determination of the surface stress or microcantilever deflection caused by molecular adsorption and only the thickness of the substrate (microcantilever) is taken into account.

2.3 Self-Assembled Monolayer (SAM)

Of the many molecular self-assembly methods [115,116], self-assembled monolayers (SAMs) have drawn considerable attention due to their many applications in a wide range of fields including physics, chemistry and biology [117,118]. SAMs have been involved in many practical applications including the investigation of surface properties such as wetting, corrosion and friction [119]. The increasing interest in SAMs which have made them an integral part of nanotechnology and surface engineering studies is attributed to their distinguishing characteristics. One of which is that the preparation of SAM can be performed with a straightforward protocol. A well-defined SAM can be prepared simply by immersing a solid substrate into a solution containing the molecules to be assembled. In contrast to other assembly techniques such as Langmuir–Blodgett which requires specialized and complex instrumentation for the preparation for monolayers which are often unstable, SAMs provide highly ordered and stable monolayers by simple preparation methods [120]. The compatibility of most of SAMs with many surface characterization techniques such as X-ray diffraction, cyclic voltammetry and scanning probe microscopy have increased the interest on SAMs. The successful employment of

SAMs in the fabrication of nanodevices such as nanosensors and nanoresistors has made SAMs as one of the most cost-effective and promising technologies in semiconductor electronics industry [121].

SAMs are defined as the spontaneous organization of molecules into highly ordered and oriented structures on a surface. The assembly of molecules into highly stable, organized and low energy state structures is governed and promoted by the chemisorption process such as chemisorption of thiols on gold and intermolecular forces such as Van der Waals forces, hydrogen bonding, and electrostatic interactions [122,123]. There have been two extensively studied systems of SAMs, namely Thiol-based SAMs and Silane-based SAMs. The main components of a SAM, shown in Figure 2.7, consist of the following units:

1- The substrate onto which the molecules constituting the SAM form. There are several substrates that support the formation of SAMs. Hydroxylated surfaces such as glass, SiO_2, Al_2O_3 [124] as well as gold [125], silver and copper [116] have been commonly used as SAM substrates. Nanostructures such as colloids and nanocrystals are also types of SAMs substrates [119]. The selection of the appropriate substrate depends on the application for which a SAM is used. For example, thin metals films supported on silicon wafers are widely used in many applications as sensors [116].

2- The headgroup or ligand which allows the binding of the receptive molecules onto the substrate. The specific and high affinity of such groups towards the substrate is the driving force behind their attachment to the surface. There are a number of functional groups that can be used to anchor the molecules to a surface. Thiols, amines and sulphides are the most stable and extensively used headgroups for the formation of SAMs. One of the largely investigated SAMs is the assembly of alkanethiols onto noble metal surfaces [126]. In this assembly, the high affinity of sulfur for the gold surface makes it possible to form a highly stable and compact SAM. Other examples of headgroups include the binding of organosilanes onto hydroxylated surfaces via Si-O bond [115]. It has been reported that the SAM's orientation, compactness, and packing density is greatly affected by the interaction strength between the headgroup and substrate [115,116]. An example of strong headgroup-substrate interactions is the S-Au interaction which has an energy of about 190 kJ/mol, making it one of the most stable and strong binding groups for SAMs [127].

3- A spacer is the component responsible for the connection of the ligand to the endgroup. The spacer is the main factor that determines the thickness of the SAM on the substrate. It also affects the orientation of the molecules on the surface. A common example of the spacer chain is the methylene groups, which is the major constituent of the alkanethiols.

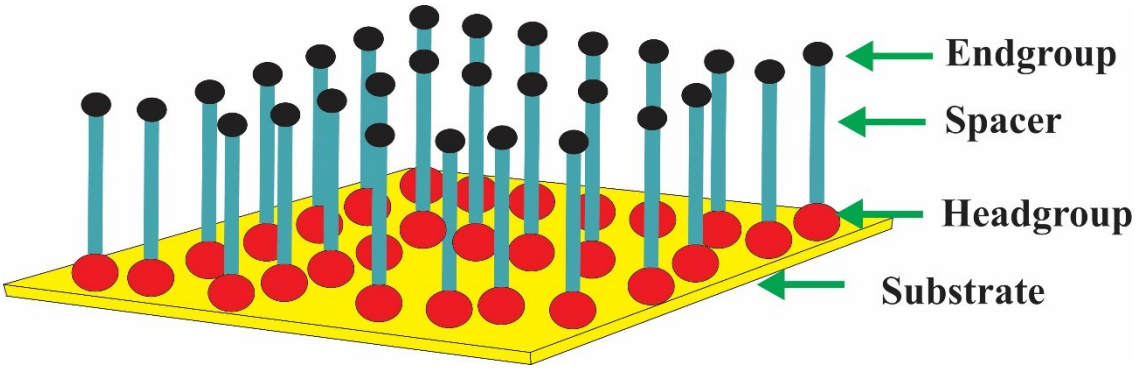

Figure 2.7: Schematic of the main components of SAM.

4- The endgroup provides the platform for incorporating many chemically-synthesized functional groups. Examples of such functional groups include CH_3 or COOH. The endgroup can also be modified so as to act as a binding site for target analyte to be recognized. For example, macrocyclic compounds such as crown ethers have been extensively employed for the selective binding with metal ions [128].

2.3.1 Thiolates-derived SAMs on Gold

A fundamental understanding of the mechanisms that drive the self-assembly process is imperative in order to achieve a well-structured and uniform SAM on the substrate. Such understanding is also important to gain insight into the mechanism of the adsorption-induced surface stress. There have been several literature reports devoted to the study of SAM formation on metallic surfaces [129]. Early literature studies were focused on the

SAM formation on metal surfaces caused by organosulfur compounds such as thiols, disulfides, sulfides [116]. Subsequent studies have started measuring the surface stress associated with the formation of SAM on metal substrates [130]. Among other metallic surfaces such as silver and copper, gold has been widely selected as the preferred substrate for SAM formation. One of the appealing characteristics of gold is its reasonable chemical inertness. Gold does not react with many chemicals and does not easily oxidize. These properties make it possible to conduct experiments under ambient conditions. The ease of producing thin films of gold onto solid substrates using either thermal evaporation or sputter deposition is another attractive characteristic of gold.

Most of the present knowledge about SAM-induced surface stress stems from studies conducted on the alkanethiol SAMs on gold. The formation of alkanethiol ($HS(CH_2)_n$ X), where n is the number of methylene units and X is the end group of the alkyl chain, SAMs on gold surfaces has received considerable attention and has been viewed as a model system for SAM studies [131]. The compactness, stability and simple chemical composition of alkanethiol SAMs have attributed to their wide and extensive investigation. A typical alkanethiol, schematically shown in Figure 2.8, consists of a thiol binding group (HS) for attachment to the gold surface, methylene groups $(CH_2)_n$ and a functional end group which can be designed to produce any surface chemistry. The investigation of the self-assembly of alkanethiols on gold surface is crucial as it helps to understand the factors that govern and influence the orientation of molecules on a surface. More specifically, the mechanism of the interaction between gold and sulfur which is the most common functionalization method used for attaching chemical and

biological molecules onto gold surface can be better understood from these studies. The immobilization of thiols onto gold takes place via a S-Au bond. The adsorption mechanism between Au and S takes the following form:

$$RSH + Au \rightarrow RS–Au + e^{-} + H^{+}$$

It is assumed that upon adsorption of thiol on gold, the thiol group is deprotonated (e.g. loss of the hydrogen) and that the thiol chemisorbs to the gold surface via the formation of a covalent Au-S bond. The strong interaction between sulfur and gold during alkanethiol formation has been found to cause the ejection of gold atoms from the surface, creating etch pits on the Au surface [130].

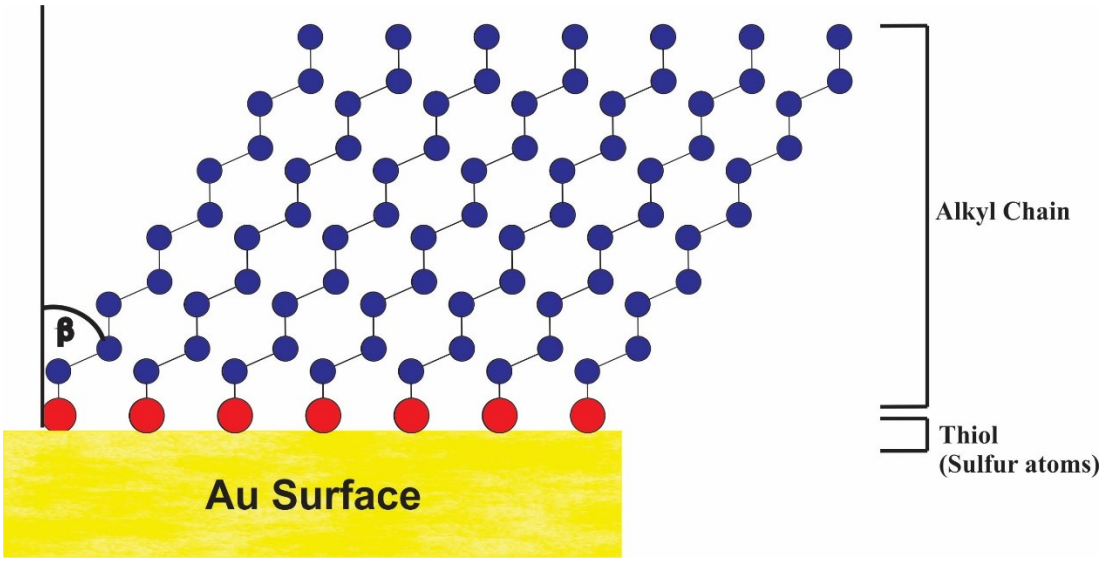

Figure 2.8: A schematic illustration of alkanethiols SAM on gold. Typically, an alkanethiol molecule consists of a thiol binding group (HS) and an alkyl chain.

It has been revealed by STM studies that a typical alkanethiol monolayer forms a ($\sqrt{3} \times \sqrt{3}$) R30° structure on gold with a $C(4 \times 2)$ periodicity [132]. The alkyl chains were found to be tilted by approximately 30 degrees, depending on the chain length, from the surface normal. Such structure was also confirmed by Strong and Whitesides [133] who used the electron diffraction technique and found that the intermolecular spacing between adjacent alkanethiols is around 0.497 nm.

The formation process of alkanethiol SAMs has been intensively investigated both theoretically and experimentally. It has been proposed that the formation process takes place in two distinct stages. The first stage which is called the *lying-down* stage is a rapid process where alkanethiol molecules lie parallel to the gold surface. The growth of the lying down phase can be completed in a matter of a few minutes and is a result of chemisorption between the sulfur and gold. The second stage of the alkanethiol formation is a slow adsorption step during which the transition from the *lying-down* structure to *standing-up* stage occurs. In this stage, the alkyl chains of alkanethiol molecules assemble themselves in an angled orientation on the gold surface. Upon the completion of this stage which can take up to a day or more, a highly ordered SAM of alkanethiol is obtained. Despite the fact that many studies have confirmed the occurrence of these two phases during the formation of alkanethiol SAM on Au, the issue of determining the exact binding site of alkanethiol molecules on a gold surface is still unresolved [134]. Nevertheless, it was suggested that alkanethiol molecules preferably adsorb on hollow sites on fcc which is proposed to be the most stable with minimum energy binding site of the Au(111) surface [135].

The adsorption and growth kinetics of alkanethiol SAMs have been found to be greatly affected by several factors. A comprehensive understanding of the assembly of SAMs can be developed by careful investigation of these factors and these effects on the assembly process. As reported by Schwartz [136], the morphology and cleanliness of the gold substrate, concentration of the adsorbate, and temperature are some of the factors that influence the SAM behavior on gold surface. Godin *et al.* [137] also conducted an investigation on the factors that influence the kinetics of the formation of self-assembled monolayers of alkanethiol on gold-coated microcantilevers and the associated surface stress. They identified that the gold grain size has a significant influence on the formation process of SAMs, supporting the experimental finding reported by Schwartz. Godin has however found that the chain length of the alkanethiol molecule had no effect on the surface stress induced by the SAM. The role of other parameters such as the immersion time, chain length, and purity of the adsorbates were also shown to be influential on the structure and properties of SAMs [116]. Although there have been contradictory reports on the literature about the mechanism that drive the SAM formation of alkanethiols, fairly sufficient understanding about this mechanism has been established which has helped to gain more insight into the mechanism of SAM-induced surface stress.

2.4 Adsorption-Induced Surface Stress

Most of the current knowledge about the origin of surface stress caused by molecular adsorption is obtained from microcantilever sensing experiments [77]. Microcantilever

sensors have proven to be well suited for measuring surface stress. Despite the increasing number of reports in the literature on the use of microcantilever sensors to detect changes in surface stress, a quantitative understanding of the origin of adsorption-induced surface stress is not yet resolved [138]. The fundamental physical origin of adsorption-induced surface stress, from the available studies on molecular interactions by microcantilever sensors, has been described by several mechanisms. The present understanding of the origin of adsorption-induced surface stress has been primarily obtained from DNA hybridization and alkanethiol adsorption studies [139]. The study conducted by Fritz *et al.* [109] was the first that investigated the origin of surface stress formed during DNA hybridization. They attributed the formation of surface stress mainly to electrostatic, steric and hydrophobic interactions that occur between the DNA strands on the microcantilever surface. They also found that the microcantilever deflected downward, indicating the induction of a compressive surface stress as a result of DNA hybridization. In contrast, Wu *et al.* [140] observed that DNA hybridization caused the microcantilever to deflect upward, which means that a tensile surface stress was formed. They agreed that besides electrostatic and steric interactions, the configurational entropy should be taken into account as a cause of the surface stress induced during DNA hybridization. The authors stressed that the magnitude and sign of the microcantilever deflection caused by the formation of surface stress due to DNA hybridization is affected by several other factors such as buffer concentration and temperature. In a separate study, Mertens *et al.* [141] claimed that the microcantilever deflection generated during DNA hybridization can be caused by the hydration forces between the DNA strands. Watari *et al.* [142]

attempted to explain the physical origin of surface stress induced during the pH variation of the buffer solution on thiolated alkane chains functionalized on a microcantilever surface. They observed microcantilever deflections at different pH values and attributed these results to the electrostatics, ionic hydrogen bonds and the effect of the counter ions. In efforts to further understanding the origin of surface stress induced during molecular adsorption, Godin *et al.* [137] presented a study which examined the effect of several mechanisms as possible origins of the induced surface stress during the formation of alkanethiol SAMs. The authors considered the contribution of the following three forces on the generation of surface stress caused by the self-assembly of alkanethiol: Lennard-Jones interactions, intermolecular electrostatics, and the changes in electronic density at the gold surface. They found that the greatest contribution to the overall induced surface stress was observed by changes in electronic density of the gold surface atoms, whereas the effect of Lennard-Jones interactions and the electrostatics interactions between the adsorbed molecules was minimal. These findings were consistent with the description provided by Ibach [84] about the possible mechanism of the adsorbate-induced surface stress, where it is stated that the electronegativity of the adsorbate with respect to the substrate, as the case with Au^{+} S^{-} bond, causes charge to be removed from the bonds between the surface atoms of the substrate. This removal would reduce the inherent tensile stress and lead to the formation of compressive surface stress. These experimental results supported with theoretical models can be used for the interpretation of surface stress. These experimental findings can also be helpful to provide an explanation about

the formation of tensile or compressive surface stress observed during molecular sensing experiments.

From the preceding discussions, it is obvious that different reaction systems were employed in the efforts to develop a better understanding about the origin of adsorption-induced surface stress. However, these studies showed that there might be several sources of surface stress, exhibiting the difficulty and complexity of the formation mechanism of surface stress. In addition, the contradicting results of Fritz and Wu which showed different results for two similar experiments indicate that the mechanism of surface stress at the molecular level still remains ambiguous. It is therefore concluded that a systematic theoretical and experimental investigations of more reaction systems is needed in order to gain new insights into the physical origin of surface stress.

Part I

Experimental Studies Using Single Microcantilever System

Chapter 3 Experimental Apparatus and Techniques

The underlying goal of this research is to investigate the binding capabilities of calixarene-modified microcantilevers towards specific metal ions. The achievement of this goal has been conducted on two experimental systems. The first experimental platform relies on the use of a single active and reference microcantilever mounted in different positions. In this system, only one active and one reference microcantilevers can be used at a time. The second experimental system, which is discussed in *Chapter 6*, uses two 8-microcantilever arrays where active and reference microcantilevers are on the same chip, allowing several active and reference microcantilevers to be tested at the same time.

Both sensing systems consist of four main elements:

1. The measurement cell which houses the microcantilever sensors.
2. The optical system which monitors the microcantilever response during sensing experiments. This system includes the optical focusers and the PSDs.
3. Electronic system which is used to acquire and process the signal produced by the PSDs.
4. Fluid delivery system which is used for introducing of the target solutions into the measurement cell.

In this chapter, a brief introduction of the first experimental platform will first be given. The optical beam deflection system which has been used for the detection of the microcantilever deflection will then be discussed. The other experimental techniques that were used during the course of this work such as the scanning tunneling microscopy (STM), atomic force microscopy (AFM) and sputter deposition will also be discussed.

3.1 Single Microcantilever Experimental Set-up

The microcantilever setup used in this work (see Figure 3.1) consists of a fluid cell, optical focusers, PSDs and an optical microscope. The fluid cell, which houses the microcantilevers, was made of aluminum which is not known to react with reagents used in this work. The fluid cell is connected to two PEEK tubes where one tube is responsible for transporting the solution from the syringe pump into the fluid cell while the second tube transports the solution out of the cell. The fluid cell can be sealed with a viton o-ring and a specially made glass cover coated with two antireflective coatings to prevent the laser bean from reflecting from the air/glass and the glass/water interface. Once the microcantilever sensor was placed in the fluid cell and covered with the glass cover, the laser beams were focused on the free end of the microcantilevers using optical focusers. The reflected beams from each microcantilever were directed into two separate PSDs. In order to ensure that the laser beam was on the desired position (e.g. apex) on the microcantilever surface, an optical microscope placed above the experimental set up (see Figure 3.1) was used. When the laser beam hits the PSD, a photo current is generated

which is then converted into a voltage signal by an amplifier. The output voltage is directly related to the beam spot on the surface where a +/- 5 mm position on the PSD surface corresponds to +/- 10 V. The output voltage signals are then read by the data acquisition board interfaced to a computer.

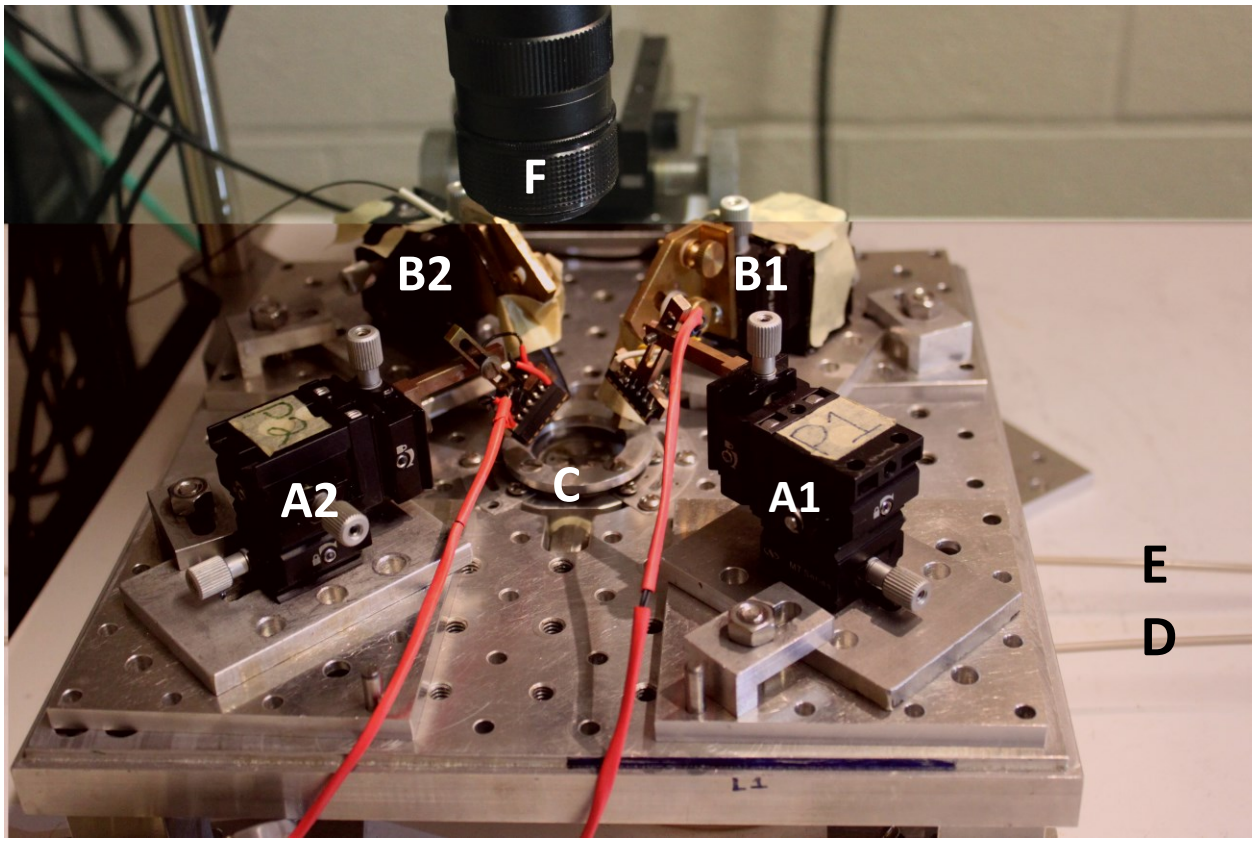

Figure 3.1: A photograph of the microcantilever sensor setup. A1, A2, B1, B2) Translation stages, C) Fluid cell, D, E) Input and output tubes. F) Optical Microscope placed above the fluid cell used to view the position of the optical beam on the microcantilever surface.

3.2 Optical Beam Deflection System (OBDS)

The optical beam deflection system is one of the most established methods used to monitor the microcantilever deflection (see Figure 3.2). The optical beam deflection system has been studied extensively and the relation between the microcantilever deflection and the PSD signal has been well-defined [143-145]. It has been suggested that the microcantilever deflection δ is proportional to the beam displacement on the PSD surface (Δh) through the following equation [145,146]

$$\delta = \gamma \, \Delta h. \tag{3.3}$$

where γ is a geometrical factor that needs to be determined in order to relate the microcantilever deflection to the acquired PSD signal. The beam displacement on the PSD surface (Δd) is calculated from the currents I_1 and I_2 and the effective length of the PSD l.

$$\Delta h = \frac{I_1 - I_2}{I_1 + I_2} . \frac{l}{2} \tag{3.4}$$

Several investigations have been conducted in order to estimate the value of γ which is highly dependent on the geometry of the set-up. The general strategy of calculating this factor considers that the angle of the microcantilever deflection is small and could be assumed to be half the deflection angle of the laser beam $\boldsymbol{\theta}$ as shown in Figure 3.2 [146]. This assumption leads to the determination of γ to be:

$$\gamma = \frac{L}{4s}. \tag{3.5}$$

where L is the microcantilever length and s is the distance between the microcantilever and the PSD

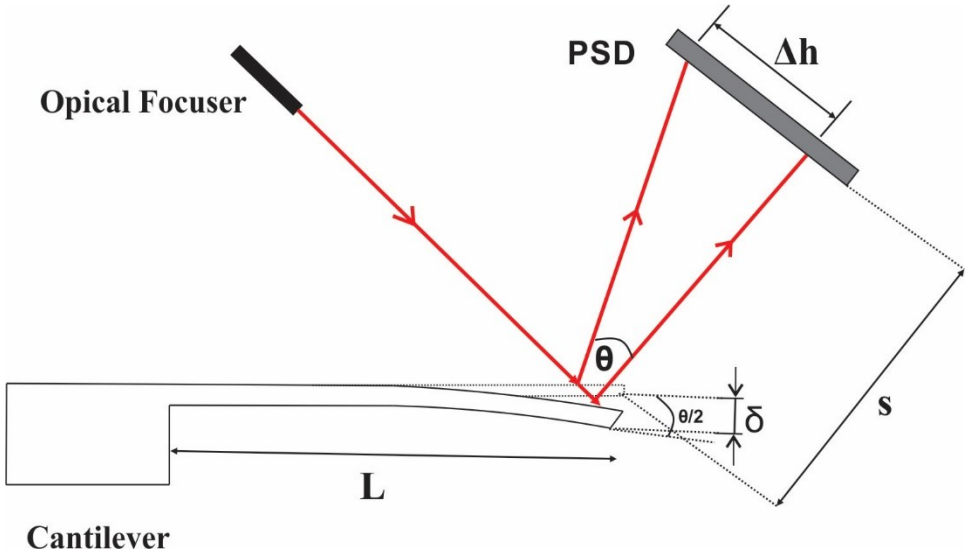

Figure 3.2: A depiction of the optical beam deflection system (OBDS).

Combining (3.3), (3.4) and (3.5) gives an equation relating the microcantilever deflection to the PSD signal:

$$\delta = \left(\frac{L}{4s}\right)\left(\frac{I_1 - I_2}{I_1 + I_2}.\frac{l}{2}\right). \tag{3.6}$$

Although this equation is used extensively in the microcantilever sensor community, other studies have improved this relation. Beaulieu *et al.* [143] developed a geometrical method that completely describes the OBDS, taking into consideration all angles related to the microcantilever deflection. They have also written a program that converts the acquired PSD signal into a microcantilever deflection. The aforementioned equations and research investigations have only considered the case when the microcantilever is operated in air. However, when operating in liquid, it is important to take into account the effect of the refractive index of the solution in which the microcantilever is immersed. When operating the optical beam deflection system in liquid, the optical path of the laser beam changes due to the presence of the air/glass and glass/ liquid interfaces, as depicted in Figure 3.3.

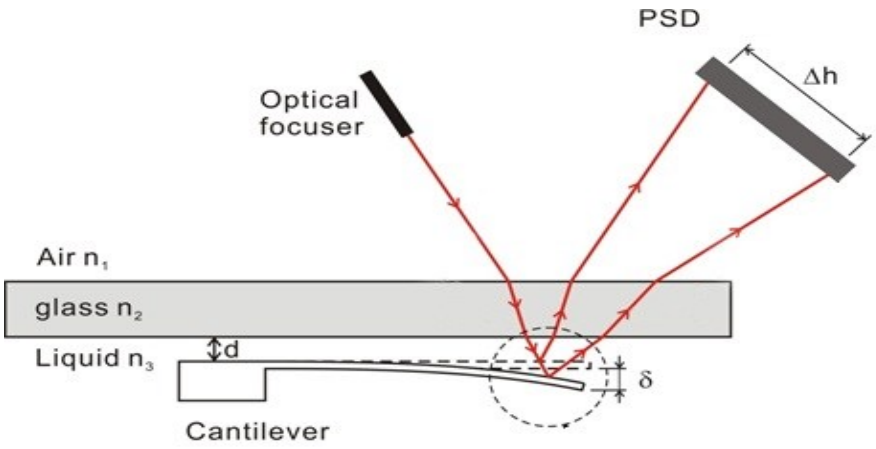

Figure 3.3: Diagram of the optical beam deflection system (OBDS). The laser beam path changes as it passes the air-glass boundary and liquid-glass boundary, stressing the importance of taking the thickness of glass into account when calibrating the OBDS.

The determination of the geometrical factor γ from Equation (3.3) for experimental systems operating in liquid has been discussed in several literature reports [147-149]. Lang *et al.* [149] derived a relationship between the radius of curvature R of the microcantilever and the displacement of the light spot Δh on the PSD as follows:

$$\frac{1}{R} = \frac{2\delta}{L^2} = \frac{\Delta h}{2sn_s}. \tag{3.7}$$

where s is the distance between the microcantilever and the PSD, and n_s is the refractive index of the solution on which the microcantilever is immersed. Although this relation considered the refractive index of the solution, it neglects the effect of the optical window which causes refraction of the laser beam. This relation is only restricted to the case of normal incidence where the incident laser beam is perpendicular to the optical window. This complete neglect of the effect of the optical window by making no reference to the refractive index of the glass window could result in an error of about 25-30% in the determination of the microcantilever deflection [150]. In a different work, Rokob *et al.* [151] derived a relationship between the radius of curvature of the microcantilever and the position of the laser beam on the PSD assuming nonnormal incidence of the laser beam on the optical window. They found that an additional term has to be added to Equation (3.7) which takes into account the angle of incidence of the light beam φ :

$$\frac{1}{R} = \frac{2\delta}{L^2} = \frac{\Delta h}{2Lsn_s}\left[\frac{(1-\sin\varphi^2)^{\frac{3}{2}}}{(1-{n_s}^{-2}\sin\varphi^2)^{\frac{1}{2}}}\right]. \tag{3.8}$$

This equation implies that it is very important to consider the angle of laser beam incidence. This indicates that the assumption made by some authors [149] that the laser beam is normal to the optical window, which is not the case in reality, to simplify the calculations could result in a large systematic error [151]. Despite the fact that the derivation of Equation (3.8) took into consideration the effect of the angle of the incidence of the laser beam, it neglected the influence of the thickness of the optical window, making it inaccurate for the cases where optical window is used.

Xiao *et al.* [152] have comprehensively investigated multiple optical arrangements taking into account all factors that can influence the determination of microcantilever deflection in liquid which were ignored in the previous derivations. It was stated that the position of the laser beam undergoes a lateral shift on the PSD surface because of the change in the beam direction caused by the glass thickness. For an optical arrangement where the laser beam passes the air-glass boundary and glass-water boundary, the relationship between the microcantilever deflection δ and the lateral shift of the laser beam on the PSD Δh can be expressed as:

$$\frac{2\delta}{L^2} = \frac{2\emptyset}{L} = \frac{\Delta h}{Ls}\left[\frac{1}{\left(\frac{d_s}{s} + n_s\frac{d_a}{s} + \frac{n_s}{n_g}\frac{d_g}{s}\right)}\right]. \tag{3.9}$$

where s is the distance between the microcantilever and the PSD, d_a, d_s and d_g are the distance between the microcantilever beam and the inner glass, the distance between the outer glass surface and the PSD, and the thickness of the glass window, respectively, n_s

and n_g are the refractive indexes of the liquid solution and the glass, respectively. The derivation of Equation (3.9) took into account all reflection and refraction angles of the laser beam which were then associated to the deflection angle of the microcantilever ∅. For the optical arrangement used herein, the geometrical factor was calculated to be γ =5.20 × 10^{-6} $\frac{m}{V}$, taking into account that the PSD has a linear response of units as 5 ×10^{-3} $\frac{m}{V}$.

The frequent use of OBDS is due to the fact that this technique is simple and has a great lateral resolution [153]. Even though the PSD signal (in volts) can provide information about the microcantilever behavior during experiments, microcantilever deflection measurements provide much more useful information. In quantitative analysis of the probe-target interaction events on the microcantilever surface where some important parameters such as the binding constant or Gibbs free energy to be evaluated, the voltage signal of the PSD will not be useful and thus the actual microcantilever deflection is required [94,96]. The microcantilever sensing results have also been widely quoted in surface stress units [137,154]. The conversion from microcantilever deflection (Δδ) into change in surface stress (Δσ) is completed through Stoney's equation (see Equation 2.32). This equation takes into account all microcantilever parameters which can be estimated. The reason for expressing the microcantilever response in surface stress units is to compare such values to theoretical models which are often conducted in units of surface stress.

3.3 Sputter Deposition

Sputter deposition is a powerful method of depositing thin films onto a substrate by the use of a glow discharge. In this work, a sputter deposition system was used to deposit thin films of inconel and gold on microcantilevers. Sputter deposition system possesses several advantages making it a desirable technique for thin film deposition. One of the main advantages of sputtering is it allows for accurate control of the deposition conditions such as power and gas flow. A sputter deposition also allows the control of the film characteristics such as thickness and roughness. Since the sputter deposition system is based on a kinetic process rather than a chemical one, any material can, in principle, be sputtered onto a substrate. The sputtering machine consists of five main components: a target material, substrate, vacuum chamber, magnetrons and a pumping system. Both the target material which is the cathode and substrate which is the anode are mounted inside the vacuum chamber as shown in Figure 3.4a. Magnetrons are mounted parallel to the target and are used in order to create a magnetic field near the target. The vacuum chamber must first be evacuated to a pressure of 10^{-6} Torr, which can be measured using a pressure gauge connected to the chamber. During the sputtering process, argon gas is introduced into the chamber and then becomes ionized by an electric field. The ionized argon atoms collide with the target atoms causing them to eject and deposit onto the substrate surface creating a thin film of the target material. The collision between argon gas and the target leads to the emission of secondary electrons, which can participate in the ionization process by ionizing neutral argon atoms in the plasma. The magnetic field

created by the magnets leads to the capture of electrons near the cathode, causing them to undergo a circular path in the target region (see Figure 3.4b)[155]. This confinement of electrons near the target amplifies the ionization density which, in turn, increases the deposition rate.

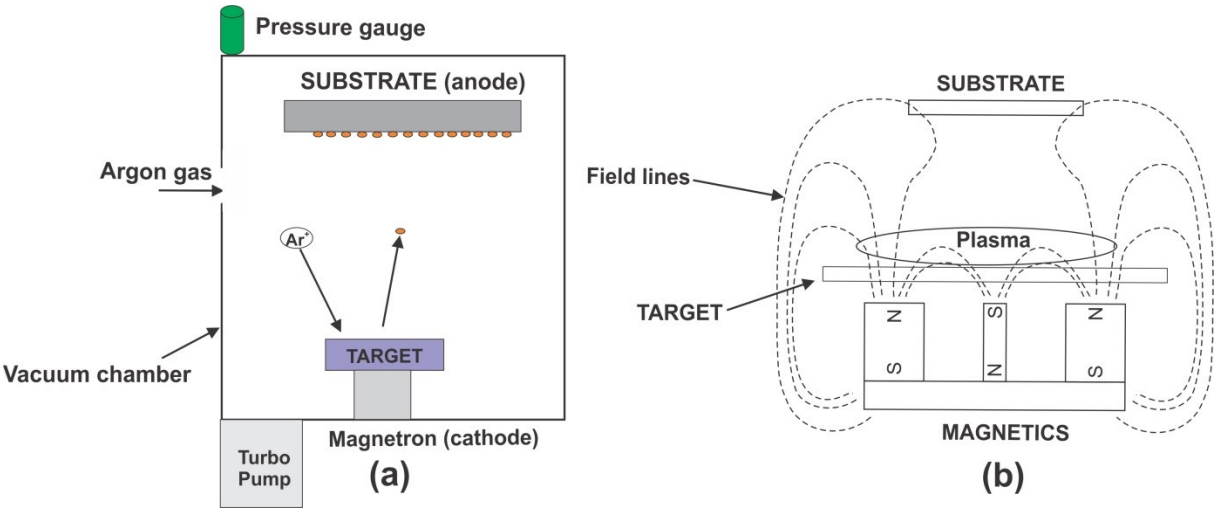

Figure 3.4: (a) A schematic representation of the basic components of a sputtering deposition system. (b) The magnetic field produced by the magnetrons traps the argon ions (plasma) and secondary electrons in the vicinity of the target. The electron participation in the ionization process increases the plasma which, in turn, increases the sputtering process.

3.4 Scanning Tunneling Microscopy (STM)

STM belongs to the family of scanning probe microscopes (SPM) which is widely used to study the surface properties of materials. The SPM family also includes the Atomic Force Microscopy (AFM) and Magnetic Force Microscopy (MFM). STM was invented by Gerd Binning and Heinrich Rohrer to whom the Nobel Prize was awarded in 1986 for its invention [156]. Figure 3.5 shows a schematic representation of the main components of an STM. The STM comprises five major components: the tip, piezoelectric scanner, current amplifier, bias, and feedback loop.

The STM operating principle relies on a quantum mechanical effect called *Quantum Tunneling*. When the tip is brought in close proximity to the sample surface, a small current flows through the gap between the tip and the sample due to the applied bias. This phenomenon is called Quantum Tunneling. The current flowing through the gap is called the tunneling current and is monitored to create the image. This current is exponentially dependent on the distance between the tip and the sample which is required to be a conductor or a semiconductor. It also depends on the applied voltage and on the height of the barrier (energy barrier). The STM probe (tip) is made of a stable and conducting material such as Pt/Ir. It is crucial for the tip to be sharp to obtain a good image resolution and to prevent various tip effects from occurring. An example is the double tip effect which results in indistinct images and is due to the fact that more than one portion of the tip can participate in the tunneling process.

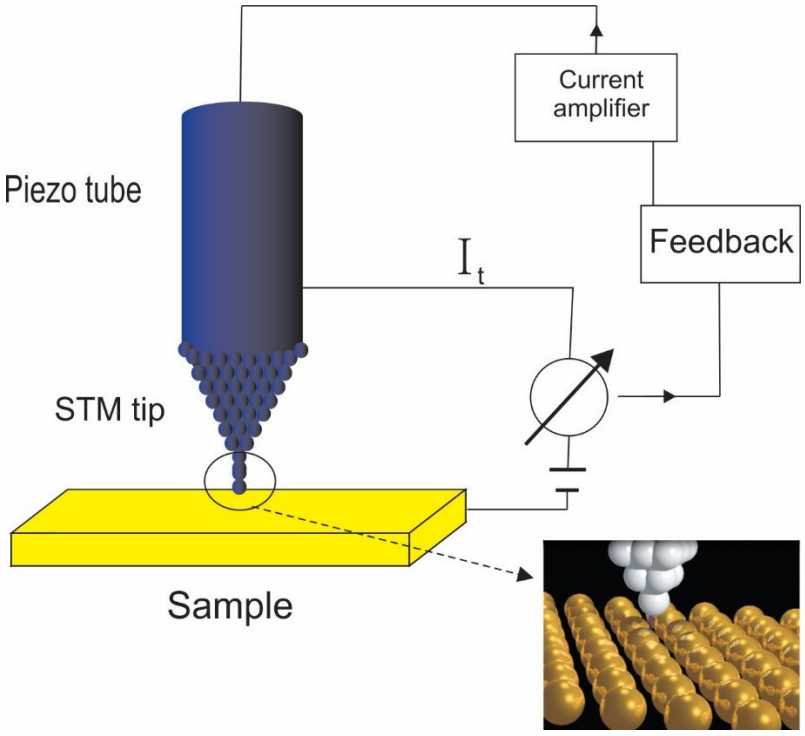

Figure 3.5: A depiction of the main components of the scanning tunneling microscopy (STM).

During the imaging process, the tip scans over the sample with the use of a piezoelectric scanner. The STM is predominantly operated in two modes: constant current mode and constant height mode. In the former mode, the current is held constant by the feedback loop while the height is changed by the piezoelectric scanner. The change in height is used to create the image of the surface. Despite the fact that in this mode the scanning takes longer, it is the preferred mode for most cases. In the latter mode, the current change leads to the construction of the image while both voltage and the height are being

held constant. Imaging using this mode is faster since the scanner is held constant (no up and down movements) and is preferred for performing atomic resolution imaging over small surfaces.

3.5 Atomic Force Microscopy (AFM)

One of the limitations of STM is that it can only be applied to conductive materials since it images the surface properties by detecting changes in current. This limitation has been overcome by the subsequent development of the atomic force microscope which images the surface properties by detecting changes in the forces on the sample surface [157]. AFM is one of the versatile tools for imaging surface topography and probing the surface mechanical properties with very high resolution. The AFM has several imaging modes which are used depending on the application of interest. The most common mode is the contact mode where the cantilever deflection is kept constant while the tip scans over the sample. Soft cantilevers with very low spring constant are normally used in this mode for investigating rough surfaces [158]. The second AFM operation mode is the non-contact mode, where the cantilever is oscillated at or near its resonance frequency and changes in oscillation amplitude is used to generate the image. The third imaging mode combines both features of the first and the second mode and is termed as the tapping mode. In this mode, the oscillating cantilever makes intermittent contact with the surface. This mode overcomes the disadvantage of contact mode in which excessive forces is exerted on the

sample which could potentially damage it. Both non-contact and tapping mode are widely used for imaging soft materials such as DNA and polymers [159].

In this work, AFM was primarily employed for determining the spring constant of array-based microcantilevers. The spring constant of single microcantilevers, which were used in the experimental system described in section 3.1, was not measured due to the unavailability of the AFM system when the experiments involving single microcantilevers were conducted. Commercially available microcantilever sensors are often taken from silicon wafers comprising hundreds of microcantilevers and thus they are usually shipped with a broad range of spring constant values. Consequently, it was necessary to assess the variability of the spring constant values of microcantilevers within the arrays and correlate the difference in these measured values to the difference in the response values of microcantilever within the array. Here we use the AFM to find the resonance frequency of the microcantilever, from which the spring constant can be determined. As suggested by Cleveland *et al.* [160], the spring constant of a microcantilever k can be estimated by measuring the resonance frequency of the microcantilever f as follows:

$$k = 2\pi^3 l^3 w \sqrt{\frac{\rho^3}{E}} (f)^3. \tag{3.10}$$

where l and w are the microcantilever length and width respectively, ρ is the material density, E is the Young's modulus. Taking advantage of the cantilever tuning feature

provided by the tapping mode in our AFM system, the resonance peak of our microcantilevers can be determined. After the resonance frequency of the microcantilever was found, the spring constant was determined from Equation (3.10). In order to determine the spring constant after the deposition of gold, the method proposed by Gibson *et al.* [161] was used. In this method, the spring constant of the microcantilever can be determined by measuring the resonant frequency before and after the deposition of a thin gold layer. The equation for determining the spring constant in terms of the frequency before and after the addition of gold is as follows:

$$k = (2\pi)^2 \frac{0.24\, l\, w\, t_{Au}\, \rho_{Au}}{(f_2^{-2} - f_1^{-2})}. \tag{3.11}$$

where f_2 and f_1 are the resonant frequencies after and before the deposition of gold thin film, respectively, ρ_{Au} is the gold density, and t_{Au} is the thickness of the gold layer.

Chapter 4 Materials and Experimental Procedures*

This chapter is intended to provide an introduction to calixarenes and the experimental procedures that were followed in the preparation of microcantilevers for sensing experiments. As mentioned previously, this work involved the study of three calixarene compounds whose selectivity and sensitivity towards specific target ions have been investigated using microcantilever sensors. The synthesis of the calixarene compounds was conducted by Dr. Paris Georghiou's group in the Chemistry Department at Memorial University. This chapter will present the structures and the synthesis schemes of the three calixarenes used in this work. In addition, the experimental procedures which were undertaken to prepare active and reference microcantilevers for the single microcantilever experimental setup will be provided. A discussion of the two cleaning methods that were used for cleaning silicon microcantilevers is also given. Experimental results that show the effect of these two methods on the chemically-modified microcantilevers will also be described. Finally, a description of the differential microcantilever signals and how they were obtained will conclude this chapter.

* Parts of this chapter have previously been reported in publications which have resulted from this author's work and are cited as [165], [171] and [172].

4.1 Calixarenes

Calixarenes are synthetically-derived molecules that have drawn substantial interest due to their relative ease of preparation and their ability to be chemically altered resulting in their ability to bind with target ions/molecules [162,163]. Calix[*n*]arenes (where *n* = 4, 6 or 8, represents the number of phenolic rings) are macrocylic compounds which have been widely used in complexation and supramolecular chemical studies, especially in host-guest systems [164]. The calix[4]arene structures are characterized as "cup-" or "basket-shaped" molecules comprising four benzene rings connected by methylene groups as shown in Figure 4.1a. Each benzene ring contains a hydroxyl group (-OH) on the "narrow rim" (or "lower rim") and a tertiary-butyl group [-$C(CH_3)_3$] on the "wide rim" (or "upper rim") [165]. Modifying either the wide or narrow rim appropriately allows the calixarene to be anchored to various substrates, creating highly ordered SAMs.

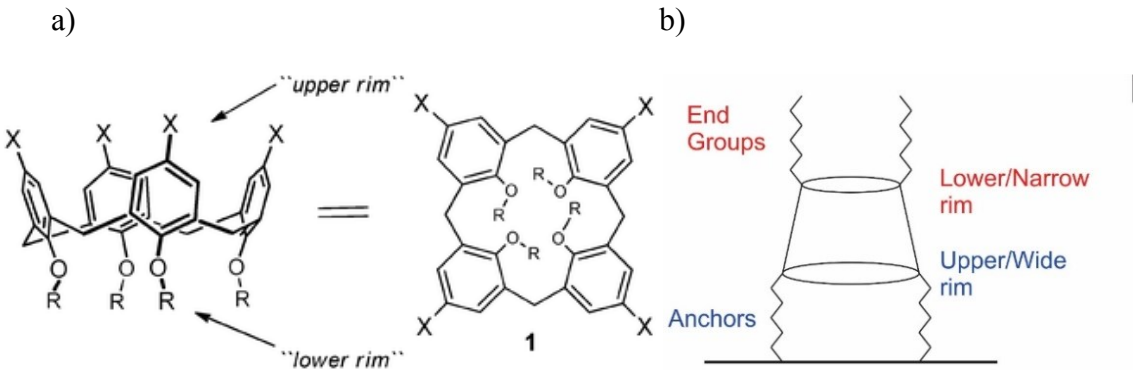

Figure 4.1: a) Two different forms of representations of the general structure of calix[4]arenes (where X and R represent possible functional groups. b) Schematic representation of a calixarene molecule showing the orientation of the "cup" section of the molecule [165].

Because of their basket shape, monolayers with calix[4]arenes are highly stable and can position themselves naturally in a single orientation with the anchors on the substrate and the opposite end groups pointing outward from the substrate, as illustrated in Figure 4.1b. The receptive nature of the molecules to various target ions or molecules can then be accomplished by modifying the lower rim with various receptors or "podands" such as ionophoric chelators and crown ethers [128,166]. The nature of the functional groups on the podands makes such bimodal molecules suitably and selectively receptive to ions of specific size(s) and/or charge(s). Such modified calixarenes have been used to selectively bind to a wide range of cations and anions [167]. The upper rim, on the other hand, can be difficult to modify and require first that the tertiary-butyl groups be removed. Following the removal of this group, the upper rim is typically modified with a thiolate (-$SCOCH_3$) end group which permits the calixarene to self-assemble onto a metallic substrate.

Calix[4]arenes can be synthetically modified so that the final desired structure adopts one of four major conformations. The possibility of obtaining these different conformations is due to the flexibility of calix[4]arene which is mainly attributed to the ease of rotation of the phenolic units around the methylene (–CH_2–) bridges [168]. This has made it possible to produce four distinct types of calixarene orientations: namely *cone*, *partial-cone*, *1,2–alternate*, and *1,3-alternate* conformations, schematically represented in Figure 4.2.

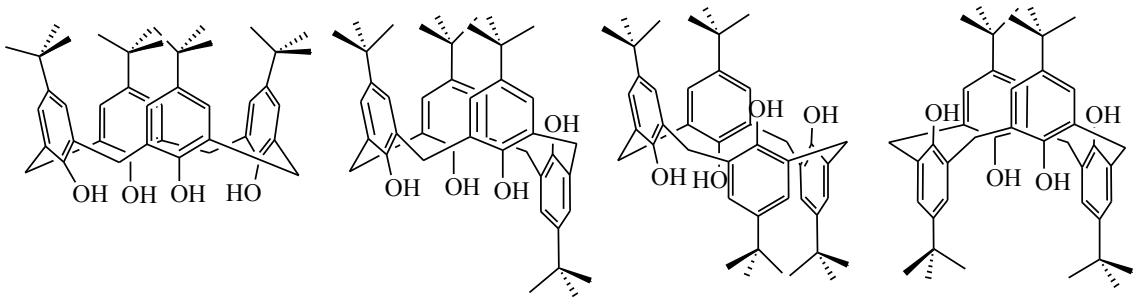

Figure 4.2: The four conformations of a calix[4]arene.

The ability of functionalized calixarenes to recognize and form selective complexes with a wide variety of target analytes such as cations, anions and biological molecules is one of the remarkable features of these compounds. The importance of investigating the interactions between modified calix[4]arenes and target molecules stems from the fact that these interactions can be used to gain an insight into the mechanism of molecular recognition and self-assembly process. For a "host" molecule (e.g. a calixarene) to selectively bind to specific molecular "guest" (e.g. cation, anion or neutral ion), two fundamental concepts should be taken into account, namely *complementarity and preorganization* [169]. These two important factors play a major role in the determination of the host's affinity or suitability towards the particular guest species. In order to achieve the complementarity between the host and the guest, the host should be synthesized with a binding site of the proper size and geometry to interact with the guest of interest. The complementarity between the host and the guest can be incorporated into the system by making the binding sites of the host complementary to the guest geometrically and electronically. The complementarity is highly dependent on the type of the guest. For

example, if the targeted guest is a cation, then the host binding site should have the proper electronic structure (e.g. negatively charged donor atoms). The second key factor characterizing host-guest complexes is the preorganization which is related to the shape and stability of the host. A host is said to be preorganized when the binding of the guest molecules does not require major conformational changes in its molecule [170]. This can be achieved by designing a rigid host with a binding site having the appropriate properties for the particular guest molecules. Calix[4]arenes have been shown to accomplish the necessary preorganization requirements for obtaining stable host-guest complexes [170].

4.2 Structure and Synthesis Scheme of *Methoxy Calix[4]arene*

The first generation calixarene synthesized for the project described in this thesis was 5,11,17,23-tetrakis(3-propylthioacetate)-25,26,27,28-tetrakis-[(O-methoxycarbonyl)methoxy]calix[4]arene and is shown in Figure 4.3. This calixarene will be referred to as *methoxy calix[4]arene* within this thesis. The synthesis scheme of this compound is outlined in Figure 4.4 [171]. The upper rim of this calix[4]arene was functionalized with a thioacetate functional group, which enabled the molecules to bind to Au surfaces via S-Au bonds. STM imaging has shown that this modified calix[4]arene forms well-ordered SAMs on Au surfaces, as will be discussed later (see Chapter 5). The lower rim was modified with an *O*-methoxycarbonyl)methoxy-(-OCH_2COOCH_3) podand functional group, making the *methoxy calix[4]arene* receptive to selective ions.

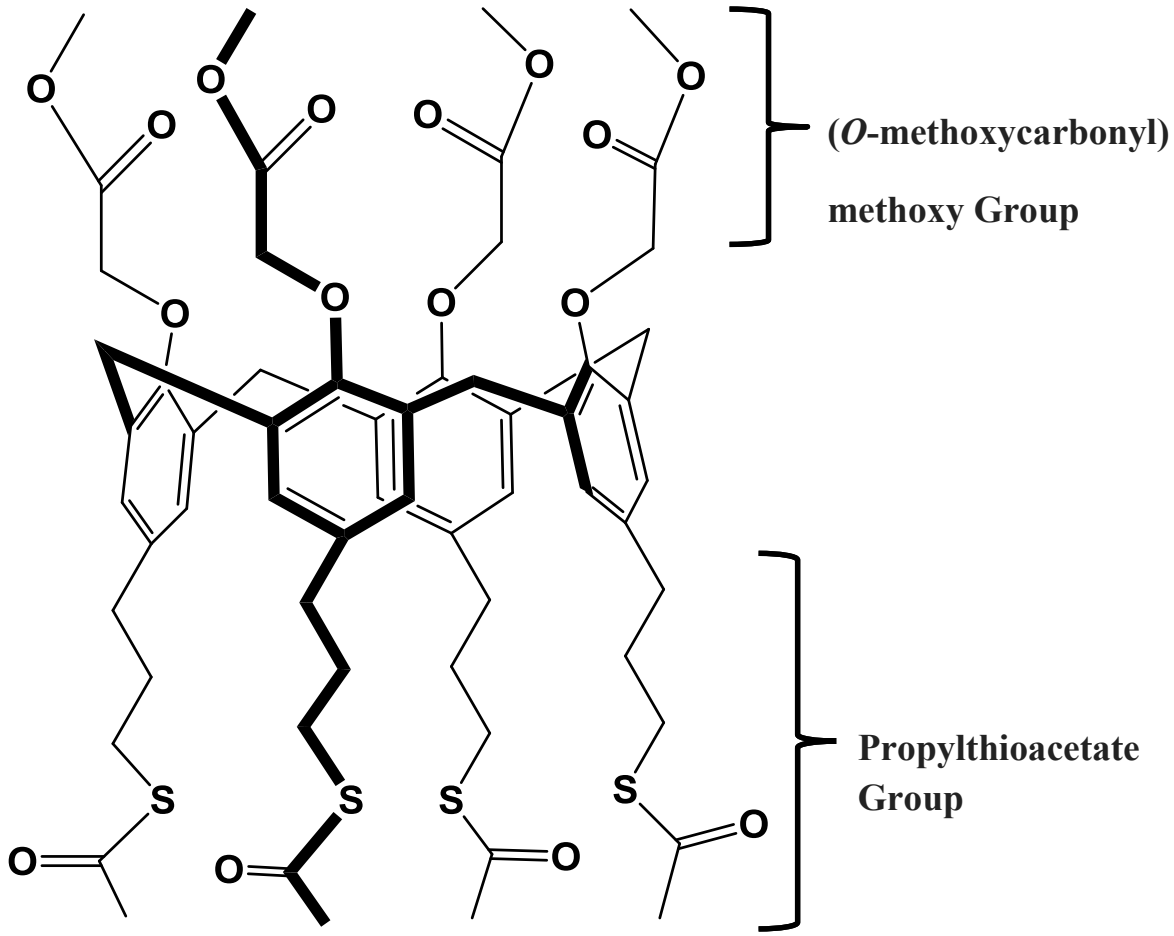

Figure 4.3: The structure of *methoxy calix[4]arene*.

The synthesis of this compound (conducted by the Georghiou's group in the Chemistry Department at Memorial University) was performed as follows. The de-*tert*-butylated calix[4]arene (denoted as **3** in the synthesis scheme shown in Figure 4.4) was first used as a starting material for the synthesis and was produced as shown from calix[4]arene **1**. Tetra-*O*-allylation of **3** formed **4** which was then converted into the tetra-*para*-functionalized intermediate **5**. Thioacetylation of the terminal alkene in **5** with AIBN

(azobisisobutyronitrile)-initiated reaction of thioacetic acid (CH_3COSH) in dioxane afforded **6**, which was finally converted to the desired tetrakis-[*O*-(methoxycarbonyl)methoxy]calix[4]-arene or *methoxy calix[4]arene,* **2**. A single-crystal X-ray analysis of the synthesized methoxy-calixarene **2** confirmed it to be in a *pinched-cone* conformation, as can be seen in Figure 4.5 [171].

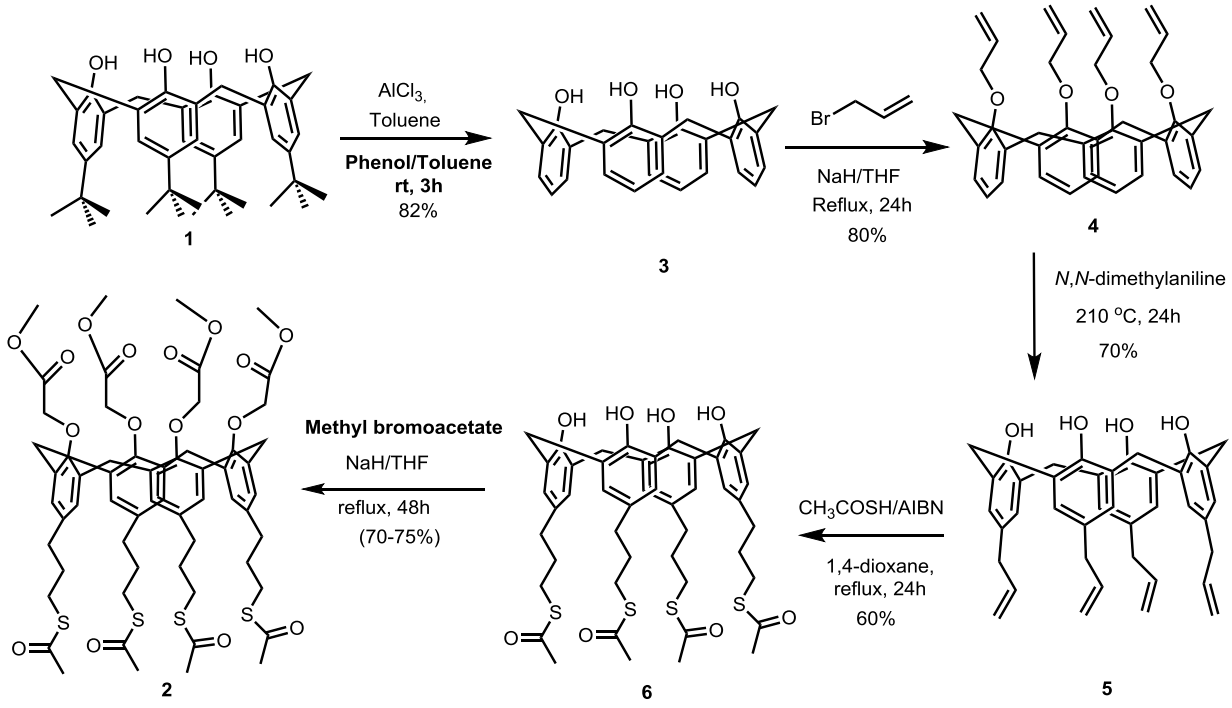

Figure 4.4: The synthesis procedure of *methoxy calix[4]arene (2)* [171].

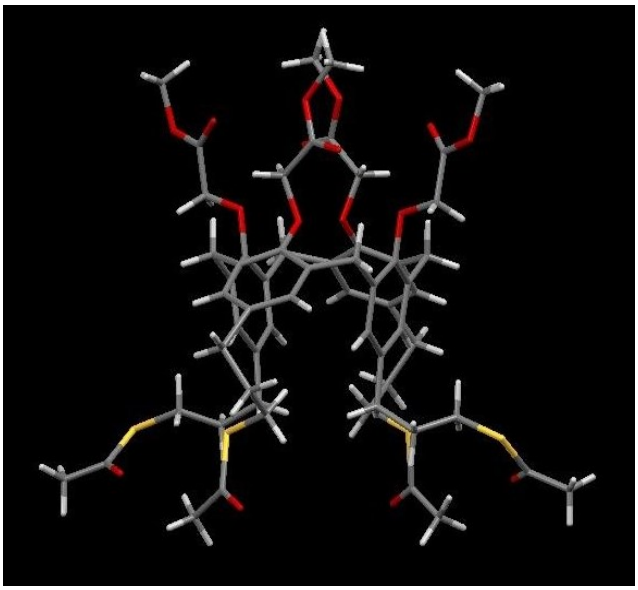

Figure 4.5: Single-crystal X-ray structure confirming the *pinched cone* confirmation of *methoxy calix[4]arene* [171].

4.3 Structure and Synthesis Scheme of *Ethoxy Calix[4]arene*

The second generation calixarene, 5,11,17,23-tetrakis(3-propylthioacetate)-25,26,27,28-tetrakis-[(*O*-methoxycarbonyl)ethoxy]calix[4]arene is shown in Figure 4.6. This compound differs from the first generation by the modification of the lower rim with ethoxy instead of methoxy groups. As illustrated by the synthesis scheme in Figure 4.7, the modification with ethoxy groups which follows the same synthesis scheme as in Figure 4.4 with the exception that the step from **6** to **7** which employed ethylbromoacetate, could in principle lead to better selectivity and/or enhanced sensitivity

towards ions of interest. There are many possible factors which have been speculated upon by other researchers to account for these subtle changes in selectivity [169].

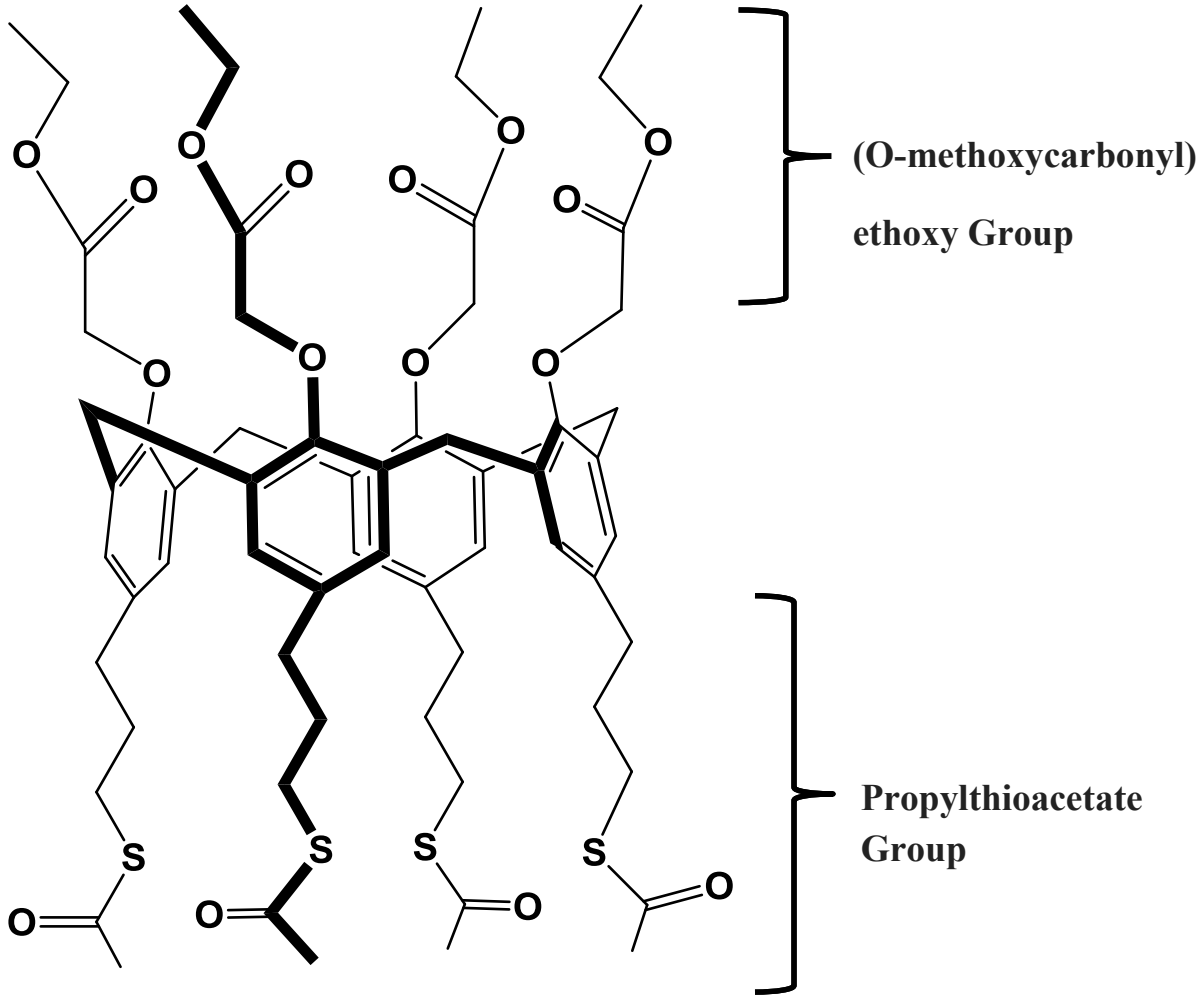

Figure 4.6: The structure of *ethoxy calix[4]arene*.

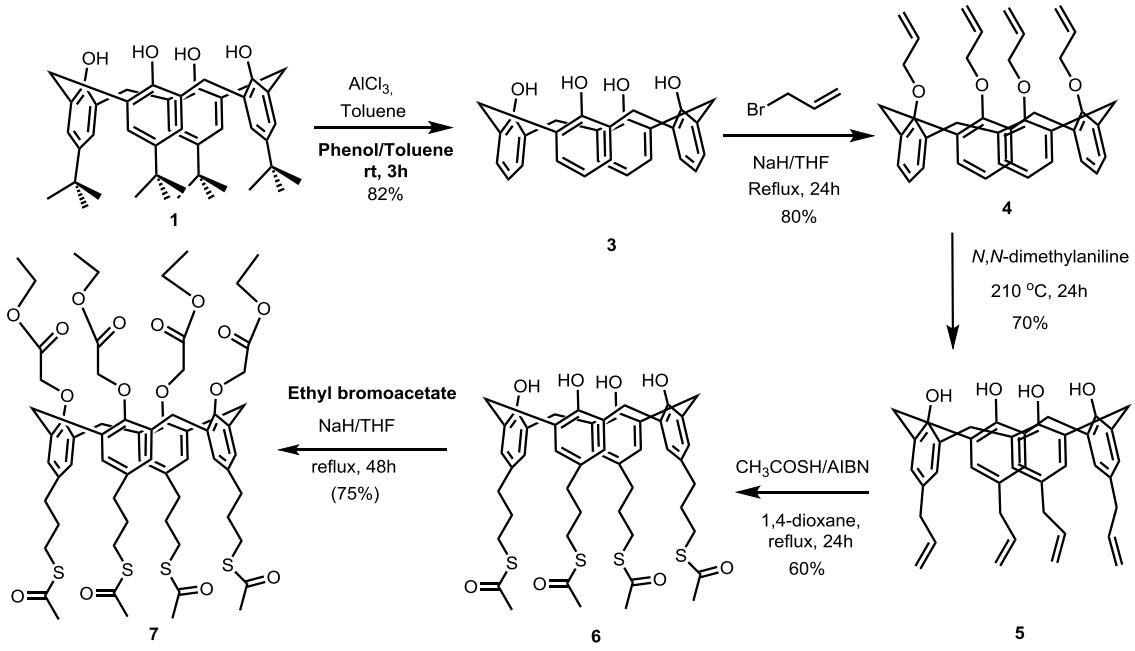

Figure 4.7: The synthesis scheme of *ethoxy calix[4]arene (7)*.

4.4 Structure and Synthesis Scheme of *Crown Calix[4]arene*

This third generation calix[4]arene shares the same synthetic methodology of the upper rim as with the previous generations whereby a thioacetate functional group was synthesized to anchor the molecules to gold. However the lower rim of this calixarene was modified with a crown ether-type of functional group, which forms a closed loop. The structure of the *cone-conformer bimodal crown calix[4]arene* is depicted in Figure 4.8. STM studies of this compound have revealed that this new calixarene was also capable of adhering to an Au surface, as will be shown in Chapter 5.

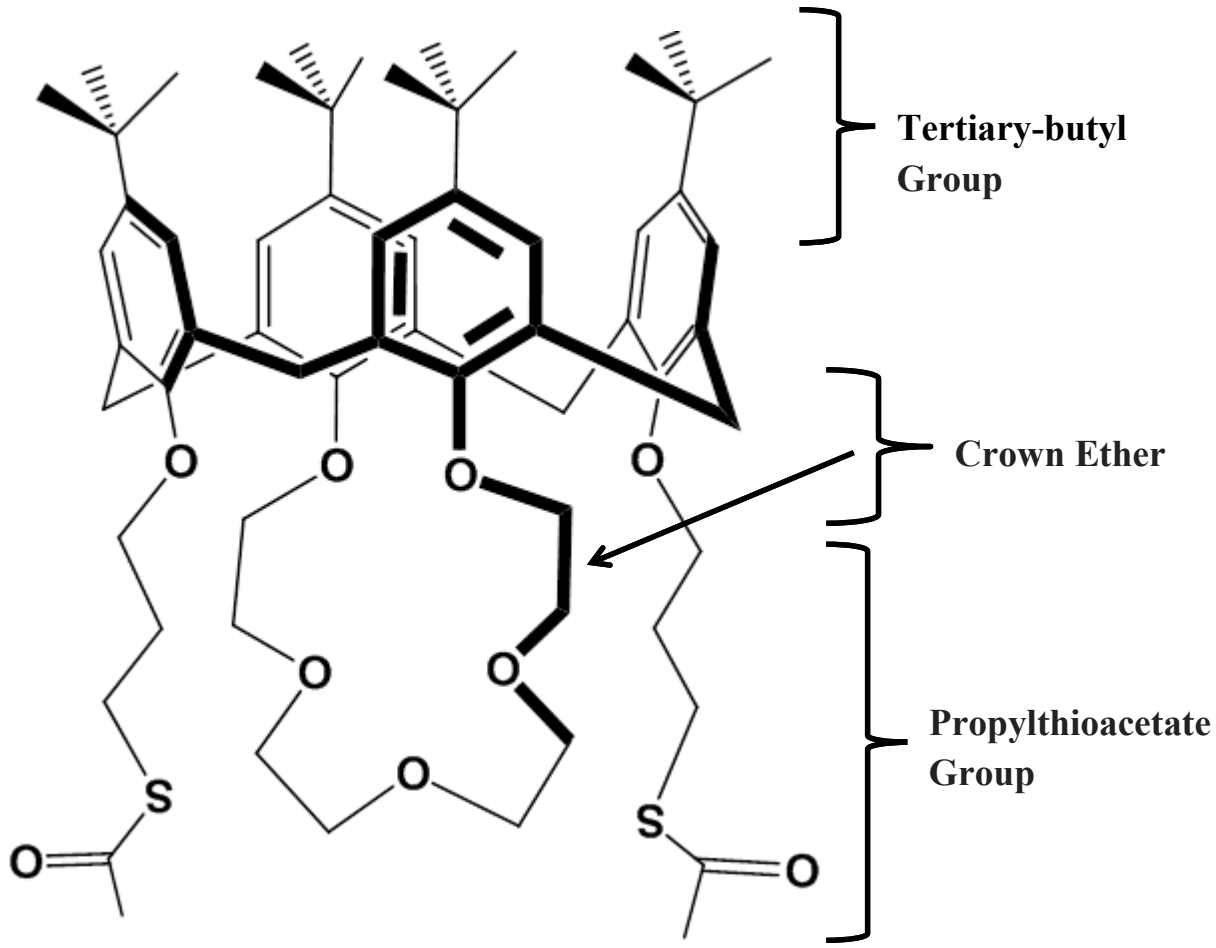

Figure 4.8: The structure of *crown calix[4]arene.*

The synthesis scheme of the *crown calix[4]arene* is illustrated in Figure 4.9. Firstly calix[4]arene **1** was used to produce 1,3-calix[4]-crown-5 (**9**). According to the published literature on similar reactions, the reaction of **9** with allyl bromide in the presence of Cs_2CO_3 in acetonitrile was anticipated to form compound **10** in a *1,3-alternate* conformation. The subsequent formation of the corresponding *1,3-alternate* conformer **8** from **10** was expected. However, the *cone* conformer of **8** was instead obtained, as

determined by NMR spectroscopy. Single-crystal X-ray crystallography, also confirmed that the newly synthesized crown calix[4]arene was in the *cone* conformation as shown in Figure 4.10 [172].

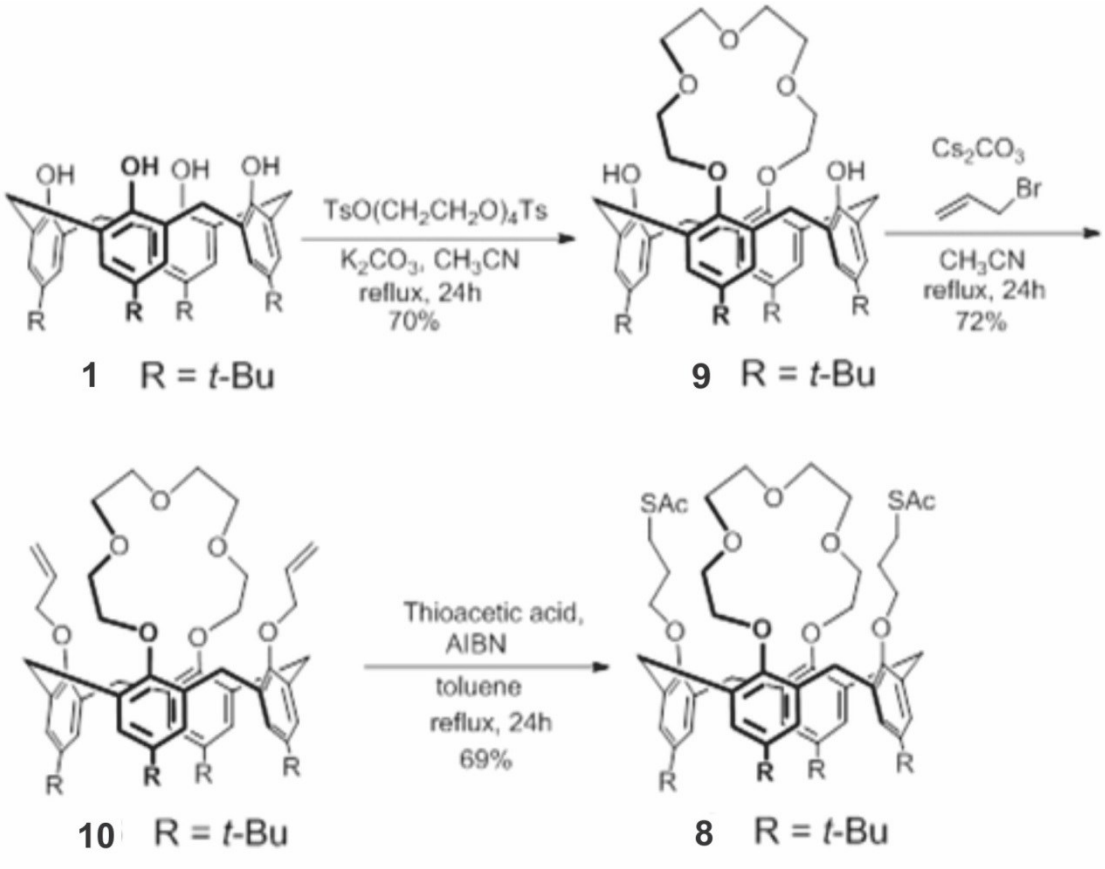

Figure 4.9: The synthesis scheme of *crown calix[4]arene (8)* [172].

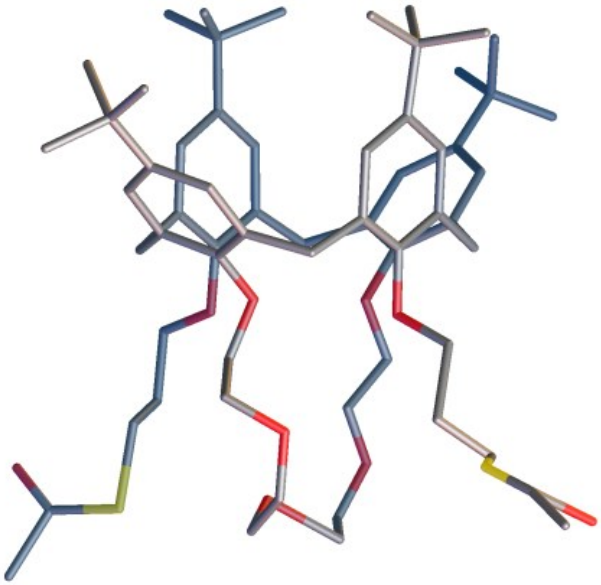

Figure 4.10: Single-crystal X-ray structure of crown *calix[4]arene*, showing the *cone* conformation [172].

4.5 Mechanism for Thioacetate Binding to Au Surfaces

The mechanism by which a thioacetate (or thiol) anchor to the gold surfaces has been a subject of ongoing investigation [173,174]. In a recent work, Fischer *et al.* [175] proposed two possible mechanisms to explain how a thioacetic acid (TAAH) binds to a Au (111) surface. In the first mechanism, demonstrated in Figure 4.11a, it was proposed that TAAH chemisorbs on the Au(111) surface allowing a H-S hemolytic cleavage bond to form. This formation of the cleavage bond leads to the binding of the chemisorbed TAA radical to the Au (111) surface through the S atoms. Figure 4.11b illustrates the second possible mechanism which begins with the physisorption of the TAAH to the Au

(111) surface. In this mechanism the H atom does a 1,2 shift to the carbonyl carbon atom, generating a transient quasi-tetrahedrical intermediate that leads to the final products. The authors concluded that the "acetyl" ($CH_3C=O$) portion of the thioacetic acid (TAAH) is cleaved off upon interaction with the Au surface and the result being that the sulfur binds directly to the gold.

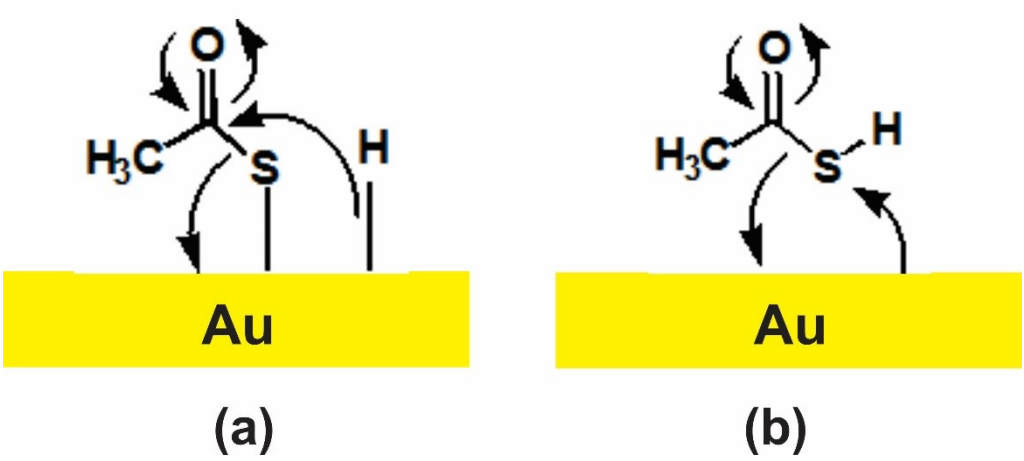

Figure 4.11: Schematic showing two possible mechanisms (a and b) proposed to explain the S adlayer formation on the gold surface. [Adapted with permission from Reference 175].

In the case of calix[4]arene which is modified with a thioacetate to bind with the gold surface, the possible binding mechanism to gold is shown in Figure 4.12. It is conceivable for thioacetate that a similar phenomenon occurs with the difference being that the sulfur atoms on the calix[4]arene are attached to the carbon atoms of the three-carbon groups ($-CH_2CH_2CH_2-$) which are attached to the wide-rim of the calix[4]arene.

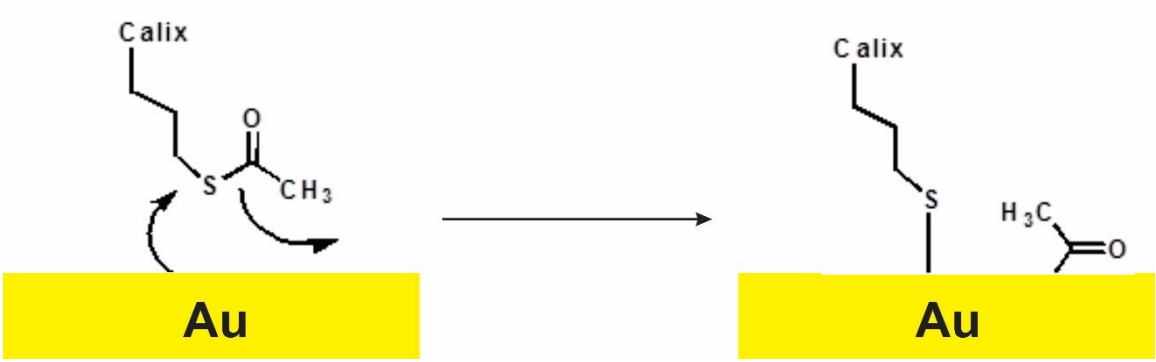

Figure 4.12: Possible mechanism explaining how thioacetate anchor to the gold surface.

4.6 Experimental Procedures

4.6.1 Microcantilever Surface Preparation

This work described herein was conducted using four different types of microcantilevers, as displayed in Table 1. The first and second types (CSC12 and CSC 38 from MikroMasch, Estonia) contained three microcantilevers on the chip (see Figure 4.13) but as they were used in the single microcantilever experimental setup, only one microcantilever was used. The third and fourth types (CLA500-010-08 and CLA750-010-08 from Concentris, Basel) were microcantilever arrays, comprising 8 microcantilevers on the chip. These two types were used in the newly developed experimental setup.

Table 4.1: The dimensions of the four types of microcantilever sensors used during this work, as provided by the manufacturers.

Microcantilever Type	Length (µm)	Width(µm)	Nominal Thickness(µm)	Typical Spring constant (N/m)
CSC 12	350 ± 5	35 ± 3	1 ± 0.5	0.03
CSC 38	350 ± 5	32.5 ± 3	1 ± 0.5	0.03
Cantilever Array (CLA500-010-08)	500 ± 3	100	1± 0.1	0.030 ± 0.008
Cantilever Array (CLA750-010-08)	750± 3	100	1± 0.1	0.010 ± 0.003

As illustrated in Figure 4.13, the microcantilever chip we used contained three microcantilevers of different lengths. Since the single-microcantilever experimental setup was designed to allow monitoring the response of only two separate microcantilevers, only one microcantilever within the chip was used. Microcantilever B which is the longest one was always used due its highest sensitivity over other microcantilevers on the chip (e.g.: A and C). All types of microcantilevers presented in table 4.1 were fabricated from single crystal Si where the microcantilever surface is in the {100} plane and edges are aligned along the <110> direction.

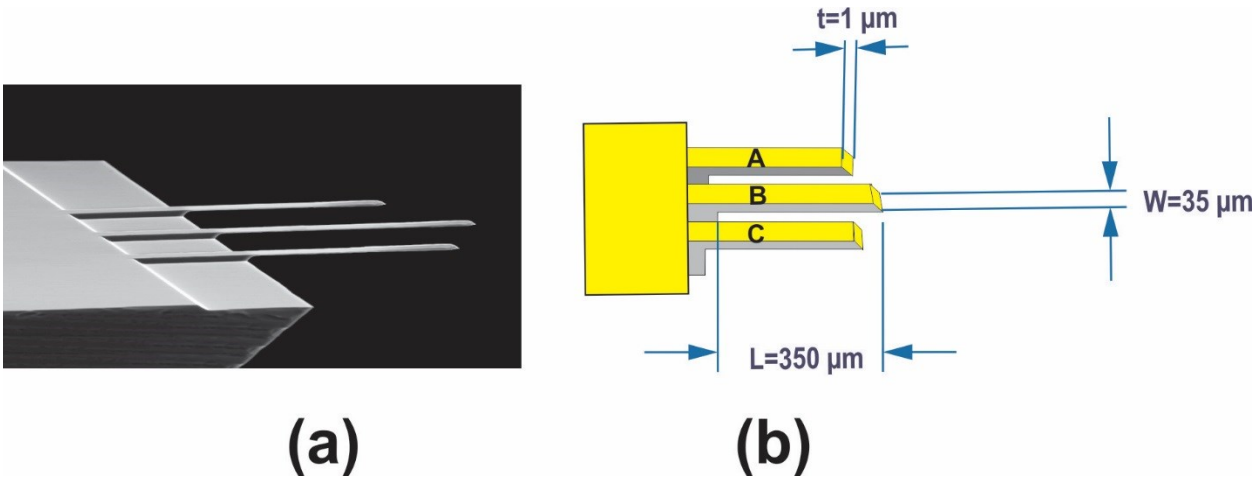

Figure 4.13: (a) An SEM image of a MiKroMasch cantilever (CSC 38) [Reprinted with permission from MikroMasch]. (b) Schematic representation showing the dimensions of CSC 12 MiKroMasch microcantilevers. CSC 38 microcantilevers have similar design, length and thickness but different width (e.g.: 32.5 µm). In both types, the longest microcantilever (B) was used due to its higher sensitivity.

In order to use microcantilevers in sensing experiments, the following three main steps were followed: cleaning the cantilevers, thin film deposition and SAM preparation. All microcantilever types shown in table 4.1 were subjected to the same cleaning and thin film deposition process. However the chemical functionalization of the microcantilever arrays required the use of a functionalization unit which facilitates the simultaneous incubation with different sensing layers (see Chapter 6). The chemical activation of single microcantilevers (CSC 12 and CSC 38) was performed by immersing them in a solution containing the sensing layer molecules.

As stated previously, the microcantilever reliability and effectiveness can be affected by the cleaning methodology and thus the effect of cleaning method was first examined. The first method investigated was cleaning the microcantilevers with a Piranha solution (H_2SO_4: H_2O_2 =3:1) for 10 minutes and then washing them twice with ethanol followed by de-ionized water to remove any residue and contamination on the surface. After rinsing, the microcantilevers were dried in an oven for 10 minutes at 275 C.

The second method was to treat the microcantilevers with the RCA cleaning method [176]. In this method, cleaning was performed in three steps as follow:

1- A solution of (NH_4OH: H_2O_2: H_2O = 1:1:5) heated at 80 ° C for 10 minutes. This step removes the organic residues off the Si-microcantilever surface.
2- A solution of (HF: H_2O=1:50) at room temperature for 5 minutes. This step ensures the removal of the oxide layer on the Si-microcantilever surface.
3- A solution of (HCl: H_2O_2: H_2O = 1:1:6) at 80 ° C for 10 minutes. This step aims at removing the ionic contaminations off the Si-microcantilever surface.

Following the cleaning process, the microcantilevers were coated with 5 nm of Inconel followed by 40 nm of gold. The use of this particular thickness of gold was based on attempts made to optimize the gold thickness that can enhance the microcantilever sensitivity (see chapter 5).

The effect of the cleaning methodology was investigated by exposing two calixarene-functionalized microcantilevers, one cleaned using a Piranha solution and the another using the RCA method to a 10^{-6} M solution of $Ca(ClO_4)_2$. As can be seen in Figure 4.14, the microcantilever cleaned with the RCA method gave a larger deflection than the microcantilever cleaned using the Piranha method. A possible reason for such a difference is that using the RCA method removes all possible contaminations that can be present on the microcantilever surface however the Piranha method only ensures the removal of the ionic residues. Because of the effectiveness of the RCA method in increasing the microcantilever sensitivity, it was used in all experiments to prepare the microcantilevers.

Flow rate of analyte solutions was also tested before conducting sensing experiments. Optimal flow rate ensures that analyte solutions are introduced to the fluid cell so that the analyte molecules interact with the microcantilever surface without disturbing the microcantilever stability. Rapid flow rates were found to cause fluctuations in the microcantilever response seen by noise in the output signal. A slow flow rate of 0.1 ml/min was found to cause no major effect on the microcantilever stability and thus it was adopted during the course of all experiments conducted in this work.

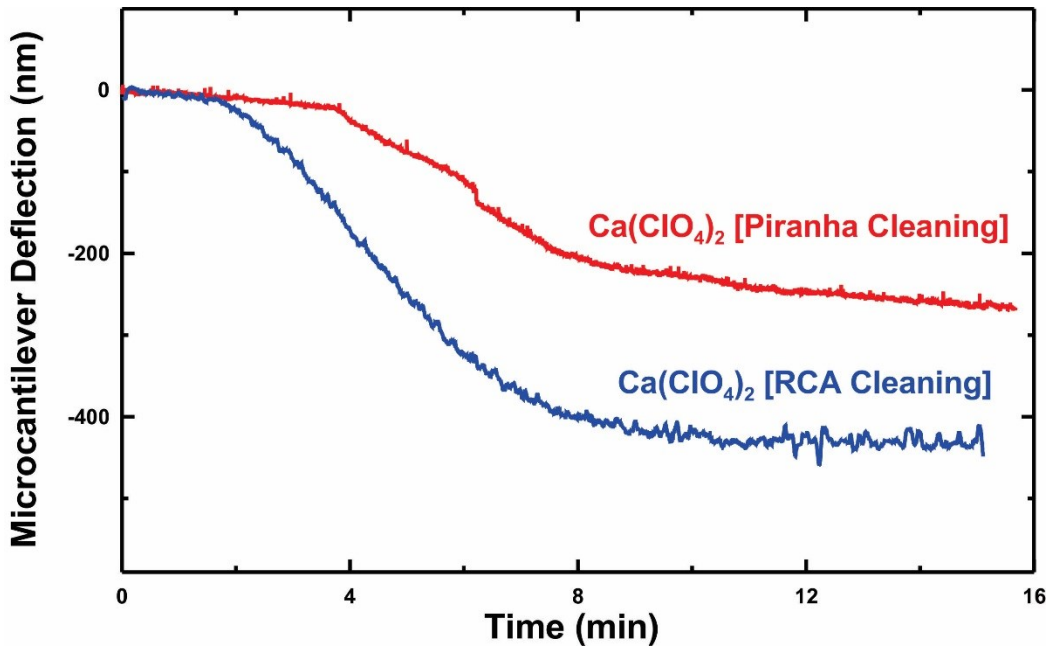

Figure 4.14: The microcantilever deflection as a function of time in response to the injection of a 10^{-6} M solution of $Ca(ClO_4)_2$. The sensitivity of calixarene-modified microcantilever treated with RCA method (blue curve) was higher than that cleaned with Piranha method (red curve).

4.5.2 Preparation of Reference Microcantilever

It is of great importance to include a reference microcantilever in all sensing experiments since the microcantilever may participate in interactions other than those between the target and the functional layer. In particular the reference microcantilever is used to exclude thermal and environmental effects such as temperature variations and non-specific binding that may affect the signal of the active microcantilever. The reference microcantilever must be prepared in a similar manner as the active microcantilever. In this work, reference microcantilevers were cleaned using the same cleaning method as

the active microcantilever and coated with inconel and gold in the same deposition batch with the active microcantilever meaning that they have the same thickness and morphology as the active ones. In contrast to the active microcantilevers which were functionalized with a sensing layer (e.g. calixarene molecules), reference microcantilevers were coated with decanethiols that do not interact with the target molecules. The signal of the reference microcantilever is then subtracted from the signal of the active microcantilever to give a differential signal that results in a microcantilever deflection that is caused only by the interaction between the calixarene and the target ion molecules. Figure 4.15 shows an example of a differential signal of the microcantilever where it is clear that the differential signal which represents the pure microcantilever deflection has less value than the active one. This signifies that the active microcantilever experienced a deflection that resulted from nonspecific bindings.

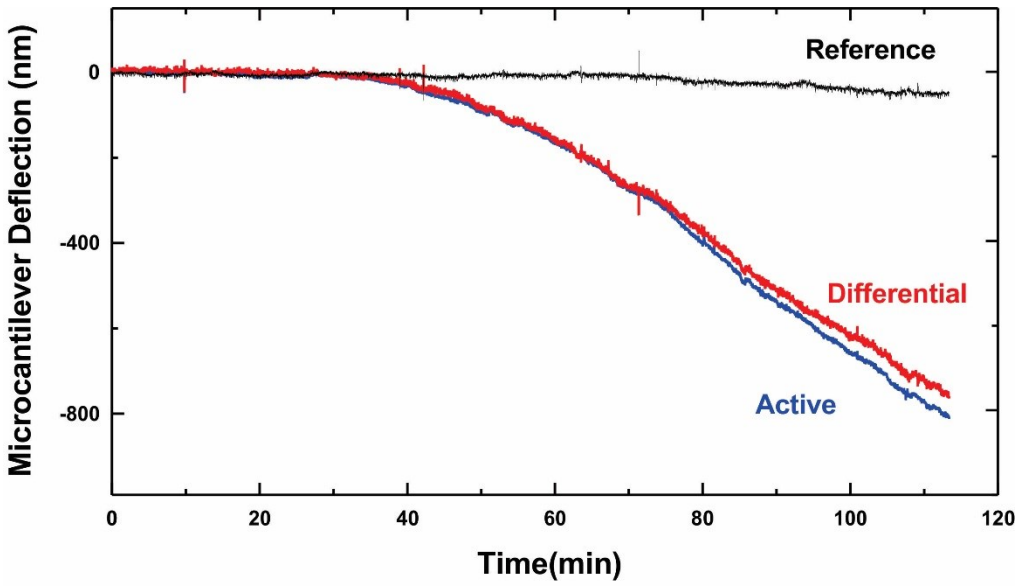

Figure 4.15: Active, reference, and differential signal of a microcantilever sensor.

Chapter 5 Characterization and Sensing Measurements of Calix[4]arene Functionalized-Microcantilevers*

This chapter is mainly concerned with examining the sensitivity and selectivity of calix[4]arene-functionalized microcantilevers sensors towards specific target ions. This chapter will first show STM characterizations that were performed in order to ensure that calix[4]arene molecules formed well-defined SAMs on the Au-coated microcantilever surface. Prior to sensing experiments, it was necessary to optimize the experimental conditions to maximize the sensitivity of calix[4]arene-functionalized microcantilevers. Therefore, the effect of incubation time as well as the thickness of the gold film on the overall response and sensitivity of calix[4]arene-functionalized microcantilevers was investigated. Target ion detection experiments were conducted and the results are discussed in sections 5.4 to 5.8. Although this work involved the use of two sensing experimental platforms, this chapter only presents the experimental results and discussion associated with the single microcantilever experimental setup. Experimental results obtained from the new 16-microcantilever experimental system will be provided in Chapter 7.

* Parts of this chapter have previously been reported in publications which have resulted from this author's work and are cited as [165], [171] and [172], and includes excerpts from Reference [165].

5.1 Calix[4]arene Immobilization and Characterization

5.1.1 Characterization of Methoxy Calix[4]arene

In this work, the immobilization of calix[4]arenes onto gold coated microcantilevers was accomplished through the well-known but poorly understood Au-S bonding [174]. The initial plan was to modify the calixarene with a thiol (S-H) group to bind to a gold surface. However, such modification was not possible. Instead, the modification with thioacetate groups on our calixarenes has been found to bind effectively to the Au and thus was employed. The SAM of methoxy calix[4]arene (see Figure 5.1) molecules was characterized using STM.

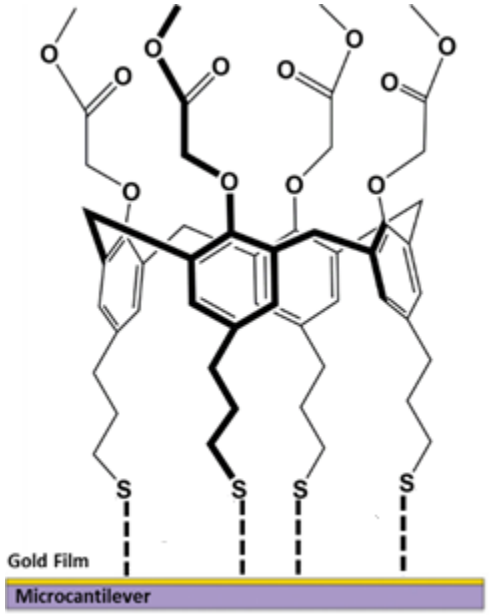

Figure 5.1: A schematic representation of methoxy calix[4]arene on a Au-coated microcantilever. (Not to scale).

Figure 5.2 shows an STM image of the methoxy calix[4]arene immobilized on Au-coated mica. The STM image indicates the presence of a long range, highly ordered SAM of calix[4]arene molecules. The STM image on the left was magnified in order to clearly distinguish the calix[4]arene molecules. To further highlight the periodicity of the SAM, the STM image was processed using the software Scanning Probe Image Processor (SPIP). This image is characterized as having rows of bright spots which are attributed to single calix[4]arene molecules. The molecules on the surface are arranged in an oblique unit cell configuration 2.0×1.3 nm in size with an angular divergence of 115º. These values are consistent with those obtained by Pan *et al.* [177] with the difference attributed to the different linkers used to attach the calix[4]arene molecules to the Au surface.

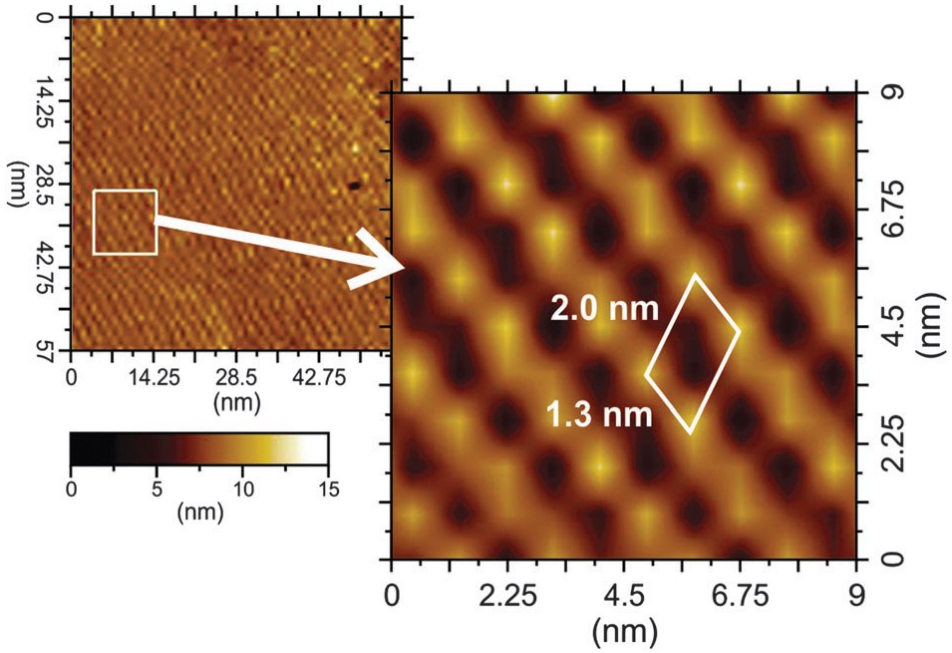

Figure 5.2: STM image of methoxy calix[4]arene molecules on gold. The top left image represents an area of 57 × 57 nm. Below is a scale bar showing the magnitude of the vertical height from low (black) to high (white). The image on the lower right-hand side is a magnified portion of the STM image on the upper left taken from the area indicated by the white square 9 × 9 nm in size. Each bright spot corresponds to a single methoxy calix[4]arene molecule [171].

5.1.2 Characterization of crown calix[4]arene

In order to assure that the crown calix[4]arene molecules (see Figure 5.3) were forming a SAM on the Au-coated microcantilever surface, STM imaging was again performed.

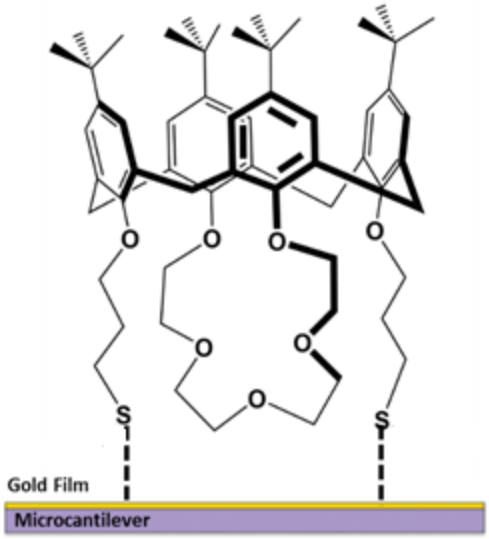

Figure 5.3: The formation of the self-assembled monolayer of crown calix[4]arene on the Au-coated microcantilever surface. (Not to scale).

Figure 5.4a shows a 26 × 26 nm sized image of crown calix[4]arene molecules on gold. As can be seen the image indicates the presences of a highly ordered SAM of calixarene molecules. A 9.5 × 10.5 nm section of this figure was isolated and expanded as shown in Figure 5.4b. In order to help highlight the molecular ordering, the image was processed using the software Scanning Probe Image Processor (SPIP). This image more clearly reveals the high ordering of calixarene molecules on the microcantilever surface, indicating that the sensing layer is well-established on our microcantilevers which should be very stable due to the strong bonding between the sulphur and gold substrate. With each high spot in the image indicating a single calixarene molecule, the intermolecular distances have been measured to be 1.9 nm and 1.8 nm in the directions shown in the

figure. These values are consistent with similar observations made on other types of calixarene-based SAMs [177].

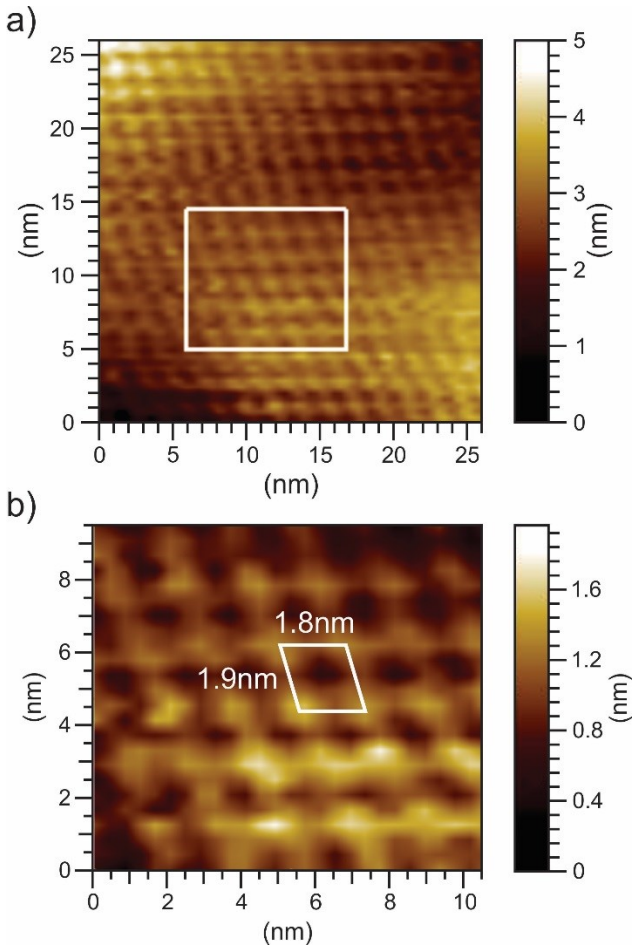

Figure 5.4: STM images of calix[4]arene-crown compound which forms a self-assembled monolayer on the gold surface. (a) A 26 × 26 nm sized image of crown calix[4]arene molecules on gold. (b) A magnified portion of the STM image shown in (a) where each high spot indicates a single crown calix[4]arene molecule [172].

5.2 Effect of incubation time on the sensitivity of methoxy calix[4]arene-functionalized microcantilever

The incubation or immersion time is defined as the period of time during which the solid substrate (e.g.: microcantilever) are exposed to the reference or receptive molecules (e.g.: calix[4]arene). Despite the fact that the incubation time is a key stage during the preparation of SAM-modified microcantilevers, very little consideration has been given by the microcantilever sensor community [178]. In this work, the effectiveness of a self-assembled monolayer of calixarene molecules on the microcantilever surface has been investigated by varying the incubation time in the hopes of increasing the microcantilever sensor sensitivity.

Au-coated microcantilevers were functionalized with a 10^{-6} M solution of methoxy calix[4]arene and incubated for six different times: 1h, 3h, 6h, 12h, 24h and 1 week. The microcantilevers were then placed in the fluid cell and exposed to a 10^{-6} M aqueous solution of $CaCl_2$. Figure 5.5 shows the deflections of microcantilevers incubated at different times in response to the introduction of $CaCl_2$ solution. The data shows that a one hour incubation led to the largest microcantilever deflection, whereas microcantilevers incubated over longer periods had smaller deflections when subjected to the same Ca^{2+} concentrations. It was also interesting to find that an incubation time longer than one day gave no change on the status of the microcantilever deflection.

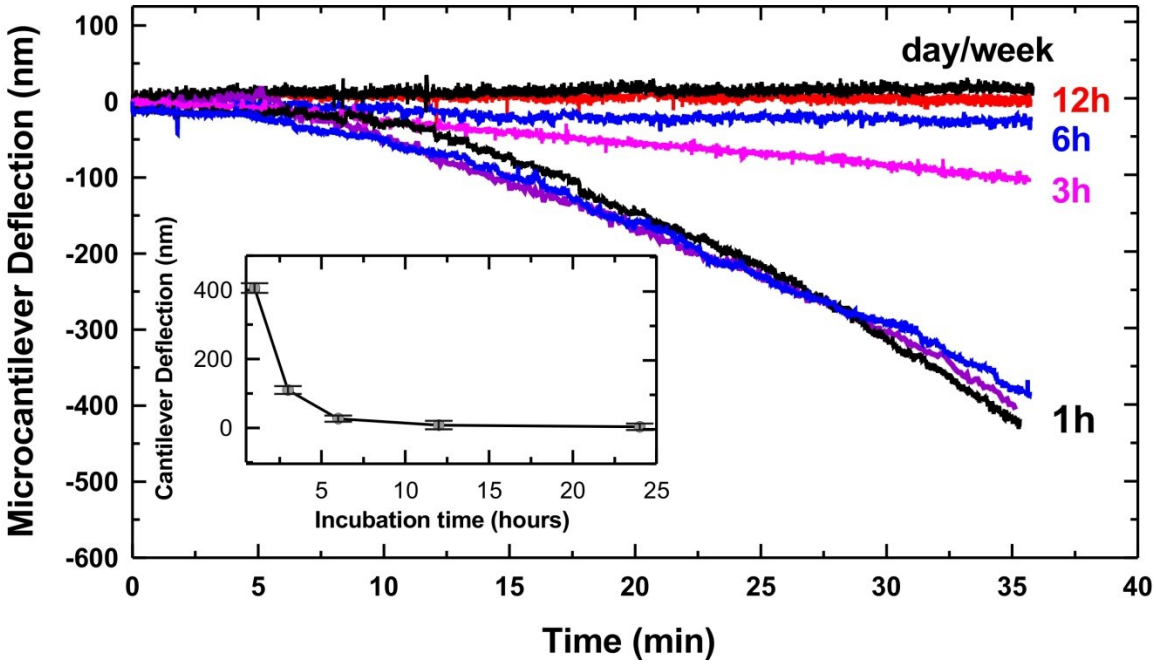

Figure 5.5: The effect of the incubation time on the microcantilever deflection for sensors exposed to 10^{-6} M aqueous solutions of $CaCl_2$. The three curves for the 1 h incubation time show the reproducibility of the collected data. The inset shows the microcantilever deflection of each curve at 35 min along with their uncertainty values represented by the error bars [165].

As shown in Figure 5.5, a one week incubation resulted in a microcantilever deflection similar to that observed with a one day incubation. It is speculated that the SAM of the calixarene molecules forms on the microcantilever within the first hour during the incubation processes. The STM analysis of the formation of the SAM of these calix[4]arene molecules illustrated in Figure 5.2 showed complete well-ordered monolayers with no bare areas after a 1 h incubation period. As the incubation continues, we speculate that additional calixarene molecules begin to physisorb onto the initial SAM

blocking their receptors to the target molecules thereby causing the sensor to become less sensitive as also suggested by others [179]. We further speculate that as more calixarene molecules adsorb onto the microcantilever, the sensor sensitivity to Ca^{2+} ions continues to decrease, until after a 24 h incubation period, the initial SAM is presumably fully covered thereby preventing further Ca^{2+} from binding onto the calixarene-coated microcantilever. This, in turn, could explain why the observed results for the 1 week incubation period were found to be the same as those obtained using microcantilevers incubated for 24 h since once the initial SAM is fully covered, further adsorption of additional calixarene molecules onto the surface of the microcantilever would not change the microcantilever sensitivity.

Figure 5.5 also shows the reproducibility that has consistently been obtained with our microcantilever sensor setup as seen by the three experiments conducted with microcantilevers incubated for 1 h. As can be seen, the three curves very closely follow the same profile. The inset graph in Figure 5.5 shows the microcantilever deflection of each curve at 35 min along with their associated uncertainty values. The uncertainty values (i.e. standard deviation), represented by error bars in the inset graph, were calculated by taking the average of the absolute value of the difference between each microcantilever deflection curve and the average value of all the curves collected which in most case was three.

5.3 Effect of Gold Film on the Sensitivity of calix[4]arene-functionalized microcantilever

The use of a thin gold film deposited on one side of the microcantilever as a means of attaching the receptive layer has been a key part of the microcantilever sensor design since the very beginning of this technology. Depositing a thin gold film on one side creates a way to selectively bind the receptive layer on one side of the microcantilever. The fact that gold is highly stable and is not easily prone to oxidizing means that the receptive layer immobilized on the microcantilever can have a longer shelf-life than similar silicon-based receptive layers.

As stated previously, gold can induce a surface stress that can reduce or prevent subsequent surface stress from forming on the microcantilever surface during molecular adsorptions. Therefore it was important to investigate the effects of thickness and roughness to optimize the microcantilever sensitivity. In an effort to understand such properties, studies were conducted to identify a relationship between the roughness of the gold thin film and the microcantilever sensitivity. Some computational and experimental investigations argued that rougher thin gold films produced higher microcantilever sensitivity over smoother surfaces [50,51,180]. On the other hand, other reports have suggested the opposite where a smoother gold thin film surface resulted in an increase to the microcantilever sensitivity than rougher surfaces [48,49,181]. In contrast to the aforementioned findings where the microcantilever sensitivity was observed to have been greatly dependent on the surface roughness, Desikan *et al.* [182] found a very negligible

effect of the surface roughness on the microcantilever sensitivity. Such wide inconsistency in the literature may be attributed to the fact that different reaction mechanisms (e.g.: DNA, alkanethiol) were used to investigate the microcantilever sensitivity which may have different response to the state of the gold surface [180]. It is obvious from the aforementioned inconsistent literature results that a conclusive relationship between the gold morphology and the microcantilever sensitivity has not been established yet. Understanding the effect of the gold morphology on the microcantilever sensitivity requires investigating a number of sputtering parameters that play a major role in determining such influence. In a recent work, Ayoub *et al.* [183] investigated the effect of various sputtering parameters such as deposition rate, power, distance between target and substrate, substrate bias and substrate orientation on the morphology of thin Au films deposited on silicon substrates. However the effect of these parameters on the microcantilever sensitivity has not been studied yet and should be considered in future studies of microcantilever sensors.

Another crucial property of the gold film that needs to be investigated is the gold thickness. In this work, we attempt to investigate the role of gold thickness on the microcantilever sensitivity. Before such attempts were made, initial studies were first focused on investigating the influence of the deposition rate on the initial deflection state of the microcantilever. We have found that a deposition rate of 0.2 Å/sec and a sputtering power of 10W produced a gold thin film with low residual surface stress during sputtering. Such stress is believed to form onto silicon microcantilevers during sputtering because of the formation of grain boundaries formed from the coalescence of nucleated

clusters [50]. Despite being a microscopic quantity, the effect of such stress could be visualized on the microcantilever sensor using an optical microscope. Figure 5.6 shows the microcantilever state after depositing gold with different thicknesses and different deposition rates.

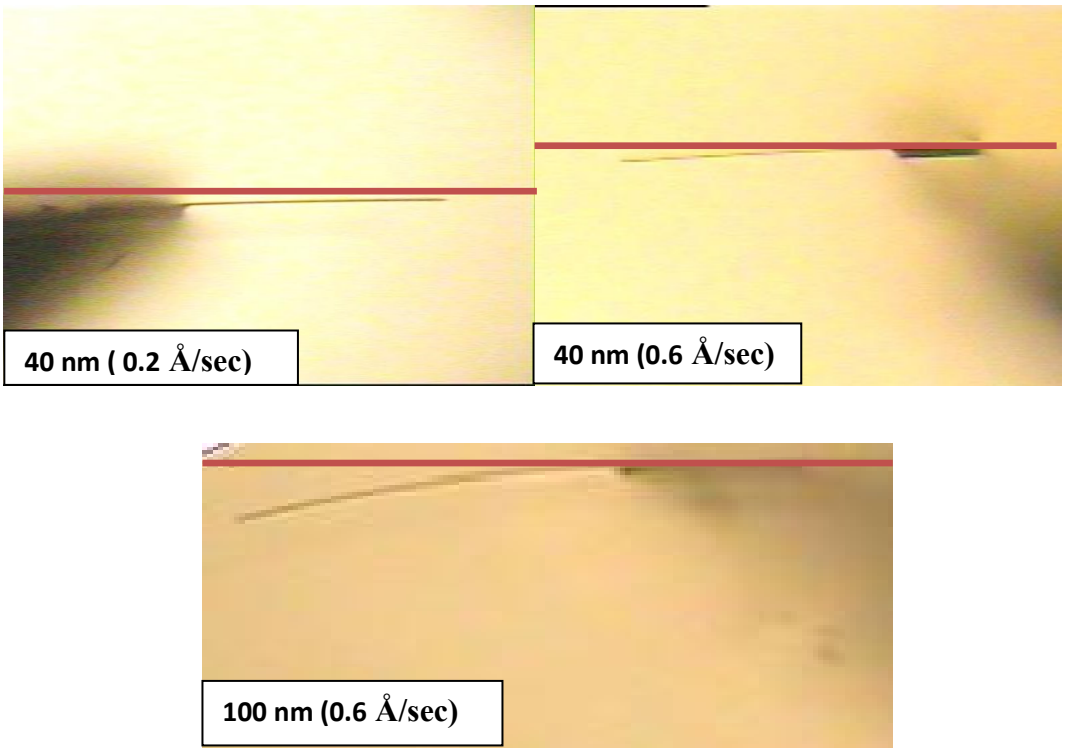

Figure 5.6: Optical microscope images of microcantilever sensors after depositing a) 40 nm [0.2 A/s deposition rate] b) 40 nm [0.6 A/s deposition rate] and c) 100 nm of gold thin film [0.6 A/s deposition rate] (Red lines represent reference line for ease of recognizing the deflection).

The deposition of 40 nm gold thin film on the microcantilever surface at two different deposition rates led to the formation of low residual surface stress that would not cause a

large influence on the subsequent molecular adsorption. However depositing 100 nm of gold resulted in a large microcantilever deflection due to the formation of large residual surface stress which reduced the microcantilever sensitivity in molecular adsorption experiments. However such great pre-deflection was highly decreased when the deposition rate was decreased to 0.2 Å/sec. It was found that increasing the sputtering power led to an increase in the initial deflection of the microcantilever (see Figure 5.6). Even though high sputtering power decreases the sputtering time, it may be possible that the fast deposition leads to the rapid formation of stress on the microcantilever during sputtering.

STM imaging was also used to characterize the topography of the gold film on the microcantilever surfaces. Figure 5.7 shows STM images of 20, 40, 60 and 100 nm thick gold films deposited at a deposition rate of 0.2 Å/sec. For 20 nm thick gold, the root mean square (RMS) roughness was found to be 0.92 nm and images revealed grain boundaries that are clearly defined. Increasing the thickness to 40 nm increased the RMS roughness value to 1.4 nm where coalescence can be clearly distinguished. Surfaces coated with 60 nm of gold showed a combination of well-defined grain boundaries and regions in the coalescence stage. At 60 nm, the RMS roughness value also increased to 1.65 nm. Deposition of 100 nm thick gold film showed larger grains with clear boundaries and less coalescence. The RMS roughness value was 1.83 nm which is the largest value among the Au thicknesses investigated. It is inferred from the aforementioned analysis that the RMS value and the grain size (summarized in Table 5.1) are functions of the gold thickness where increasing the gold thickness increased the

RMS roughness and the grain size. It is also realized that there is a relationship between the roughness of the Au surface and the size of the grains where increasing the roughness of the gold surfaces increased the grain sizes.

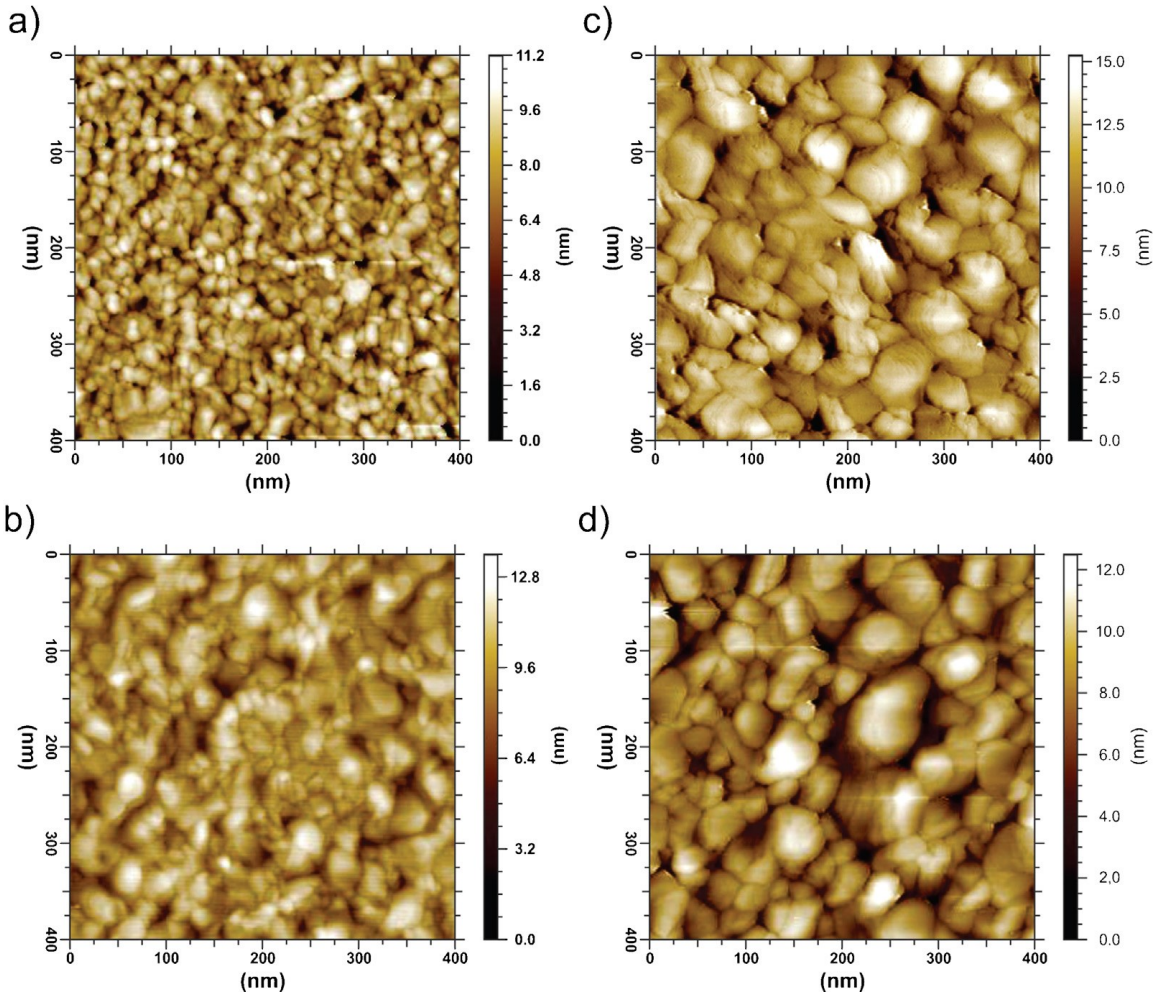

Figure 5.7: Scanning tunneling microscopy (STM) images of gold thin film deposited at 0.2 Å/sec on silicon substrates for different thicknesses: a) 20 nm, b) 40 nm, c) 60 nm, d) 100 nm [165].

Table 5.1: RMS values and grains size of gold layers of different thicknesses.

Au-Thickness (nm)	RMS Roughness (nm)	Average Grain Size (nm)
20	0.92	17.5
40	1.4	19.2
60	1.65	22.6
100	1.83	36.8

In order to relate the role of the gold thickness to the sensitivity of the microcantilever sensor, microcantilevers coated with Au of different thicknesses were functionalized with a SAM of methoxy calix[4]arene and were introduced to a 10^{-6} M solution of $CaCl_2$. In these experiments, all parameters (e.g.: stabilization solution, calixarene concentration, and target concentration) were kept constant except for the Au thickness. Microcantilevers coated with 20, 40, 60, 80 and 100 nm gold thin films were tested three times each. Each microcantilever was incubated in a 1.0 µM solution of methoxy calix[4]arene for 1 h. The microcantilevers were then exposed to an aqueous 1.0 µM $CaCl_2$ solution. Figure 5.8 demonstrates the microcantilever response to the injection of $CaCl_2$ solution where it is obvious that a microcantilever coated with 40 nm of gold

experienced the largest deflection over other microcantilevers coated with different gold thicknesses. The insert graph shows the relationship between the microcantilever deflection and the Au thickness at 35 min where it is clear that the microcantilever deflection is not a simple function with respect to the film thickness or the RMS roughness. As the film increases in thickness from 20 to 40 nm, the microcantilever becomes more sensitive, followed by a decrease in sensitivity between 40 and 60 nm at which point the trend reverses and the microcantilever becomes more sensitive although less so than for the 40 nm thick Au film. Referring to our previous discussion on the formation of the residual surface stress during the Au deposition, the microcantilever deflection obtained with a 100 nm Au film was contrary to one's expectations. This is because it was observed (see Figure 5.6) that depositing 100 nm of Au produces a larger pre-deflection (although it was found to be lower with 0.2 Å/sec deposition rate) which we hypothesize should affect the microcantilever deflection produced during subsequent molecular adsorptions. Conversely, the microcantilever deflection obtained with 20 nm Au thickness was low despite the fact that the deposition of 20 nm Au did not produce a significant pre-deflection. In the case of 80 nm thick Au, where the pre-deflection was found to be larger than that generated with 20 nm thick Au, the experimental results supported the argument that a large pre-deflection causes small deflection during molecular interactions. These results cannot be solely related to the roughness of the gold film since the largest deflection was observed with 40 nm Au film whose RMS value was neither the smallest nor the largest.

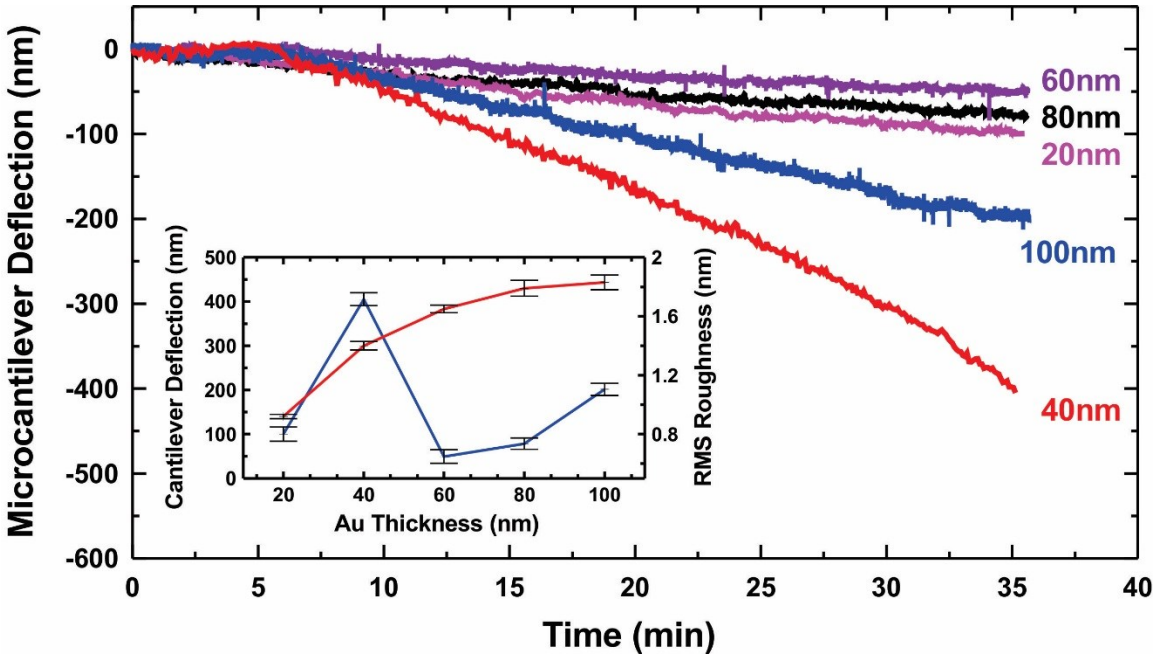

Figure 5.8: The effect of the Au film thickness on the microcantilever deflection when exposed to 10^{-6} M aqueous $CaCl_2$ solutions. The inset shows the cantilever deflection (blue curve) of each curve at 35 min and the RMS roughness values (red curve). Error bars correspond to the uncertainty values of the average microcantilever deflection at 35 mins obtained from three experiments, and the uncertainty of the RMS roughness values. This figure is a modified version of Figure 4 in Reference [165].

Based on the above findings, it is not possible yet to address the precise cause of the shape of the curve of the inset in Figure 5.8. However, these results clearly show that there is a delicate balance between the thickness and RMS roughness that needs to be further addressed. The response observed here is similar to that reported by Mertens *et al.* [50] who obtained a non-linear relationship between the Au film thickness and microcantilever sensitivity. Although we do not yet fully understand these observations,

the essential point was to consistently use the same thickness in order to be able to compare the results from different experiments.

5.4 Detection of Ca^{2+} ions

Once the optimum cleaning method, incubation time and gold thickness were recognized, experiments were conducted to examine the response of the calix[4]arene-functionalized microcantilevers to the injection of different target ions. The suitability of methoxy calix[4]arene-modified microcantilevers as a selective host for metal ions and especially Alkaline earth metal ions such as Ca^{2+}, Mg^{2+} and Sr^{2+} was first tested. Initial experiments were undertaken to detect trace concentrations of Ca^{+2} ions. Besides the environmental importance of detecting calcium in fresh water (see section 1.4), calcium is also an essential element in the human body playing a key role in regulating many different cellular functions. Calcium is important in body functions such as bone mineralization, regulation of enzyme activity, and cell growth [184]. It has also been stressed that detecting trace concentrations of calcium ions is important for both clinical and environmental applications [185]. The capability of methoxy calix[4]arene to selectively recognizing Ca^{2+} ions was shown by the solution-phase complexation studies conducted with NMR spectroscopy by the Georghiou group. The complexation studies of methoxy calix[4]arene with 14 different metal ions showed that methoxy calix[4]arene binds selectively to Ca^{2+} ions. Consequently, because of the importance of detecting calcium ions and the results obtained from NMR spectroscopy, microcantilever sensors

functionalized with methoxy calix[4]arene were used in order to attempt to detect of Ca^{2+} ions in aqueous solutions. In these experiments, RCA-cleaned microcantilevers were first coated with a 5 nm thin layer of Inconel as an adhesive layer followed by a 40 nm thin gold film. The gold-coated microcantilevers were subsequently incubated for 1h in a 1.0 μM solution of methoxy calix[4]arene. Reference microcantilevers were prepared in the same manner as the active microcantilever with the exception that the Au surface was functionalized with a 1.0 μM solution of decanethiol. As can be seen in Figure 5.9, the active microcantilever deflected as a result of the interactions between calixarene binding sites and target ions which induced a surface stress on the microcantilever surface causing the microcantilever deflection. The microcantilever deflection caused by the calixarene-target ion interactions is believed to be due to the intermolecular forces which induce a surface stress on the functionalized microcantilever. On the other hand, the reference microcantilever, which was coated with decanethiols, showed no apparent deflection indicating that the deflection of the active microcantilevers is caused by the interaction between the calix[4]arene binding sites and target molecules. Six different concentrations of $CaCl_2$ (10^{-6}, 10^{-7}, 10^{-8}, 10^{-9}, 10^{-10}, 10^{-11} M) were introduced to the microcantilever functionalized with calixarene molecules as shown in Figure 5.9. The primary objectives of these experiments was to assess the sensitivity of methoxy calix[4]arene-microcantilevers and to determine the lowest concentration of target ions that can be detected with our current system. We have been able to detect a target concentration of as low as 10^{-11} M. As demonstrated in Figure 5.9, the microcantilever deflection is a function of the target ion concentration where higher deflections are seen

for high concentration of target ion. Figure 5.9 also shows that microcantilever deflections reach a saturation state after approximately 20 mins. This implies that all target molecules have filled the binding sites on the calixarene molecules which were immobilized on the microcantilever surface.

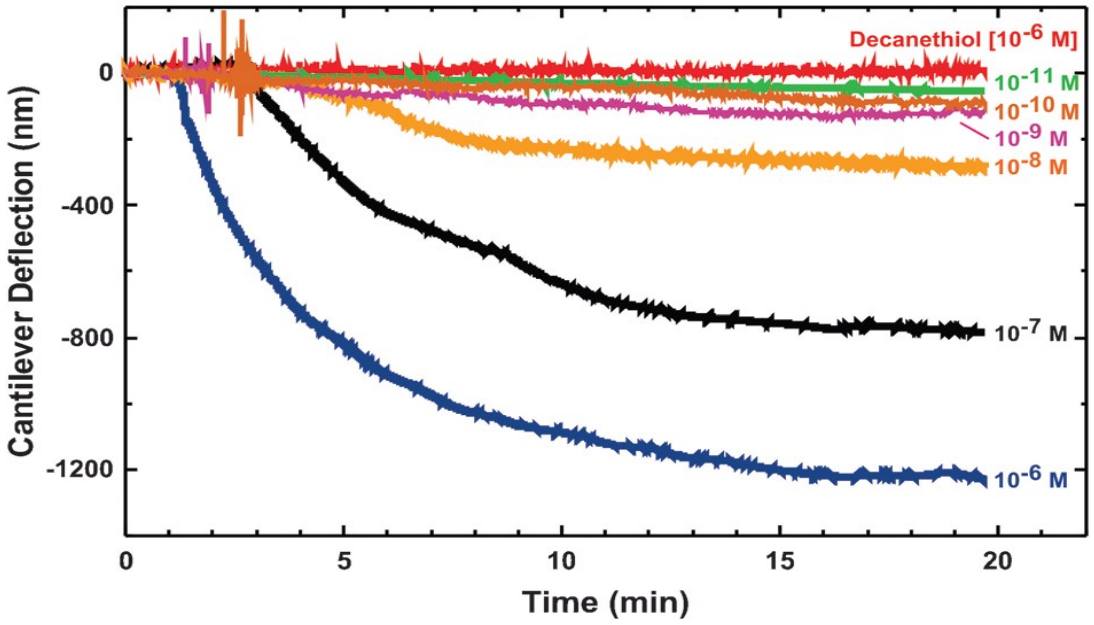

Figure 5.9: Responses to different concentrations of $CaCl_2$ for microcantilevers functionalized with methoxy calix[4]arene and a reference microcantilever functionalized with decanethiol [171].

Despite the fact that the microcantilever deflection is small for low target concentrations, it still exhibits a sufficient sensitivity to detect these small concentrations. It is noteworthy to mention that the results obtained with microcantilever sensors and shown in Figure 5.9 were found to be much more sensitive than those obtained with the ion-selective electrodes (ISE) by three orders of magnitude [185]. A calcium concentration of

10^{-8} M was reported to be detectable with ISE whereas calix[4]arene functionalized microcantilever sensors were able of detecting a concentration of as low as 10^{-11} M, indicating the high sensitivity of these sensors.

5.6 The Effect of cation on the selectivity of methoxy calix[4]arene-functionalized microcantilevers

The above results have illustrated the sensitivity of methoxy calix[4]arene-coated microcantilevers by recognizing the presence of calcium ions in solution. These results also showed that the microcantilever sensor was able to distinguish different concentrations of Ca^{2+} ions by undergoing larger deflections for higher concentrations. Therefore, subsequent experiments were conducted to assess the selectivity of methoxy calix[4]arene functionalized microcantilever sensors to other cations such as Mg^{2+} and Sr^{2+}. However, due to the fact that the results shown in Figure 5.9 were obtained from microcantilevers that were no longer commercially available (CSC 12, MikroMasch) at the time these experiments were conducted, it was therefore necessary to repeat the experiments shown above with the new microcantilevers (CSC 38, NanoAndMore) in order to assure that all experiments were conducted under similar conditions. Figure 5.10 shows microcantilever deflections as a function of different concentrations of aqueous $CaCl_2$ solutions with the new microcantilevers (CSC 38). As in the previous case, the microcantilever deflection was observed to increase with increasing $CaCl_2$ concentrations with a detection limit of the order of 10^{-12} M. The reference microcantilever, represented by the pink curve (labeled "Reference" in Figure 5.10), shows little change, indicating

that the microcantilever deflection of the functionalized microcantilevers was predominately due to the binding (or complexation) reaction between the calixarene sensing layer and the target ions. Although the data shown in Figure 5.10 only shows single microcantilever deflection curves for each compound, each experiment was repeated several times. The end deflection at 35 min, including the uncertainty, will be shown and compared with other results later (see Figure 5.13b). One of the notable observations in the data shown in Figure 5.10 is the lack of the saturation state which was seen in the data presented in Figure 5.9. This aspect is discussed in detail at the end of this section.

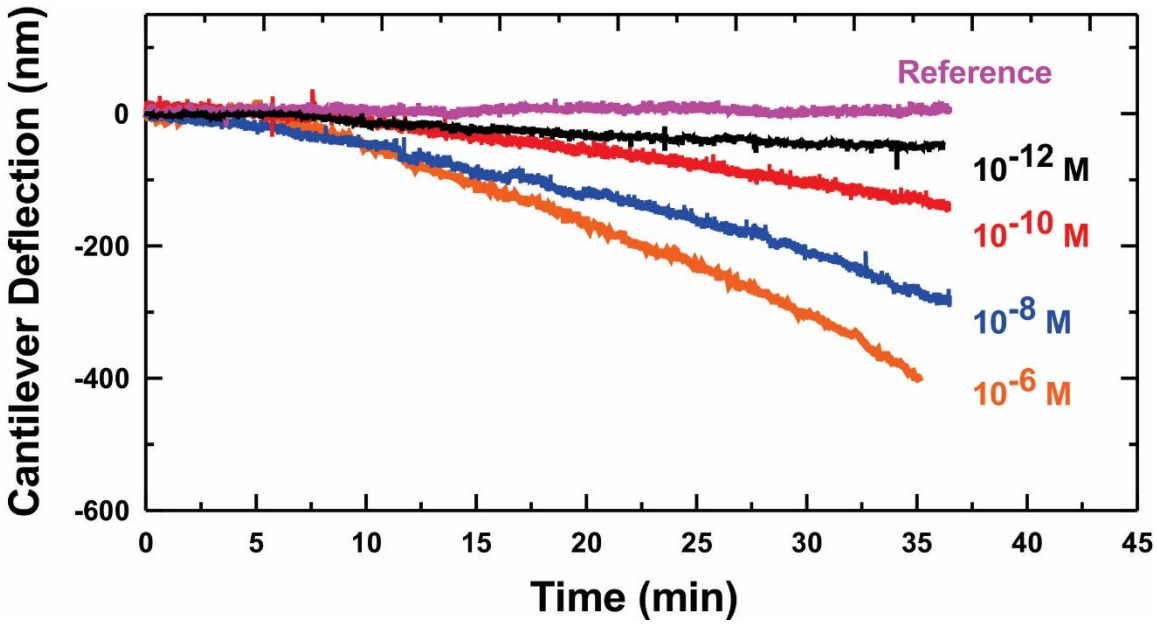

Figure 5.10: The microcantilever sensor response to varying concentrations of aqueous $CaCl_2$ solutions using the new microcantilevers (CSC 38). This figure is a modified version of Figure 5 in Reference [165].

Subsequent experiments were conducted to test the sensitivity of methoxy calixarene-coated microcantilevers to the introduction of aqueous solutions of $SrCl_2$ and $MgCl_2$. The reason for selecting the Mg^{2+} and Sr^{2+} cations was that they are both from the same group in the Periodic Table and have different ionic radii, with $Mg^{2+} < Ca^{2+} < Sr^{2+}$. In particular, it was of interest to see whether Sr^{2+}, being larger than Ca^{2+} would induce a larger surface stress on the microcantilever, or if Mg^{2+}, having a smaller radius, would more easily bind inside the cavity of the calixarene molecule and thereby produce larger microcantilever deflections. Figure 5.11a shows a comparison of the deflection signals of microcantilevers exposed to the same 10^{-6} M aqueous solutions of $CaCl_2$, $SrCl_2$, and $MgCl_2$ for the same period of time. The methoxy calix[4]arene-functionalized microcantilevers displayed a definite preference for Ca^{2+} over both $Mg^{2+}$and Sr^{2+}. Given that all three compounds had the same chloride counterion, it can only be speculated that the difference in the deflection signals originates from the size difference of the cations and their corresponding charge densities. The end deflection at 35 min for each compound including the associated uncertainty, calculated as described previously, is shown in Figure 5.11b. As in the previous case the error bars are approximately 10–15 nm indicating the excellent reproducibility obtained with our system.

The selectivity of the metal ion-complexing role of the podand groups in calixarenes has been well-documented in Ref. [169] and the rationale for this selectivity can be complex. The $-OCH_2CO_2CH_3$ podand groups attached to the lower rim of the methoxy calix[4]arene are shown here to be capable of binding to aqueous Ca^{2+} ions.

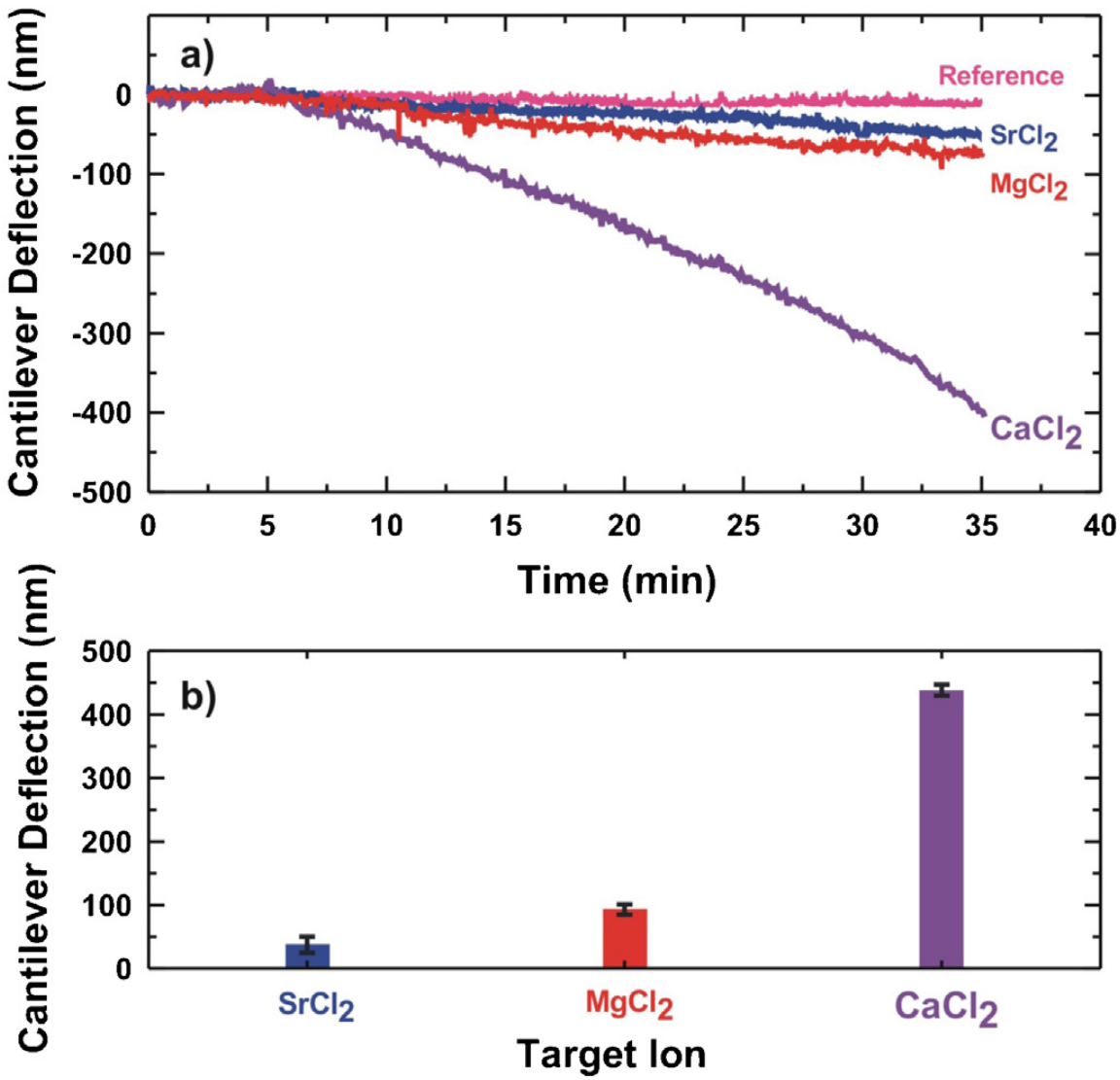

Figure 5.11: (a) Microcantilever sensor response to 10^{-6} M aqueous solution of $CaCl_2$ (purple), $MgCl_2$ (red), and $SrCl_2$ (blue). b) The microcantilever deflection plotted as a function of the different cations. Each datum point corresponds to the average microcantilever deflection obtained from three experiments [165].

It is apparent from the results shown in Figure 5.11 that the binding of the smaller Mg^{2+} ion by the surface-bound calixarene host does very little to increase the surface stress of

the microcantilever. It is possible also that desorption of the Mg^{2+} ions back into the aqueous medium could be competing with its binding to the calixarene host more strongly than is seen with either Ca^{2+} or Sr^{2+}. With Sr^{2+} as the target cation, we speculate that since it is larger than either Mg^{2+} or Ca^{2+}, it is too large for optimum binding with the calixarene host and it too binds more loosely with the upper-rim podand group of the functionalized layer creating a smaller surface stress.

As stated earlier, the main difference between the data shown in Figures 5.9 and 5.10 is the absence of the saturation state. In order to investigate this issue, methoxy calix[4]arene-functionalized microcantilevers were exposed to target ions with different concentrations for approximately 110 min. Such experiments were conducted in the hopes of gaining a better understanding of how the exposure time and concentration of the target ion would affect the existence of the saturation state. Figure 5.12 shows the response of methoxy calix[4]arene-functionalized microcantilevers to the injection of 10^{-6} M solutions of $CaCl_2$, CsCl and KCl. Although these data still clearly show that microcantilevers functionalized with methoxy calix[4]arene have a higher selectivity towards $CaCl_2$ over other target ions, the saturation state was not obtained even after 120 minutes of target exposure. The absence of the saturation state gives rise to many questions that remain to be addressed. One of these questions is whether this phenomenon is associated with the physical state of the microcantilever itself, or is related to the assembly of calixarene molecules or is influenced by both of them. In fact, the deflection curve and, in particular, the microcantilever saturation is a nontrivial issue

and has been an ongoing subject of debate in the microcantilever sensor community [186].

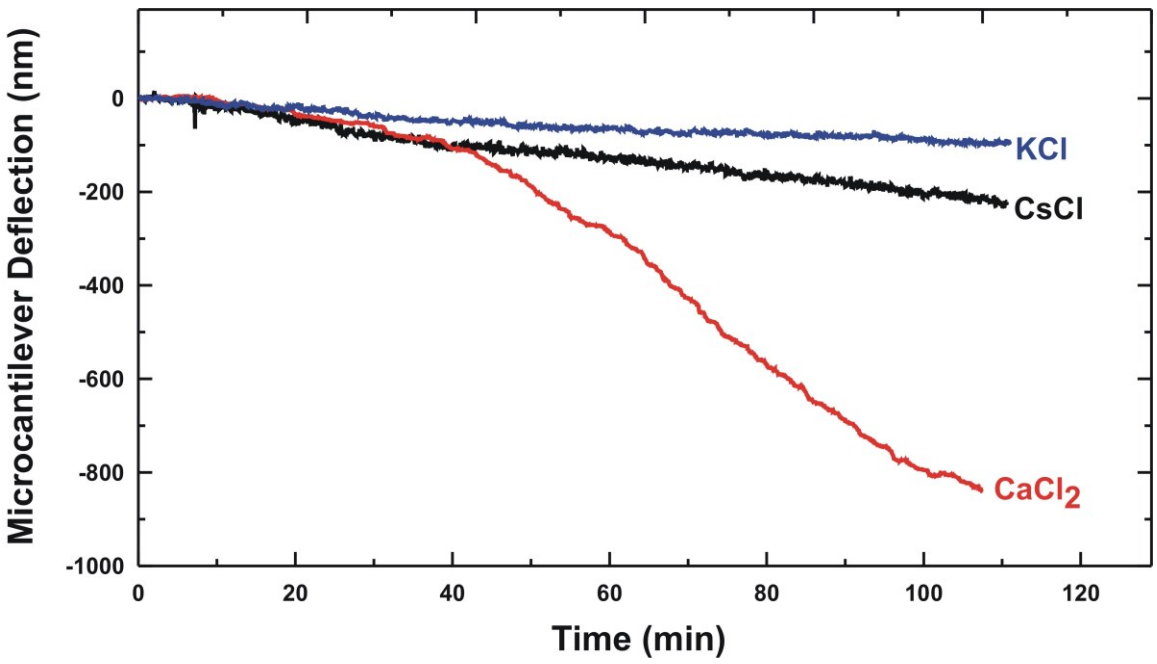

Figure 5.12: The response of microcantilever sensor functionalized with methoxy-calix[4]arene to the introduction of different 10^{-6} M target ions with different cation.

In efforts to further understand the mechanism behind the microcantilever saturation, a simple program was written to model the time it takes a microcantilever to reach the saturation state. This program aimed mainly at determining the time it takes for the target ions to fill the binding sites of the calixarene cavities. Based on the STM image shown in Figure 5.2, each methoxy calix[4]arene molecule occupies an area of 2.35 nm^2 on the surface of Au-coated microcantilever. This program included a calculation that took into account the number of receptors on the microcantilever determined from the number of

particles per liter from the solution concentration. In this program, we also assumed that only 50% of target particles are moving towards the microcantilever and a fraction of these target particles (i.e. assuming binding efficiency of 80%) will be captured by the microcantilever. By also considering the cell volume in which methoxy calix[4]arene microcantilever was immersed, the available targets (assuming uniform concentration) and the flow rate, we found that a 10^{-6} M solution should cause the microcantilever to reach saturation within several minutes. However, this prediction is not what was observed and shown by our data. To reach a point of saturation the force exerted on the microcantilever caused by the surface stress generated by the host/guest complexation reactions occurring on the microcantilever surface must be in equilibrium with the reaction force of the microcantilever. The other factor that affects the saturation point is the way in which the target is delivered to the microcantilever. In microfluidic systems, such as our microcantilever sensor setup, fluid is never turbulent but instead highly laminar. For our single microcantilever system, fluid dynamics simulations were recently performed in our group in order to study the flow of target solutions in the system [64]. As the target solution is introduced into the cell, the majority of the fluid stream follows a clear path from the fluid cell input to the output while a small portion of the solution slowly mixes with the water within the rest of the cell. Although the concentration of target molecules around the microcantilever may be at a maximum, the fact that the fluid is in motion greatly reduces the ability of the targets to bind with the receptors on the microcantilevers. This in turn explains why even at large concentrations such as 10^{-6} M, the cantilever never reach saturation. In the simulations reported by Manning *et al.* [64],

although the force of attraction was increased by a factor of 10, only 0.2–2% of the target particles were detected under identical experimental conditions used here. In other work, McKendry *et al*. [188] reported that only 1 in 75,000,000 particles injected into their microcantilever sensor cell was detected by the cantilever. Hence, we can infer that the notion of cantilever saturation is keenly related not only to the cantilever itself but also to the geometry of the cantilever sensor fluid cell and the way in which the target solution is presented to the microcantilevers.

5.7 The Effect of counter ion on the selectivity of methoxy calix[4]arene-functionalized microcantilevers

Following the experimental investigations of the effect of cations on the response of methoxy calix[4]arene-modified microcantilevers, experiments were conducted to examine the response of the methoxy calix[4]arene-modified microcantilever to the injection of a target with the same cation but with a different anion. As illustrated in Figure 5.13a, results showed that the microcantilever was able to detect the interactions between calixarenes and $Ca(NO_3)_2$ with a concentration as low as 10^{-12} M. As shown in Figure 5.13b by the blue data for $Ca(NO_3)_2$, the microcantilever deflection is approximately linear with the log of the $Ca(NO_3)_2$ concentration. Similar to $Ca(NO_3)_2$, the same trend was observed for $CaCl_2$, as shown in Figure 5.13b, by the red data, with the main difference being that the slope for $Ca(NO_3)_2$ was less than that of the $CaCl_2$ data,

indicating that the methoxy calix[4]arene host is much more receptive to $CaCl_2$ than to $Ca(NO_3)_2$.

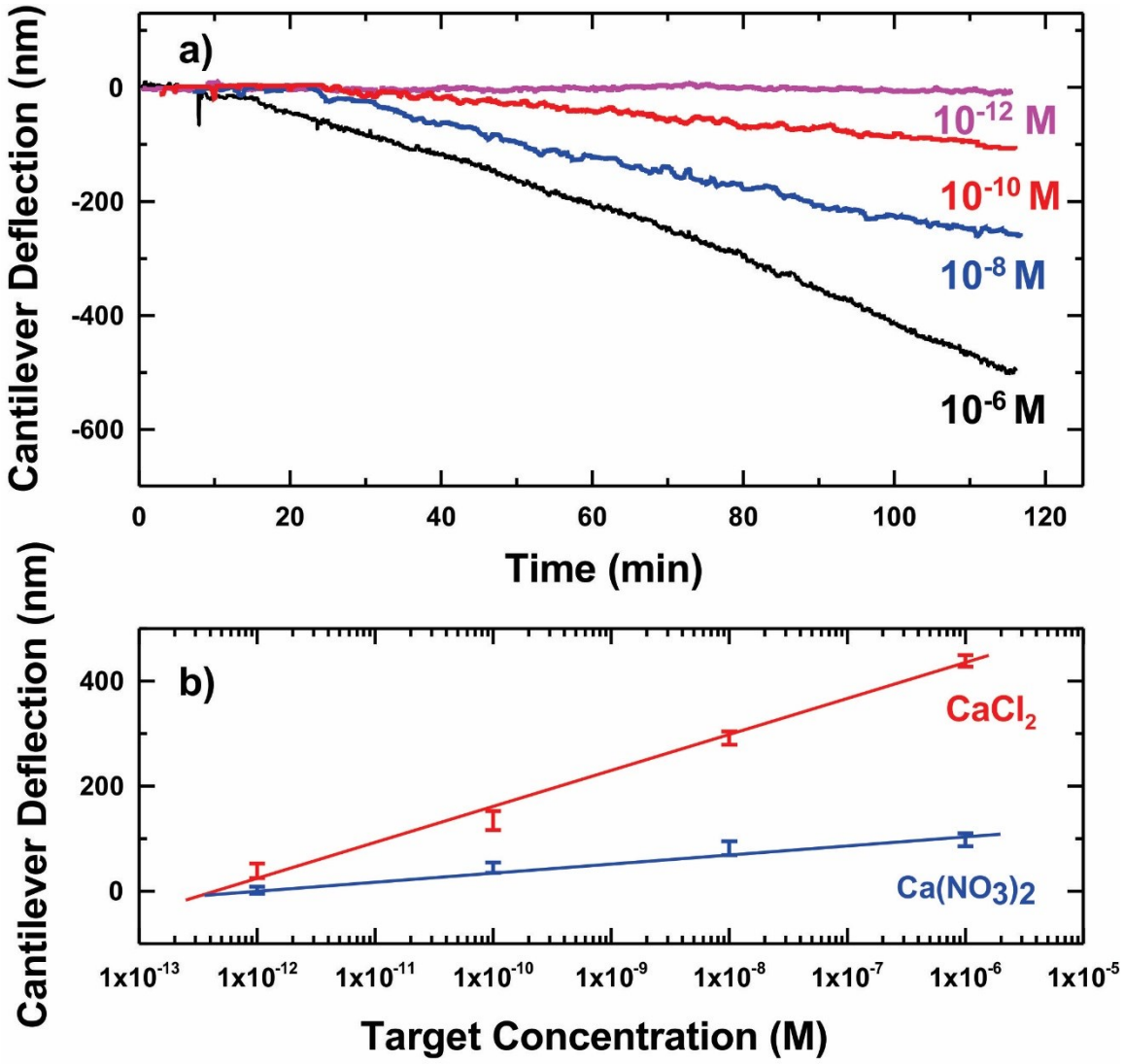

Figure 5.13: (a) Injection of different concentrations of $Ca(NO_3)_2$ solution. (b) The microcantilever sensor response as a function of target ion concentration for $CaCl_2$ (red data) and $Ca(NO_3)_2$(blue data). Each datum point on this plot represents the average microcantilever deflection obtained from three experiments with error bars calculated as described within the text. This figure is a modified version of Figure 4 in Reference [165].

Other anions associated with the calcium salts were also tested and were also found to influence the microcantilever response. As shown in Figure 5.14, the methoxy calix[4]arene-functionalized microcantilever exhibited a large response to aqueous $CaCl_2$ solutions allowing trace concentrations as low as 10^{-12} M to be detected. Initially, it was expected that these sensors would be equally responsive to all water-soluble calcium salts. However this was found not to be the case. Figure 5.14 shows a comparison between four different calcium salt solutions. $CaBr_2$, CaI_2, and $Ca(NO_3)_2$, were chosen to be compared with $CaCl_2$ in order to better understand the potential effect of their corresponding counterions on the response of the methoxy calix[4]arene-functionalized microcantilevers. The data shown in Figure 5.11 indicates that the chloride anion has no effect in inducing large microcantilever deflections when coupled with either Sr^{2+}or Mg^{2+}. However, the results shown in Figure 5.14 clearly indicate that the Cl^-, Br^-, $I^-$and NO_3^- counterions of these salts do play a significant role in the binding or complexation dynamics of the calcium ion with the bimodal methoxy calix[4]arene immobilized on the surface of the microcantilever. The deflection trend seen, namely Cl^-> Br^-> I^- for the calcium halides (tested under the same aqueous concentration and conditions) follows the same trends observed by others, including ourselves, when comparing the binding properties of halides in solution studies with other host molecules [189,190], including calixarenes [169]. Hence this indicates that the microcantilever deflections are due to the target ionic species as a whole instead of only the specific cation and/or anion.

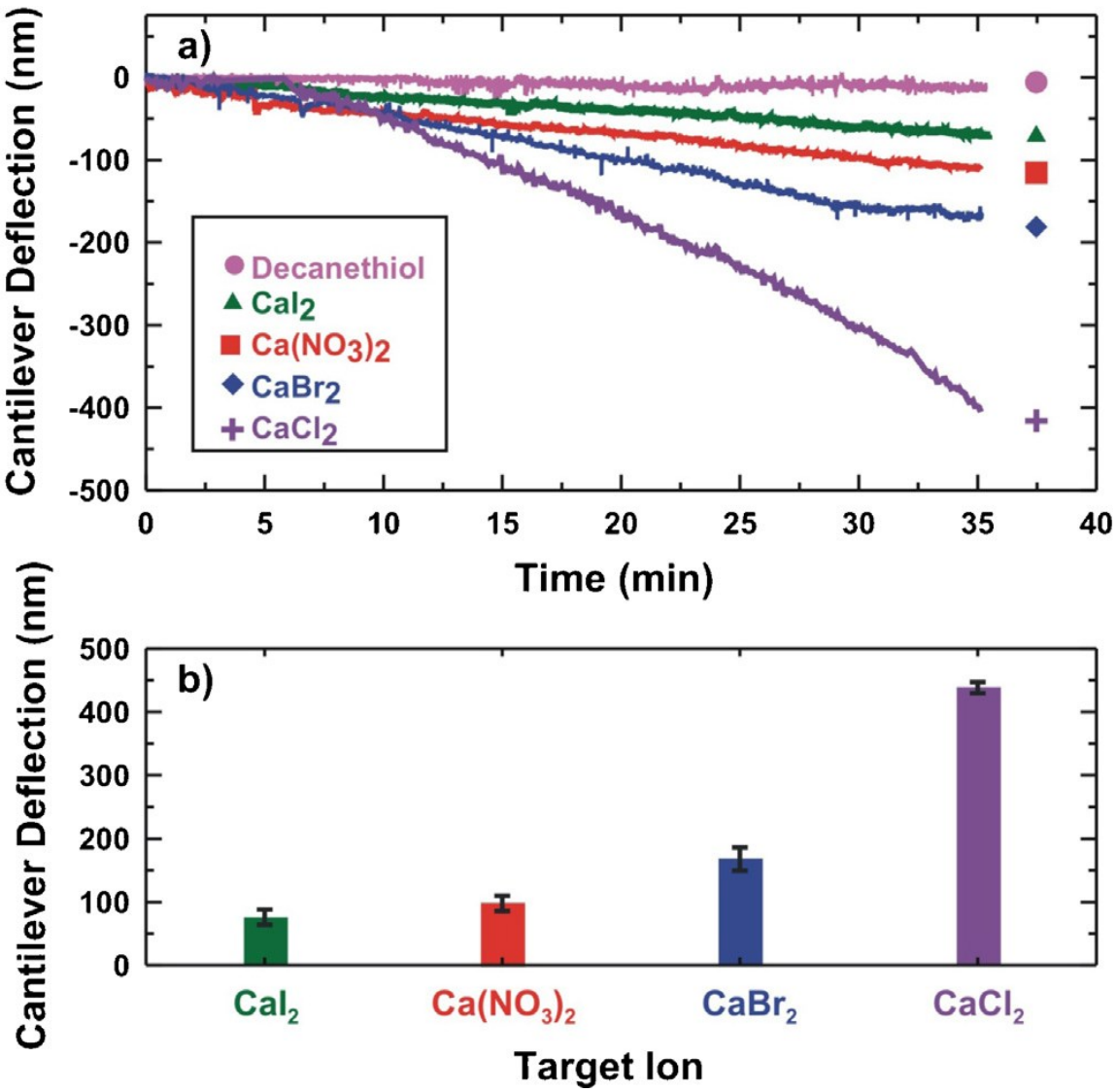

Figure 5.14: (a) The microcantilever deflection in response to 10^{-6} M aqueous solutions of $CaCl_2$ (purple), $CaBr_2$ (blue), CaI_2 (green), and $Ca(NO_3)_2$ (red). The mauve curve shows a typical response of the reference microcantilever (coated with decanethiol) to the aforementioned solutions. (b) The response of the methoxy calix[4]arene-functionalized microcantilevers to the variation in the counterion. Each datum point corresponds to the average microcantilever deflection obtained from three experiments [165].

It is also possible to rule out any interaction of these counter ions with the Au film on the microcantilevers since any such interaction would have also occurred on the reference microcantilever. Hence the deflections caused by these interactions would have been eliminated in the differential measurements reported here (active signal–reference signal). In the event that these ions would have somehow preferentially bound with the active microcantilever only, the chemisorption of I^- would have generated a larger deflection than either Cl^-or Br^-, since it binds with the largest surface mismatch with Au which would lead to the largest surface stress and hence microcantilever deflection [191]. However this is not what is observed as shown in Figure 5.14.

An explanation for the results shown in Figure 5.14 is not immediately obvious. Clearly, in aqueous solution all four of the calcium salts are dissociated into their respective calcium ions and anions at the concentrations used, as can be determined by their reported solubilities in water. Thus, in aqueous solution both the cations and anions are hydrated as represented schematically in Figure 5.15a for $CaCl_2$. However, when the cation is bound to the calixarene host, the resulting complex necessarily requires the corresponding counterions to neutralize the charge on the complex (see Figure 5.15b). The observed results suggest that the sizes and the shapes of both the cation and its counterions ultimately affect the binding of the ionic species to the calixarene host on the microcantilever surface, and consequently, its response. Molecular modeling calculations (DFT/B3LYP/6-31G(d) gas-phase) [192] on the three halides show volumes ($Å^3$) of 23.70, 28.08 and 34.78, respectively, for the Cl^-,Br^-, I^- ions. The increase in volume of these spherical anions is inversely related to the microcantilever deflection seen with the

corresponding calcium halides. Although the computed volume of the NO_3^-anion is larger (44.14 $Å^3$) than that of the iodide ion but gave a larger microcantilever deflection than that of I^-, it should be noted that its trigonal planar shape is different to those of the halide ions and thus cannot be directly compared with them. Hence we hypothesize that if the anions are larger than Cl^-, as would be the case for Br^-, I^- and NO_3^-, the "ion triplet" [189] formed by the calcium ion and its two associated counterions would not be as deeply encapsulated by the calixarene host as represented in Figure 5.15c, and hence would not be bound as strongly with the calixarene receptor as for example $CaCl_2$ which in turn would create very little stress on the microcantilever, as observed here.

It has also been reported that the complexation between calix[4]arene compounds and the metal ions can be affected by factors other than the cavity size of the calix[4]arene and the ionic radii of target ions. These suggested factors are the pH of the target solution, electronic pairing between the calix[4]arene binding sites and the cation, electrostatic charges, and entropy [193,194].

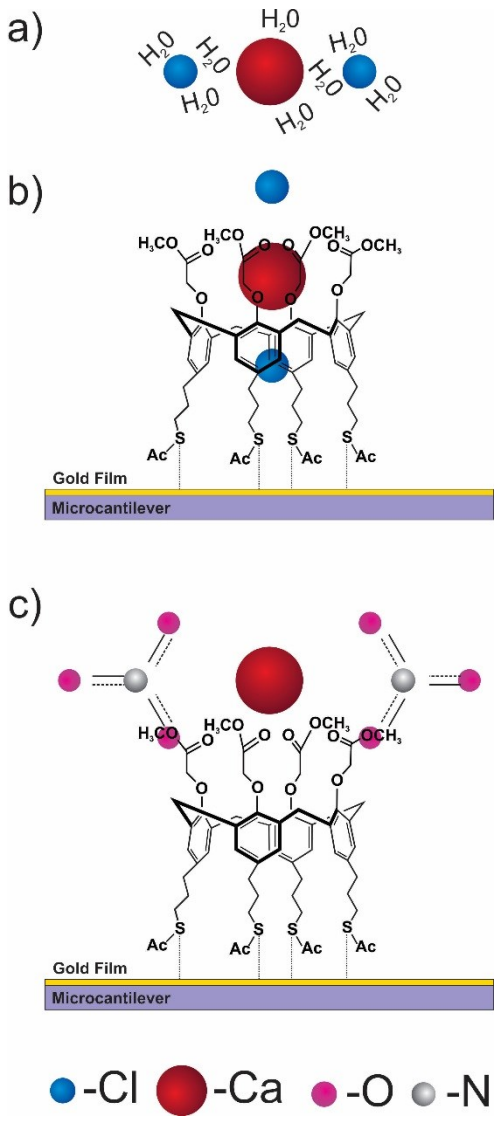

Figure 5.15: a) Intimate ion triplet formed by CaCl2 in aqueous solutions. b) The interaction mechanism of the hydrated $CaCl_2$ molecule with methoxy calix[4]arene. c) The reaction of hydrated $Ca(NO_3)_2$ with methoxy calix[4]arene.

The binding strength between a guest and host can be quantitatively measured by calculating the complexation constant [K]. The determination of the complexation constant from the microcantilever deflection was first reported by Feng Ji *et al*. [186]. They stated that the complexation constant can be obtained from the microcantilever deflection using the following equation [186]:

$$\delta = b\left(\frac{3(1-v)L^2}{Et^2}\right)\left(\frac{K[M]R}{1+K[M]}\right). \quad (5.1)$$

where δ is the microcantilever deflection, v is the Poission's ratio, L is the microcantilever length, E is Young's modulus, t is the microcantilever thickness, K is the complexation constant, M is the ionic concentration, and R is the number of moles of the ion receptor on the microcantilever surface. A plot of "1/ δ " vs "1/[M]" gives the value of K. Given that the microcantilever deflection is obtained from the experimental results and M is known, it was possible to obtain a complexation constant values of 6.5×10^{10} M^{-1} for Ca^{2+}, 1.7×10^{9} M^{-1} for Cs^{+}, and 2.9×10^{9} M^{-1} for K^{+}. These values clearly show that the Ca^{2+} has a higher complexation value with the calixarene than others, suggesting a high binding degree between methoxy calix[4]arene and $CaCl_2$ molecules.

5.8 Sensing measurements of crown calix[4]arene

Following the examination of the sensitivity and selectivity of methoxy calix[4]arene towards specific metal ions, experiments were conducted to test the affinity of crown calix[4]arene-functionalized microcantilevers to specific metal ions in aqueous solution. Following the same experimental procedure as before, the response of crown calix[4]arene coated microcantilevers to four different aqueous (5.0 μM) metal chloride solutions were monitored. Since we had previously noted significantly greater responses to chloride counterions in the case of calcium halides with the methoxy-calix[4]arene, aqueous solutions of $CaCl_2$, KCl, RbCl and CsCl were tested [172]. As demonstrated in Figure 5.16a, the crown calix[4]arene-functionalized microcantilever showed the highest affinity towards CsCl over other metal ions. The largest deflections seen were for Cs^+ which was significantly greater than the deflection seen for K^+ similar to what was reported by Ji *et al.* [186], although in their case their receptor was a benzo-crown-6 moeity. The deflection seen with Rb^+ was smaller than with Cs^+ but greater than K^+. In addition, in our case only a relatively weak response was seen to $CaCl_2$ which, for methoxy calix[4]arene, showed the largest deflections. This latter result is not surprising as it is well-known in the literature that crown ethers are highly selective towards particular metal cations [169,195]. In order to clearly demonstrate the repeatability of results obtained for different target ions, the average microcantilever deflection for three experiments of each concentration was measured and shown in Figure 5.16b. Each error

bar corresponds to the standard deviation obtained from three separate experiments. This figure shows the excellent reproducibility obtained from our system.

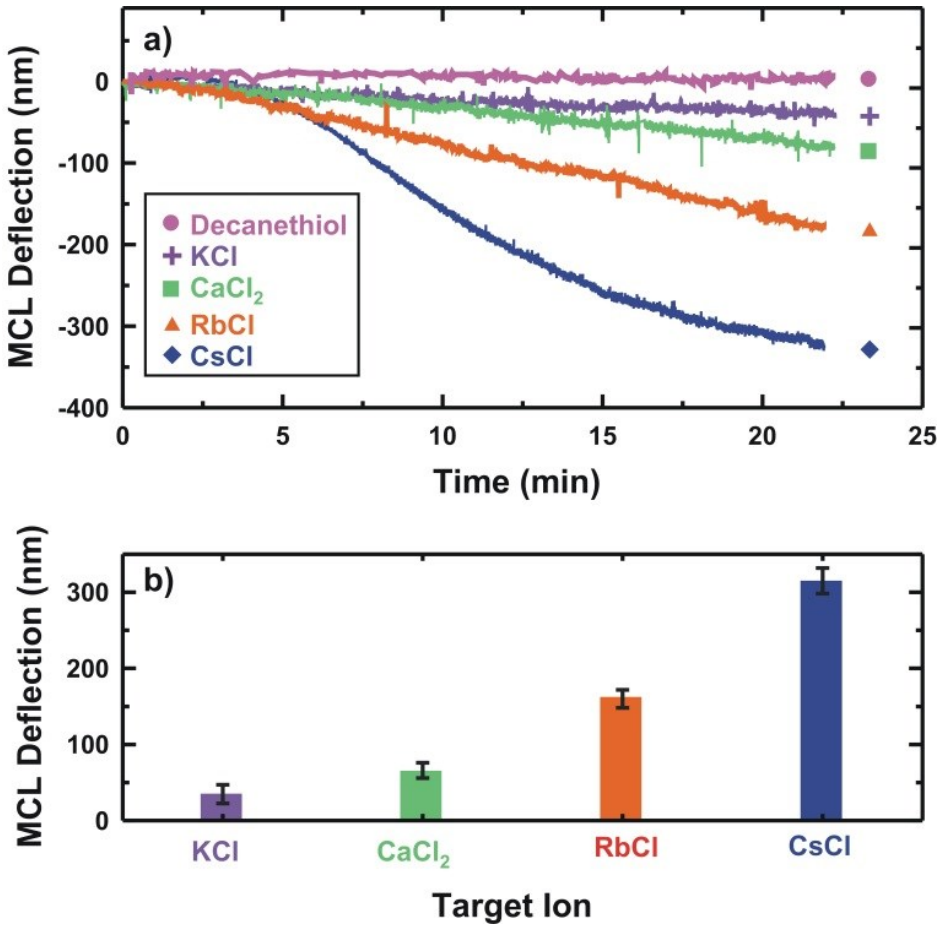

Figure 5.16: (a) The response of microcantilever sensor functionalized with crown calix[4]arene to different target ions. (b) The microcantilever deflection plotted as a function of the different target ions. Each datum point represents the average microcantilever deflection obtained from three experiments with the corresponding standard deviation shown by error bars [172].

5.9 Summary

The experimental findings reported in this chapter clearly indicate that the microcantilever sensitivity can be greatly affected by the Au thickness and the incubation time. It can also be speculated that the Au thickness is one of the key parameters responsible for many conflicting published reports discussing the influence of the RMS roughness of the Au film on the sensitivity of microcantilever sensors. It was also confirmed by STM imaging that modifying the calix[4]arene with thioacetate grouping enabled them to form SAMs on the Au surface of the microcantilever. Results also showed that both methoxy and crown calix[4]arenes can be used as host/guest-type receptive layers for microcantilever sensors. Methoxy calix[4]arenes-functionalized microcantilevers were capable of detecting trace concentrations of $CaCl_2$ in aqueous solutions down to 10^{-12} M which is sufficiently low for most applications. This calix[4]arene sensing layer also showed a definite affinity toward aqueous solutions of $CaCl_2$ over other ionic species such as Mg^{2+} and Sr^{2+}. On the other hand, crown calix[4]arene microcantilevers showed sensitivity to aqueous Cs^{+} and to a lesser-extent to Rb^{+} and Ca^{2+} ions and a negligible response to K^{+} [172]. These results have confirmed the capability of calix[4]arenes-modified microcantilevers to serves as effective target ion sensors.

Part II

Experimental Studies Using

Microcantilever Array System

Chapter 6 Development of New Microcantilever Array Experimental set-up

The investigation of the capability of microcantilever sensors for being reliable and versatile sensing platforms requires the development of an experimental apparatus that allows for accurate determination of such properties. As stated previously, the microcantilever sensitivity can be significantly affected by the geometry of the delivery system of the target analyte as well as the position of the microcantilevers in the cell and thus the design of a microcantilever sensor apparatus should take into account all possible influencing factors. An ideal experimental platform for a microcantilever sensor should be designed in such a way that it allows for the direct interactions between the analyte molecules and the chemically modified microcantilevers. A critical part of this work has been to develop a new microcantilever sensor set-up. The objective of designing a new experimental set-up is to obtain simultaneous measurements allowing multiple microcantilevers with different coatings to be monitored. The new system allows up to 16 individual microcantilevers to be used at one time. The key advantage of using the 16-microcantilever system is that measurements of the responses of active and reference microcantilevers can be evaluated simultaneously. Modifying microcantilevers in the array with different sensing layers was made possible by the use of the functionalization

unit, which is discussed in section 6.3 of this chapter. The development of the new experimental setup was conducted through four stages:

- A complete 3D drawing of the microcantilever sensor setup and of the functionalization unit was created using AutoCAD.
- All parts were machined according to the AutoCAD drawings. The system was then assembled.
- Software to control the setup and analyze the data was developed and tested.
- The system was tested and finalized.

6.1 System Components

As shown in Figures 6.1 and 6.2, the major components of the new microcantilever sensor set-up include the fluid cell, optical focusers, optical microscope, 2D PSD, and an actuator translation stage. In order to minimize the effect of vibrations from external sources, the sensor cell containing the microcantilever arrays was placed on a vibration-free platform. The entire experimental system was placed on a wooden box lined with sound proof material in order to minimize environmental effects such as the light that interferes with the PSD from processing of the laser beam during experiments. A schematic representation of the new microcantilever array experimental system is demonstrated in Figure 6.1. Each component of the new system is described in detail below.

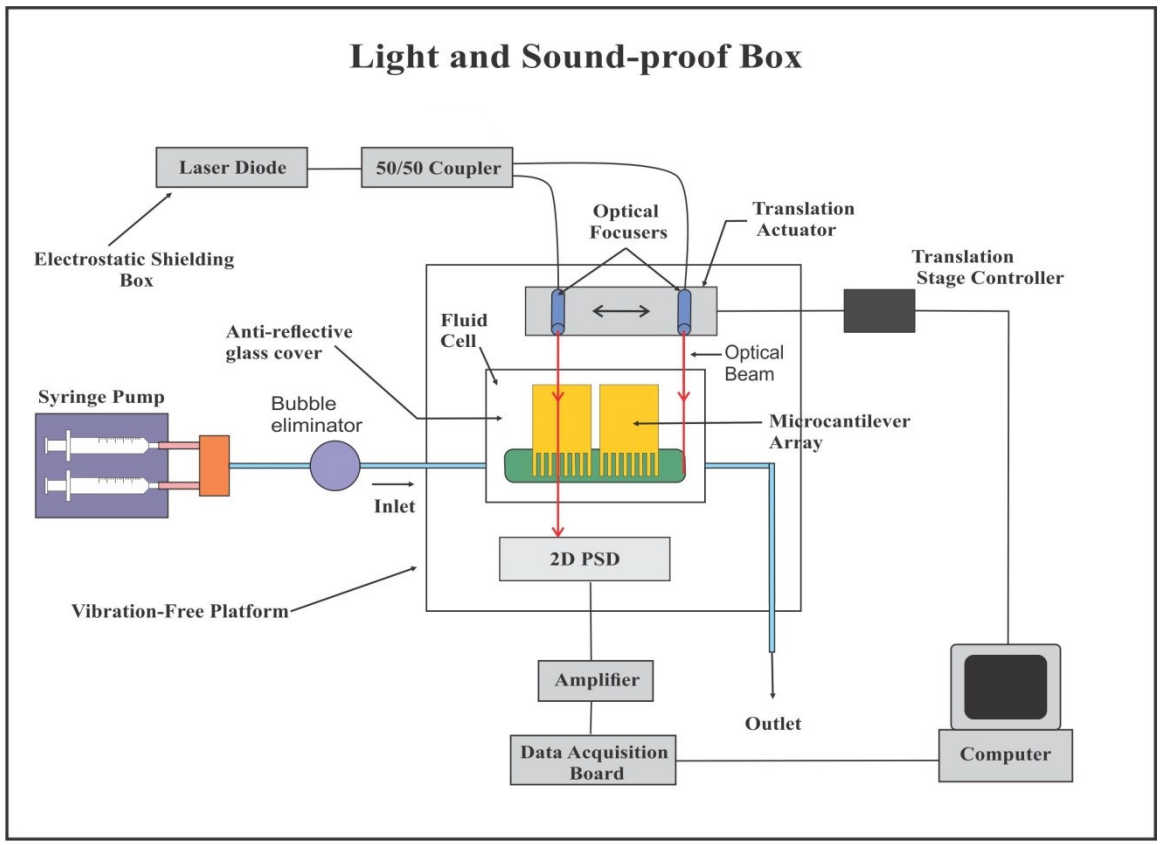

Figure 6.1: Schematic representation of the 16-microcantilever sensing platform.

6.1.1 Fluid Cell

As shown in Figures 6.1 and 6.2, the fluid cell is placed at the center of the platform. The fluid cell was made of stainless steel which is resistant to the chemicals used in this work. This is important to ensure a minimal effect of the fluid cell on the experimental results thus increasing the accuracy of the measurements. Stainless steel is a highly resistant material even to certain acids, making it possible to use various cleaning methods when cleaning the system. The cell was designed to accommodate two chips each with eight microcantilevers. The fluid cell is connected to two tubes in order to transport solutions to and from the fluid cell. These two tubes, made of Polyether Ether Ketone (PEEK) which is non-reactive with organic compounds, are connected to a programmable syringe pump which allows the injection of different solutions. During experiments, it is necessary to introduce different solutions which require that syringes to be changed. This leads to the formation of bubbles inside the fluid cell which prevents the laser beam from reflecting from the microcantilevers. Therefore, a diverter was constructed and placed between the syringe pump and the fluid cell, as schematically shown in Figure 6.1. This diverter allows the injection of a new solution without the need to disconnect the first syringe, and thus preventing the formation of bubbles inside the fluid cell.

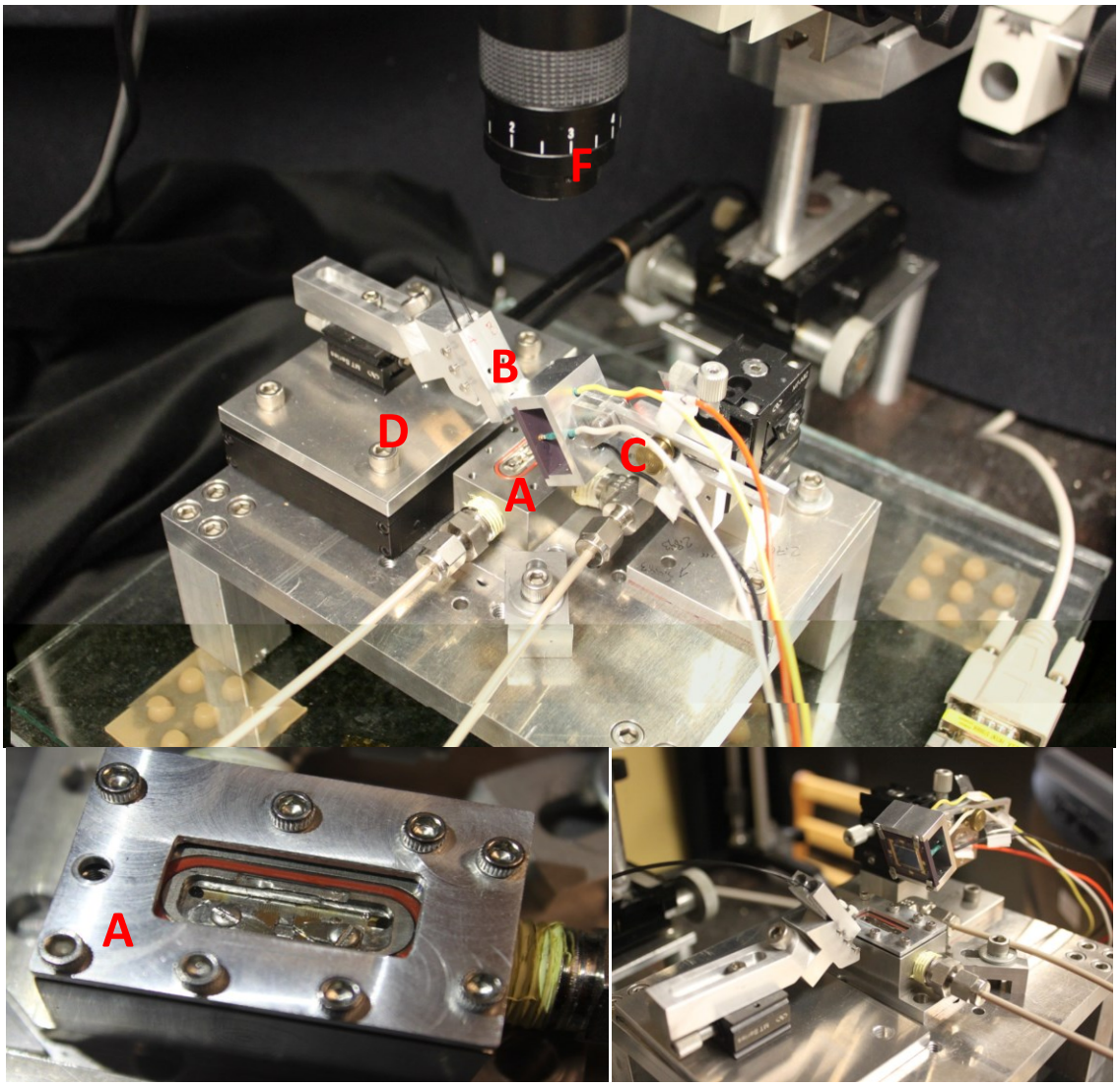

Figure 6.2: A photograph of the new microcantilever set-up. A) Fluid cell, B) Laser holder, C) 2D PSD, and D) Actuator translation stage assembly, F) Optical microscope.

6.1.2 Lasing System

Measurements of the microcantilever response using an optical beam deflection system require the use of a laser beam which is focused onto the free end of the microcantilever using optical focusers. Two optical focusers (LPF-01-635-4/125-S-2.6-15-4.5AC-40-3S-3A-1, OZ optics) were used to focus the 17 mW laser beam generated from a laser diode (FMXL0658-017SF0A, Blue Sky Research). The power and temperature of this laser is monitored by using a precision current source (LDX-3412, ILX Lightwave Corp) and a temperature controller (LDT-5412, ILX Lightwave Corp) respectively. The laser diode was held by a laser mount (LDM-4980, Lightwave Corp) and placed in an electrostatically shielding box since static electricity can adversely affect the reliability of the laser diode and can even cause a breakdown of the diode. The reason for using a single laser beam source is to assure that all microcantilevers experience the same laser intensity. The laser beam operating at a wavelength of 635 nm is divided using a 50/50 coupler (FUSED-12-635-4/125-50/50-3S3S3S-1-0.5, OZ Optics) which preserves the laser beam characteristics such as the power and wavelength. The two optical focusers constituted of achromatic lenses, focusing the laser beam to a spot size of approximately 12 μm at a working distance of approximately 15 mm. As there are two microcantilever arrays used, a laser holder was made to hold two focusers as shown in Figure 6.2 B. The laser holder is attached to a translation stage so that the incident beam could be adjusted onto the desired microcantilever. The optical focusers attached to the translation actuator made it possible for the laser beam to move across the microcantilevers. The position of

the laser beam on the microcantilever can be visualized using an optical microscope as shown in Figure 6.2 F.

6.1.3 Position Sensitive Detector (PSD)

The reflected beam off the microcantilever surface is detected using a two axis position sensitive detector (PSD). In contrast to discrete element devices such as charge-coupled devices (CCD), the PSD features fast response time, high position resolution and simple operating circuits [196]. A PSD is a silicon-based device that can measure the position of an optical beam on its surface and convert it into analogue output signals with high accuracy. The capability of providing continuous position data is the main advantage of the PSD. There are two common types of silicon-based PSDs. The first type is the four segments PSD which is commonly used in AFMs. Despite the high sensitivity of the segmented PSD, it requires the light intensity to be uniformly distributed over the active area of the PSD in order to generate a linear response. This drawback of the segmented PSD is overcome by the use of a linear PSD, which is the second type of PSD. A linear PSD provides a high linearity over the active area and thus eliminating the need to adjust the laser beam on the center. In this work, a 2D duolateral linear PSD (2L2SP, On-Track Photonics Inc) with an active area on the order of 10×10 mm (as shown in Figure 6.3) was used. The PSD is adjusted so that the laser beam reflecting off each microcantilever surface is incident on the active area of the device. The PSD is also attached to a translation stage allowing it to be moved and aligned with precision (see Figure 6.2 C).

When the laser beam hits the PSD surface, photocurrents are generated and converted into voltages X_1, X_2, Y_1 and Y_2 by a transimpedance amplifier. The converted voltages are then processed by a diving chip to provide the light positions X and Y independent of the light intensity:

$$X = \frac{X_1 - X_2}{X_1 + X_1} \times \frac{L}{2}. \tag{3.1}$$

$$Y = \frac{Y_1 - Y_2}{Y_1 + Y_1} \times \frac{L}{2}. \tag{3.2}$$

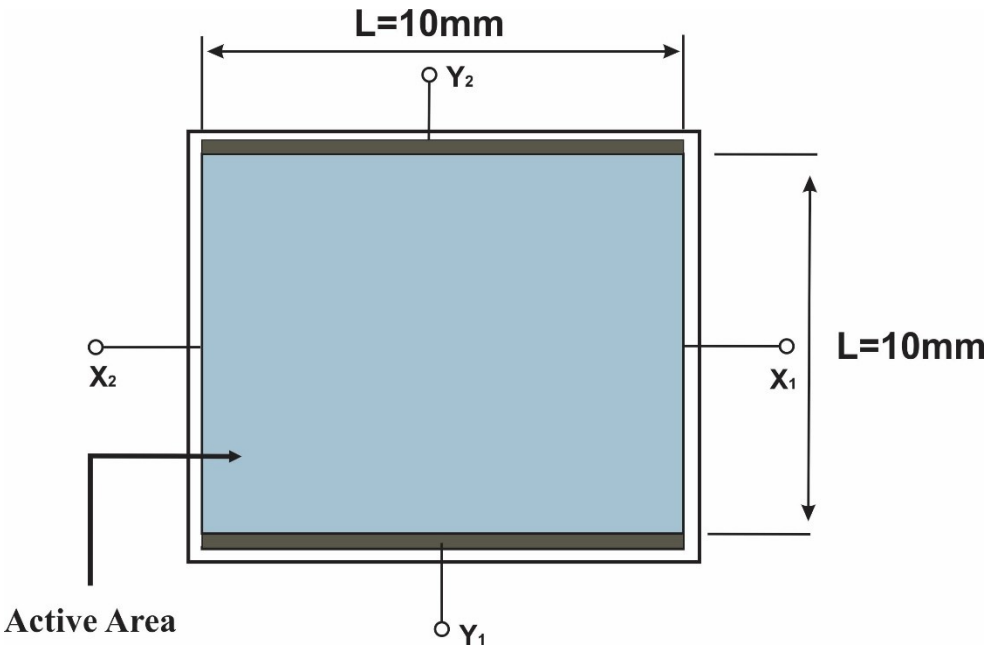

Figure 6.3: A schematic representation of the linear photo sensitive detector (PSD) where the active area is highlighted in blue.

The PSD voltages V_x and V_y are directly proportional to the light beam position on the PSD surface, from which the microcantilever deflection can be inferred. The acquisition of the PSD signals was done using a data acquisition (DAQ) board (PCI-6221, National Instruments) allowing the data to be recorded by a computer via acquisition software written in Visual Basic.

6.1.4 Translation Actuator

A high resolution motorized actuator was used to move the optical focusers back-and-forth so that each microcantilever can be interrogated one at the time. This actuator uses a 12 DC servomotor that provides sufficient torque for high load capabilities. This actuator can travel a distance of 12 mm which is sufficient to move optical focusers so that the laser beam can strike all 16 microcantilevers. The motorized actuator is coupled to a translation stage on which the optical focusers are attached. An assembly of the motorized actuator is shown in Figure 6.2 D. As the translation actuator can operate with different motion parameters such as velocity, acceleration, and step size, it was necessary to fine tune these parameters to achieve the desired performance. The calibration procedures of these parameters are discussed in the following section.

6.2 Calibration and Analysis software

Calibration of the new system involved understanding the voltage signal obtained from the two dimensional PSD and the optimization of the motion parameters of the translation stage. After the construction of the new microcantilever sensor setup was complete, the next step was to design and implement the data analysis software. The new microcantilever system required that a program be written to synchronize the data from the translation stage and the PSD data to obtain the deflection signal originating from each individual microcantilever. The development of this software, written in Microsoft Visual Basic, was conducted in three main phases. The first phase involved writing a program that controls the motion of the motorized translation stage. This program also allowed to optimize the parameters of the motorized actuator such as velocity, acceleration and step size which in turn influenced the shape and the accuracy of the peaks representing the microcantilever deflection. The development of this phase was performed in collaboration with Dr. Saydur Rahman, a postdoctoral fellow in our research group. My involvement in the first phase was to write the VB codes that interface to the translation stage without resorting to using the software provided by the manufacturer which only allows controlling the motion of the translation stage without the possibility of interacting with other software. After the translation stage was interfaced to our VB software, the next step was setting the motion parameters of the stage and writing the data to a file. By the use of this software, the initial and final positions, velocity, acceleration and the step size of the motorized stage can be controlled

with high resolution. The *x*-position data of the translation stage can also be defined and saved into a file. The second phase included modifying the existing data acquisition software to record the data obtained by the 2D PSD. The DAQ software was initially developed by Meng Xu to record the data from two separate PSDs. This software was modified by us so that it can collect the *x* and *y* signals of the 2D PSD. The third phase involved programming the data analysis software, which incorporates the data from the two programs mentioned above to provide the deflection signal of each microcantilever in the array. The major contribution to the programming of this software, which is discussed in greater details below, was made by Dr. Luc Beaulieu.

Figure 6.4 show the raw *x versus* time and *y versus* time data respectively obtained with the PSD during an experiment where 16 Au-coated microcantilevers from two 8-microcantilever arrays were subjected to hot water (approximately 90°C). The *y* data (Figure 6.4b) provides the deflection of the cantilevers. Each peak in the figure corresponds to a single microcantilever. The software was written to fold the data in such a way that all the peaks from each microcantilever lined-up one on top of each other. This software correlates the *x*-position data obtained from the translation stage software with the *y*-position data obtained from the PSD data acquisition software. An important step in developing this software was to associate the time of the PSD data to the position of the translation stage so as peaks from the same microcantilever are superimposed on each other.

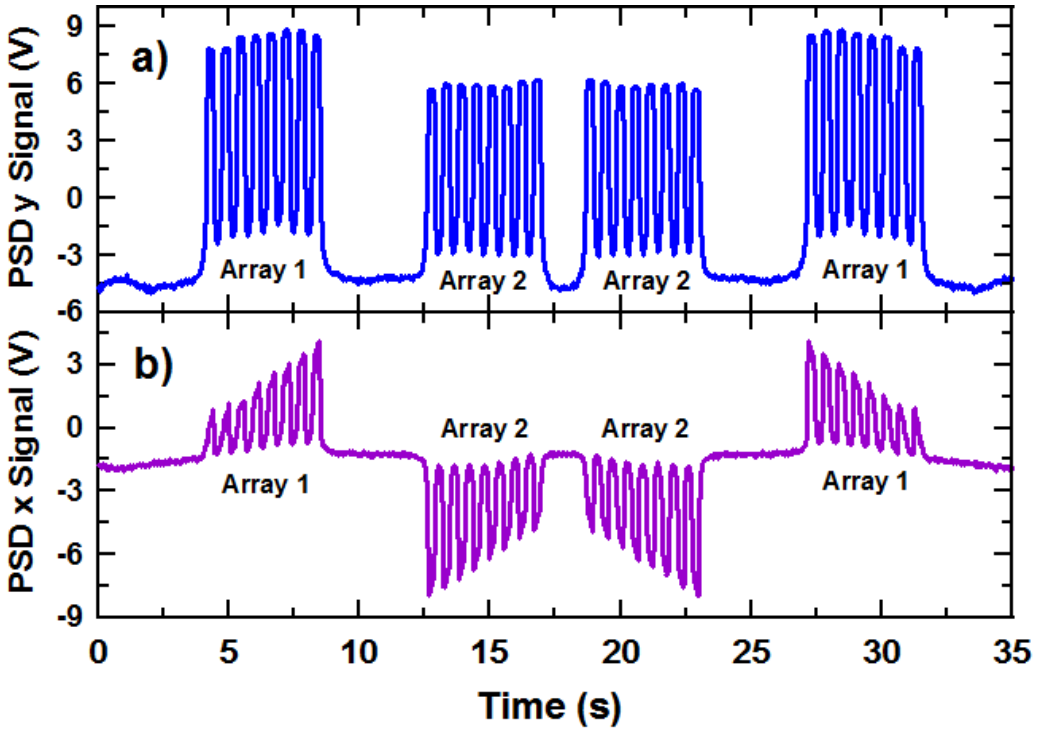

Figure 6.4: Experimental data taken while two gold coated 8-microcantilever arrays were subjected to hot water. a) The y-position as a function of time of the reflected beam on the PSD. b) The x-position as a function of time of the reflected beam on the PSD.

The difficulty in writing this software originated from the fact that the displacement of the optical beam in the *x*-direction and the *y*-signal of the optical beam had to be obtained from two separated data sets originating from two different apparatuses. Once obtained the data needed to be merged together and then folded in order to show the evolution of each peak from the deflection of each microcantilever.

Figure 6.5 shows a screen shot of the software made to analyze our data. The data shown in red on the bottom left illustrates the evolution of eight gold coated microcantilevers

exposed to hot water as a function of time. Hot water causes the microcantilevers to bend as a result of the bi-metallic effect. The data displayed is a superposition of 60 cycles where one cycle represents the motion of the translation stage from left-to-right or from right-to-left. As the experiment progressed, the microcantilevers deflected as they were heated which is illustrated by the increase in the height of each peak. In order to fit the peaks, fitting functions were incorporated into the software. The data on the top right indicates the data (blue dots) collected on the first cycle from one of the microcantilevers. The data can be fitted to a four different types of polynomials or an exponential curve depending on the shape of the peaks. As shown in Figure 6.5, the data from this experiment was well fitted to the exponential curve. Once the proper fitting equation was established, the program processed through each cycles and performs a fit of each peak collected during the experiment. The height of each peak was then saved into a file along with the time at which that peak was recorded. The end result is a data set showing the deflection of each microcantilever as a function of time as shown in Figure 6.6. The data in Figure 6.6 shows how the four microcantilevers reacted the same way to the hot water. The high degree of similarity demonstrated by the eight curves is an indication of the high level of reproducibility we can expect from this system as we begin to apply it to actual sensing experiments. The data analysis program has also been modified to incorporate new features which have become necessary with usage. For example, there is an offset that exists between the left and right motion of the translation stage which is most likely due to the backlash in the screw used to drive the stage. Therefore a function had to be included to adjust the data to make sure that successive peaks overlap

appropriately. Due to thermal noise the data is also found to drift in the *y*-direction. Therefore a routine was included to normalize the data with respect to sections of the data that are fixed in position, for example the data between 0.6 and 0.8 in the data shown in Figure 6.5. In some cases it was necessary to obtain the peak profile collected during a specific cycle. Therefore, a routine was included to store the peak profiles for each individual cycle.

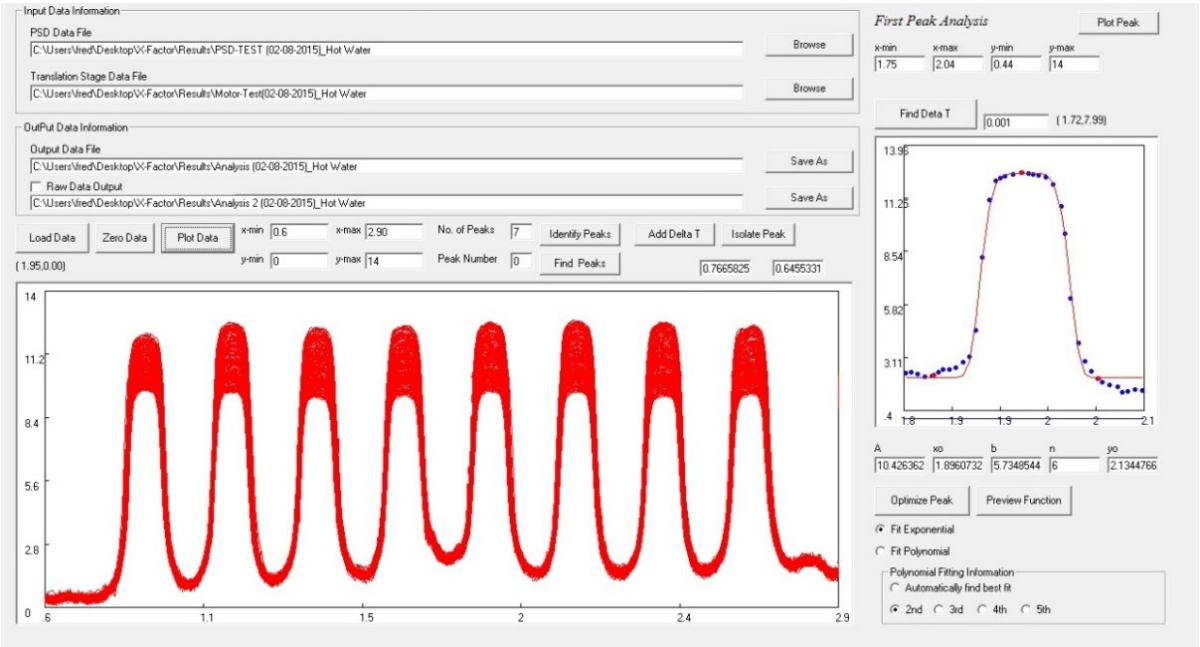

Figure 6.5: Interface of the software used to analyze the data collected by our new microcantilever sensor setup.

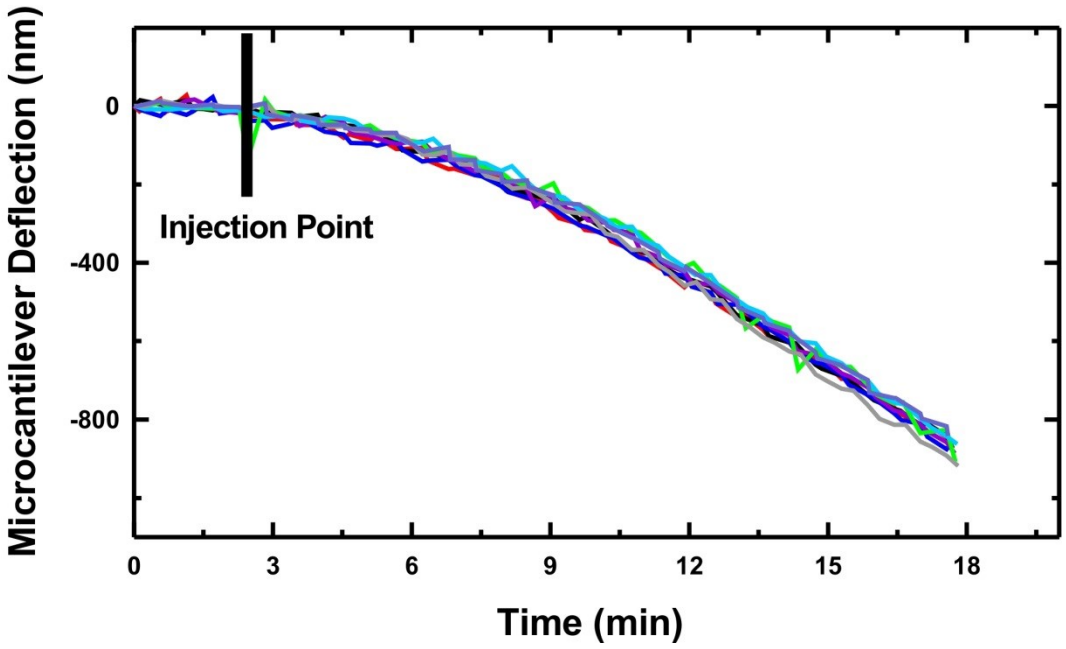

Figure 6.6: The microcantilever deflection as obtained from the analysis of the eight peaks shown in Figure 6.5.

6.3 Functionalization Unit

Since the new system uses two 8-microcantilever probes, it was necessary to develop a system that allows the functionalization of each microcantilever within the array. This design, shown in Figure 6.7, involved the use of an XYZ translation stage in which the microcantilever array is held. This translation stage allows the microcantilevers to be positioned inside microcapillaries tubes which contain the functionalization solution (i.e. calixarene) as shown in Figure 6.8.

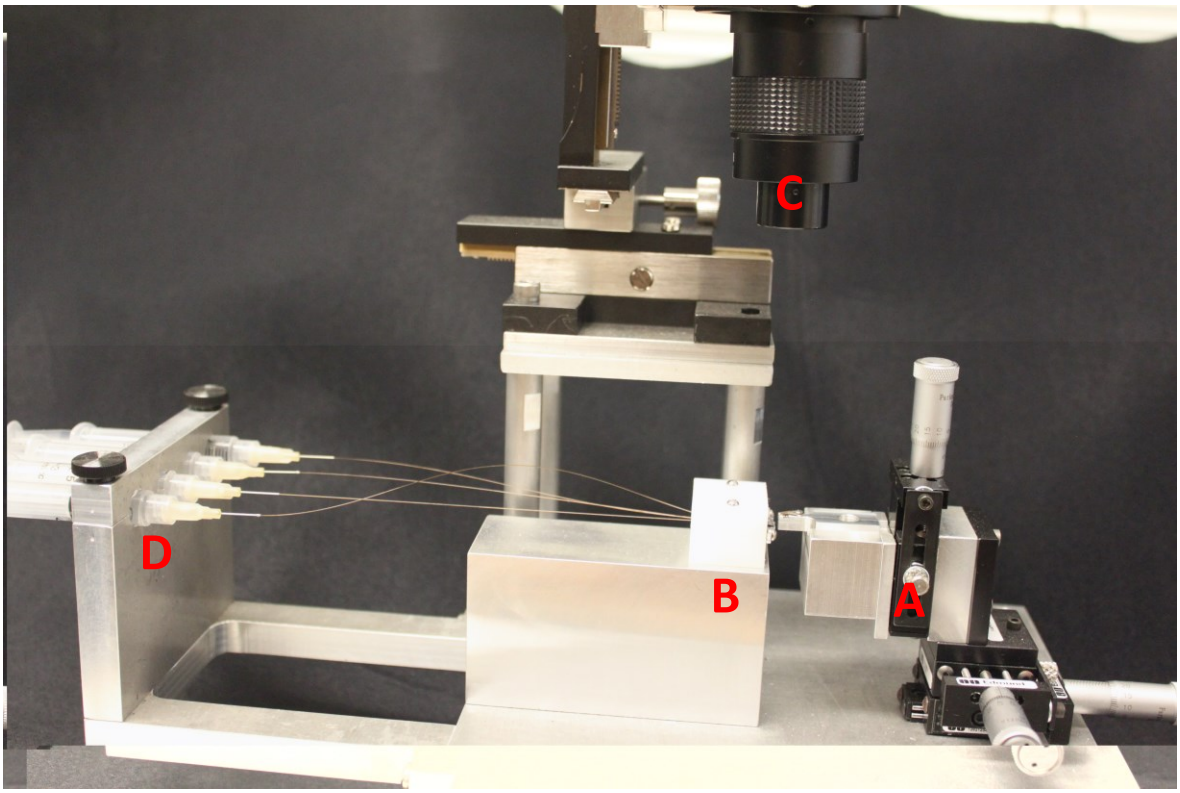

Figure 6.7: A photograph of the functionalization unit. A) an XYZ translation stage to which the microcantilever array is attached. B) micropipettes holder which is attached on the other side to syringes containing the solution to be immobilized. C) an optical microscope to allow the management of microcantilever-micropipettes insertion. D) syringes by which desired solutions are transmitted into the pipettes.

This new developed functionalization unit makes it possible to functionalize the three generations of calixarene on the same microcantilever array which is of fundamental importance to closely study the effect of a certain target ion on all three different calixarene sensing layers.

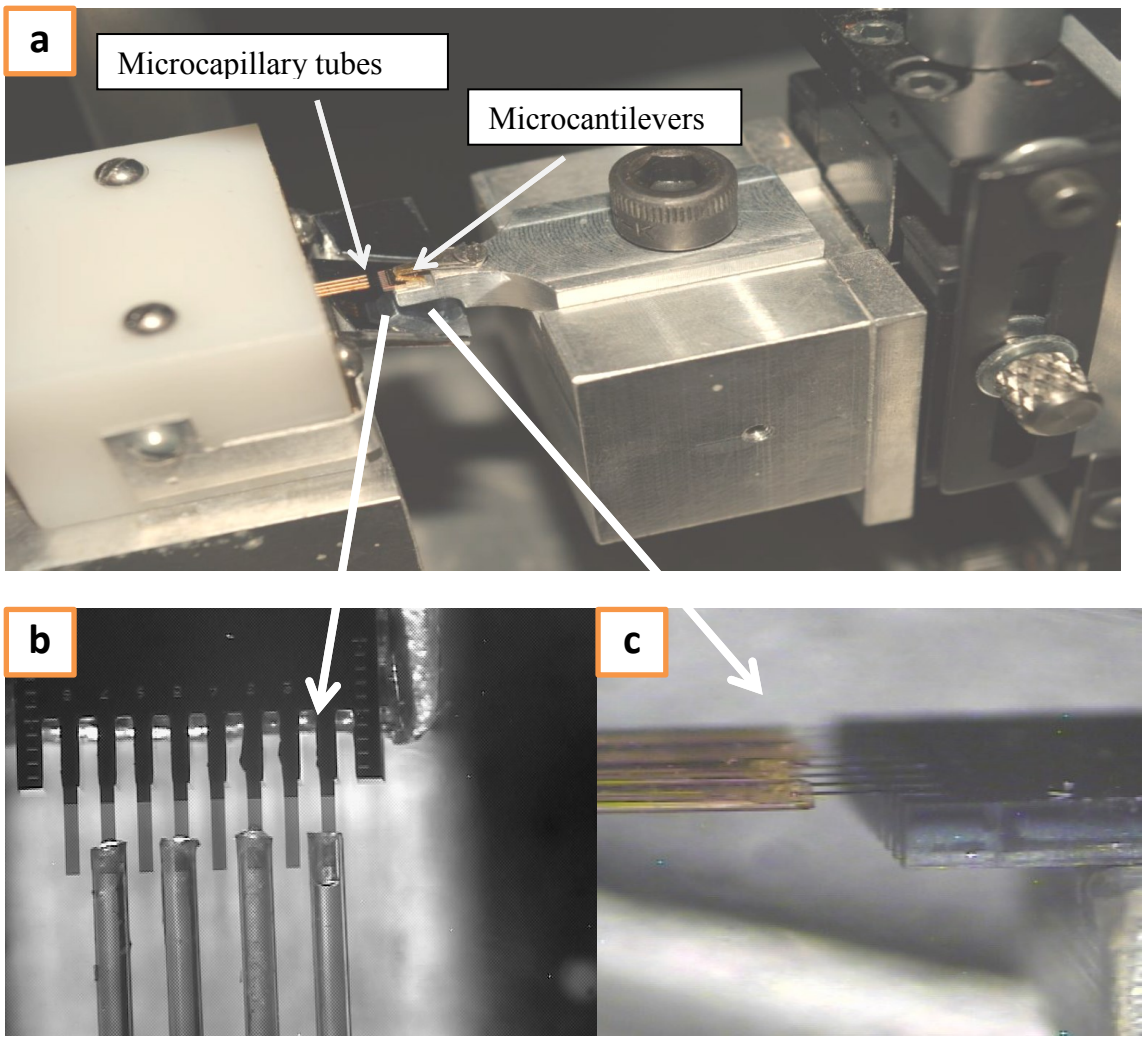

Figure 6.8: (a) A photograph showing the insertion of microcantilevers into the pipettes containing the solution of interest. (b) A top view image taken by a CCD camera which shows the simultaneous functionalization of four microcantilevers in the array. The other four microcantilevers were then re-positioned using the translation stage in order to be inserted into the filled capillary tubes. (c) A side view of microcantilevers inserted into the microcapillaries.

6.4 Experimental Protocol and Functionalization of Microcantilever Array

For the new experimental setup described herein, microcantilevers arrays containing 8 microcantilevers were used. As indicated in table 4.1, two types of microcantilever arrays with similar dimensions but different lengths were used. All microcantilevers used during the course of this work had a thickness of 1 µm.

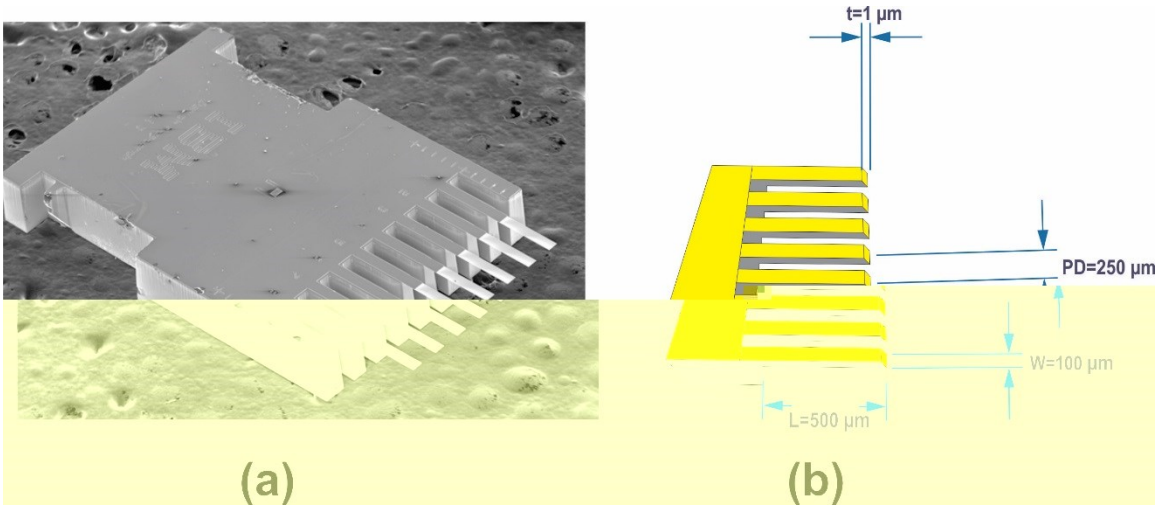

Figure 6.9: (a) A scanning electron microscopy (SEM) image of a microcantilever array comprising eight identical silicon microcantilevers. (b) An illustrative depiction of the dimensions of a microcantilever array (CLA500-010-08). The pitch distance (PD) between microcantilevers with the array is 250 µm.

One of the advantages offered by the new experimental setup described earlier was the possibility of simultaneously testing the response of microcantilevers coated with different sensing and reference layers. This feature is a key to investigating the reliability and accuracy of sensing measurements. The use of the functionalization unit made it possible to simultaneously functionalize four microcantilevers at one time with four different materials. The functionalization process was performed under special care since imprecise positioning of the microcantilevers could easily break them. In order to ensure a precise positioning of the microcantilevers, a ccd camera and three mirrors were used to allow for face and sides of the microcantilevers to be viewed simultaneously. Following the RCA cleaning and gold deposition process described in section 4.5, the microcantilever arrays were transferred into the functionalization unit where they were mounted on a 3D translation stage (see Figure 6.8a). This stage allowed microcantilevers to be precisely positioned and inserted into the capillaries. Fused Silica capillaries, shown in Figure 6.8b, having an inner diameter 150 μm, outer diameter 238 μm and pitch distance 500 μm were filled with the functionalization solution (e.g.: calixarene) by connecting them to syringes. As demonstrated by Figure 6.8, four microcantilevers within the array can be simultaneously functionalized with the desired chemical solution.

After the first four microcantilevers were functionalized, the remaining set of microcantilevers was inserted into capillaries so that all microcantilevers within the array were modified with the desired functionalization solution. Unless otherwise mentioned, three of these tubes were filled with the three calix[4]arene compounds (i.e.: methoxy,

ethoxy and crown) and one tube was filled with decanethiol. Figure 6.10 illustrates the typical scheme used to functionalize the microcantilevers used in sensing experiments. This process also allowed for the *in-situ* functionalization of the reference microcantilever.

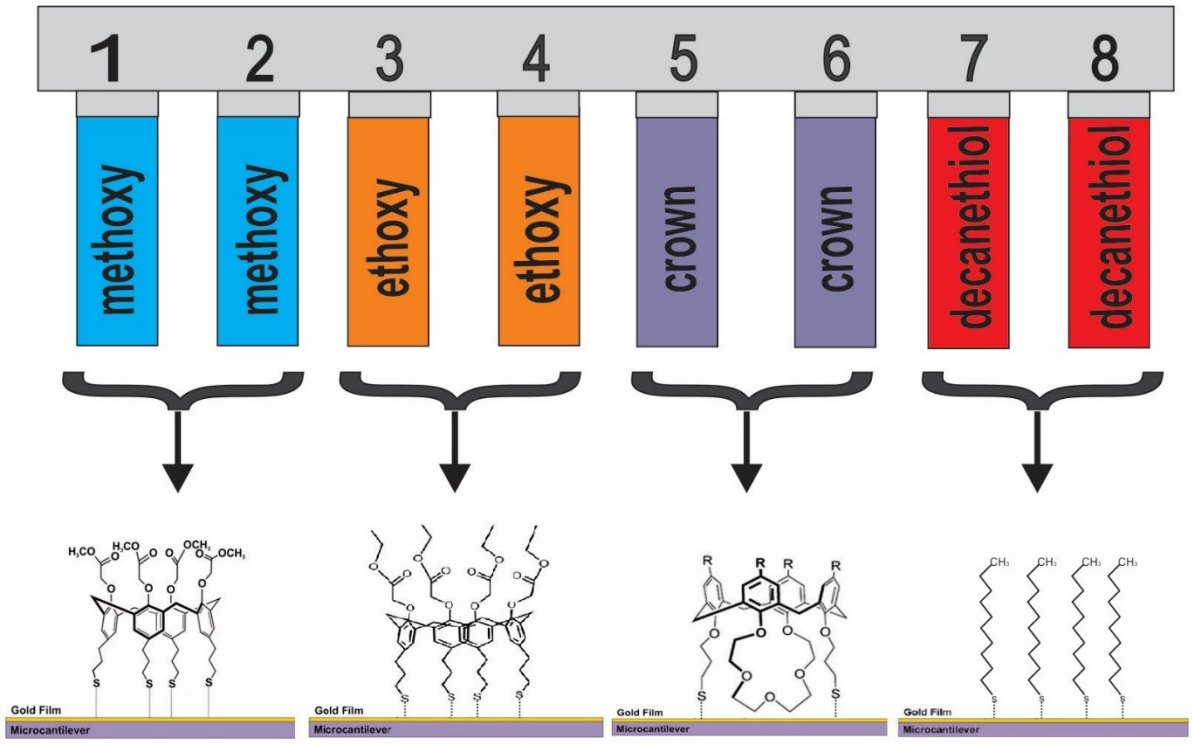

Figure 6.10: Schematic representation of the functionalization scheme used for the microcantilever array. Microcantilevers within the array were functionalized as follows: two microcantilevers functionalized with methoxy calix[4]arene, two microcantilevers were modified with ethoxy calix[4]arene, two microcantilevers were coated with crown calix[4]arene and the other two microcantilevers, assigned as references, were functionalized with decanethiol.

After the microcantilever arrays were functionalized with the proper sensing layers, they were placed into the fluid cell (see Figure 6.2) where they were exposed to aqueous solutions. The experiments were conducted by first flowing research-grade distilled water into the fluid cell to allow the microcantilevers to reach a thermal equilibrium position identified as a steady state baseline of the microcantilever deflection signal. Target solutions of known concentrations prepared using the same grade of water were then allowed into the fluid cell and the response of the microcantilevers was monitored via the optical beam deflection system.

6.4.1 Spring Constant Measurements

Prior to sensing experiments, the spring constant of each microcantilever in the array was measured. As discussed previously, the advancement in microfabrication processes has enabled the production of arrays comprising microcantilevers with relatively similar dimensions and properties. However, variations in the resonance frequency and spring constants in the microcantilevers within the array and/or variation from chip to chip was observed. The spring constant values provided by manufacturer are only nominal values and are specified in a wide range of values. The key parameter primarily responsible for the wide tolerance in spring constant values is the thickness of the microcantilevers. Therefore, measurement of the spring constant of each microcantilever in the array is imperative and thus was performed before each experiment. Using Equations 3.10 and 3.11 (see Chapter 3), the spring constant of the microcantilever can be determined by

measuring its resonance frequency, which was experimentally determined using the tuning feature in our AFM system.

In order to verify the effect of gold coating on the resonant frequency and spring constant of the microcantilevers, the resonant frequency and spring constant of a microcantilever array before and after deposition of gold were measured and presented in Table 6.1. A variation of about 78% in spring constant between bare and Au-coated microcantilevers was observed. The deposition of the Au coating makes a microcantilever heavier and stiffer and thus decreases the resonance frequency and increases the spring constant. Such observations are consistent with the results found by Cleveland *et al.* [160] and Sader *et al.* [197] who monitored the change in spring constant after depositing a gold thin film with a thickness far less than that of the cantilever substrate and observed a clear shift in the spring constant of cantilevers after the addition of gold film layer. The measurements of spring constant values should be performed at all times before experiments in order to allow for quantitative calculation of surface stress which, in turn, provides insight about the difference in responses between individual microcantilevers in the array. Determining the spring constant and surface stress would also allow for comparative studies of cantilever experiments conducted at different times.

Table 6.1: Measurements of frequency and spring constant of 8 microcantilevers within an array before and after deposition of gold. The difference in percentage clearly demonstrates the change in frequency and spring constants of the composite microcantilevers.

Microcantilever Number	Si microcantilevers		Au–coated microcantilevers		Percentage Difference	
	Frequency (KHz)	Spring Constant (N/m)	Frequency (KHz)	Spring Constant (N/m)	Frequency %	Spring Constant %
1	4.64	0.0241	4.35	0.0542	6.45	76.8
2	4.63	0.0239	4.33	0.0519	6.69	73.8
3	4.65	0.0243	4.34	0.0507	6.89	70.4
4	4.66	0.0244	4.38	0.0571	6.19	80.2
5	4.65	0.0243	4.36	0.0546	6.43	76.8
6	4.63	0.0239	4.37	0.0607	5.77	86.9
7	4.62	0.0238	4.35	0.0579	6.02	83.4
8	4.64	0.0241	4.36	0.0564	6.22	80.2
Average	4.64±0.004	0.0241±0.0001	4.35±0.006	0.0554±0.0012	6.33±0.77	78.6±1.8

6.4.2 Quantification of Surface Stress

In order to account for the variability of the spring constant values, the deflection response of each microcantilever in the array was expressed in terms of surface stress. Converting to surface stress makes it possible to compare the response of microcantilevers coated with similar functional layers. According to the derivation outlined in Chapter 2 (see section 2.2), the relationship between the difference in surface stress $\Delta\sigma$, spring constant K_{Spring} and microcantilever deflection δ can be written as:

$$\Delta\sigma = \frac{4L}{3\,(1-v)bt} K_{Spring}\,\delta \tag{6.1}$$

The variables L, b, t and v represent the microcantilever's length, width, thickness and Poisson's ratio respectively. In order to obtain accurate quantitative surface stress measurements, the value of each parameter in the above equation was carefully determined. The spring constant of each microcantilever in the array was obtained as described in the preceding section. The microcantilever deflection was obtained by translating the output voltage of the PSD into a deflection using the OBDS outlined in Chapter 3. With the exception of Poisson's ratio, the measurements of the microcantilever's length, width and thickness were provided by the manufacturer with their associated uncertainties (see table 4.1). For some materials such as silicon nitride, Poisson's ratio has been quoted in the literature in a wide range of values from 0.064 to 0.3 [197,198]. Silicon microcantilevers, which were used in this work, have however

well-known elastic properties such as Poisson's ratio and thus the overall uncertainty in surface stress measurements can be reduced. Poisson's ratio was taken to be 0.25±0.02 which is the standard value for silicon microcantilevers [199].

Chapter 7 Sensing measurements of Calix[4]arene using array-based microcantilevers

In this chapter, the results obtained with the new 16-microcantilever array system using calix[4]arene-functionalized microcantilevers to detect specific target ions are reported and discussed. Results presented in chapter 5, conducted using the two single-cantilever system, confirmed the sensitivity and affinity of calix[4]arene-functionalized microcantilevers towards metal ions in solution. The reason to repeat results from chapter 5 was to test the capability of the new system to reproduce previous results and to validate the calibration procedures discussed in the preceding chapter. In addition, we will exploit the ability of the 16 microcantilevers for performing a parallel investigation of multiple calix[4]arenes and reference layers at the same time. The simultaneous investigation of the binding capabilities of multiple calix[4]arene layers towards metal ions significantly increases the reliability and accuracy of our experimental results. Section 7.1 of this chapter presents the experimental results conducted to test the new experimental system. In section 7.2, surface stress measurements of the 16 microcantilever sensors functionalized with different calix[4]arene sensing layers are presented and discussed. Finally, a summary about the main experimental findings obtained in this chapter and a comparison with results obtained in chapter 5 is given in section 7.3.

7.1 Testing of the System

In order to assess the performance of the newly developed 16-microcantilever system, experiments were conducted using methoxy calix[4]arene-functionalized microcantilevers and Ca^{2+} ions. The springs constant of two Au-coated microcantilever arrays were measured and are presented in table 7.1. The spring constant of each microcantilever was substituted into Equation 6.1 to obtain the surface stress signal. According to this table, the percentage variation of each microcantilever, calculated by finding the percentage difference between the average of all spring constants in the array and each individual spring constant, ranged from 2-9%. It is obvious from this table that there is a variation in the spring constant of microcantilevers in the same arrays. Such variation was also reported by Holbery and Eden [200], who found a spring constant variation of approximately 30% for microcantilevers in the same array. These variations were attributed to the difference in thickness and/or material properties of microcantilevers in the same array.

Four microcantilevers in each array (microcantilevers 1,3,5,7) were functionalized with a 1.0 μM solution of methoxy calix[4]arene while decanethiol was immobilized on the other microcantilevers (microcantilevers 2,4,6,8), as shown in Figure 7.1. The functionalized microcantilever arrays were then equilibrated in the fluid cell by injecting distilled water followed by the introduction of a solution containing Ca^{2+} ions.

Table 7.1: Spring constant values of two Au-coated microcantilever arrays. The last two columns show the percentage difference in spring constant for microcantilevers in the first and second array.

Microcantilever Number	Array 1	Array 2	Difference (%)	
	Spring Constant (N/m)	Spring Constant (N/m)	Spring Constant of Array 1	Spring Constant of Array 2
1	0.0542	0.0457	2.18	1.93
2	0.0519	0.0451	6.52	3.25
3	0.0507	0.0474	8.85	1.71
4	0.0571	0.0477	3.02	2.48
5	0.0546	0.0442	1.45	5.16
6	0.0607	0.0503	9.13	7.81
7	0.0579	0.0481	4.41	3.38
8	0.0564	0.0439	1.78	5.84
Average	0.0554±0.0012	0.0465±0.0008	4.67±1.11	3.95±0.76

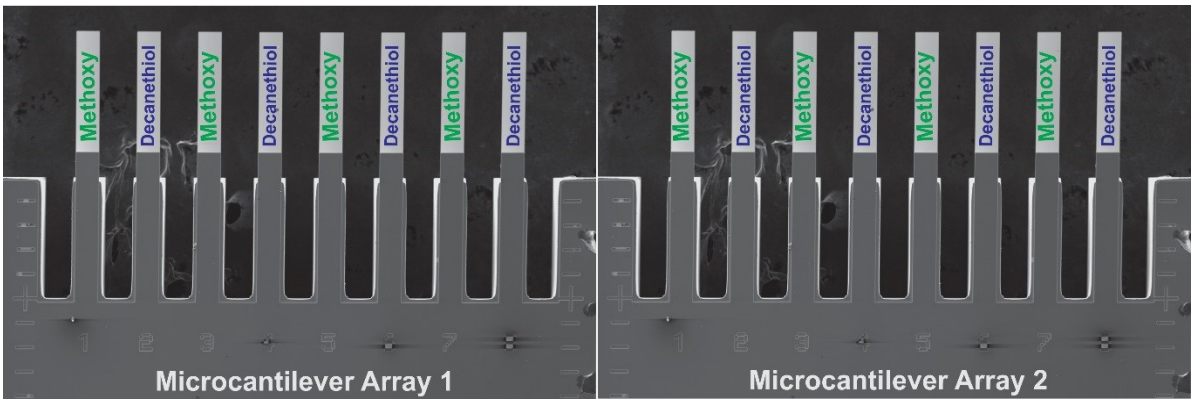

Figure 7.1: The functionalization scheme of the two microcantilever arrays used for testing the new experimental system. Four microcantilevers in each array were functionalized with methoxy calix[4]arene sensing layers while the remaining four were coated with decanethiol, to serve as reference microcantilevers.

Figure 7.2a shows the surface stress profile of the 16 functionalized microcantilevers to the injection of a 10^{-6} M solution of $CaCl_2$. As revealed in this figure, the active microcantilevers, displayed by red curves, deflected as a result of the interactions between calix[4]arene and the target ions which induced a surface stress on the microcantilever surface causing the microcantilever deflection. On the other hand, the reference microcantilevers (displayed in brown curves) which were coated with decanethiols showed a negligible response. Figure 7.2b displays the individual surface stress change at 35 min of each microcantilever in the array caused by the binding between methoxy calix[4]arenes and Ca^{2+} ions. Since each array contained four active and reference microcantilevers, the differential signal was obtained by subtracting the reference surface stress signal from the active microcantilever measurements. The resulting data represent the specific interactions between the Ca^{2+} ions and the

calix[4]arenes. As demonstrated in Figure 7.2b, the magnitude of the differential surfaces stress of each microcantilever was comparable, indicating the excellent reproducibility of the functionalized microcantilevers within the array. Since the surface stress is a function of spring constant (see Equation 6.1), the very small variations observed in the microcantilever surface stress can be attributed to the small difference in spring constant values, which were reported in table 7.1.

It was also important to ensure that the new microcantilever system can be effective in distinguishing the microcantilever deflection caused by varying the target concentration. To examine the effect of the target concentration, two microcantilever arrays coated similarly to the previous case were subjected to a 10^{-8} M aqueous solution of $CaCl_2$. As displayed in Figure 7.2a, the surface stress change resulting from the injection of the lower concentration of $CaCl_2$ could be clearly distinguished, where the methoxy calix[4]arenes-modified microcantilevers suffered a smaller surface stress than those exposed to 10^{-6} M solution of $CaCl_2$. The data shown in Figure 7.2a is consistent with the data obtained from the single microcantilever system which showed that the microcantilever deflection increased when increasing the target concentration (see Figures 5.9 and 5.10). Despite the fact that we did not have the means to measure the spring constant when experiments reported in Chapter 5 were conducted, the curve profiles of Figures 5.9, 5.10 and 7.2 are qualitatively similar.

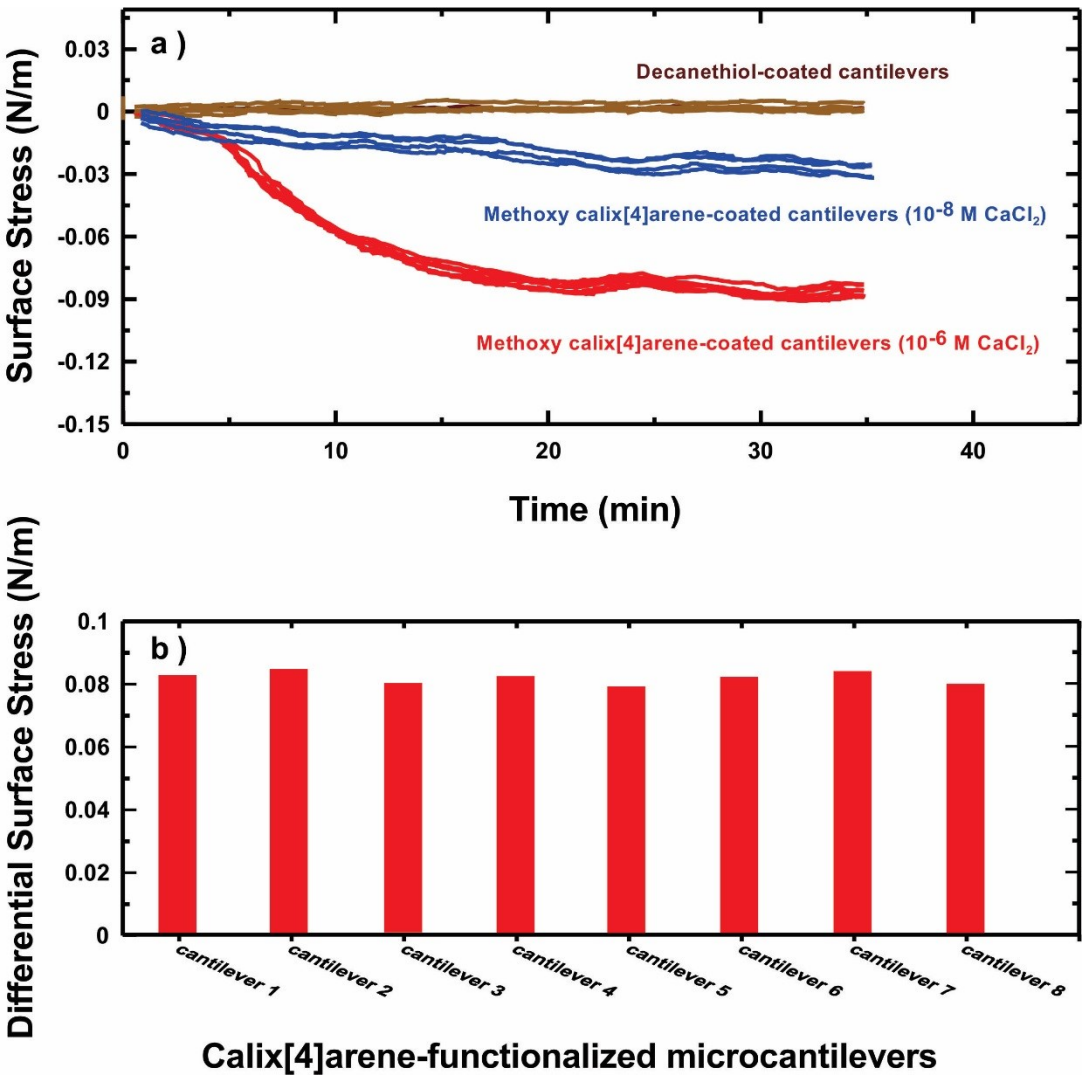

Figure 7.2: (a) The surface stress change of each microcantilever in the array to the injection of 10^{-6} M (red) and 10^{-8} M (blue) aqueous solution of $CaCl_2$. (b) The differential surface stress signal for each microcantilever in the array, representing the specific binding between the calix[4]arene and the Ca^{2+} ions.

It can be stated that based on these preliminary results that the new experimental set up was capable of successfully transducing the binding events between the calix[4]arenes-modified microcantilevers and Ca^{2+} ions into a readable deflection and surface stress signals.

7.2 The sensitivity of methoxy, ethoxy and crown calix[4]arene - functionalized microcantilevers towards specific metal ions

Taking advantage of the possibility of functionalizing multiple sensing layers on microcantilevers in the same array, experiments were conducted so as to investigate the simultaneous response of all three calix[4]arene compounds to the injection of specific metal ions. In this section, three different experiments involving the use of 6 microcantilever arrays were conducted. In all of these experiments, the microcantilevers were functionalized similarly as described in Chapter 6 (see Figure 6.10). For each experiment where two arrays were used, the spring constant and deflection response of each microcantilever were used in order to obtain quantitative surface stress measurements. The three metal ions that were used in these experiments were Ca^{2+}, Sr^{2+}, and Cs^{+}, respectively. The reason of selecting these ions was because they had the same chloride counterion and also their binding abilities with calix[4]arene layers were confirmed in our previous studies with the single microcantilever system. In particular, the binding reaction of the calix[4]arene sensing layers toward Sr^{2+} has been given very

little consideration, despite its importance in many industrial and commercial applications [201].

Figure 7.3a shows the surface stress variation of the 16 functionalized microcantilevers as a function of time in response to the introduction of Ca^{2+} ions. The four methoxy calix[4]arene-coated microcantilevers, shown by green curves, generated the largest surface stress over ethoxy (red curves) and crown (purple curves) calix[4]arene-coated microcantilevers. The sensitivity shown by ethoxy calix[4]arene-coated microcantilevers was approximately 26% lower than that exhibited by methoxy but larger than that of crown calix[4]arene by about 75 %. Reference microcantilevers, shown by pink curves in Figure 7.3a, were not however found to be responsive to the introduction of Ca^{2+} ions, assuring that the response of calix[4]arene-coated microcantilevers was predominantly caused by the binding with Ca^{2+} ions. In order to compare the response of microcantilevers modified with different calix[4]arene sensing layers, the average end surface stress at 30 mins for identically functionalized microcantilevers was determined. The differential surface stress signal which reflects the specific binding events between the target ions and calix[4]arene was calculated by subtracting the averaged reference signal from the averaged active signals of the calix[4]arene-modified microcantilevers. Figure 7.3b illustrates a comparison between the differential surface stress signals of the three different calix[4]arenes coated on 12 different microcantilevers, along with the associated uncertainty. The standard deviation, which was calculated as described in section 5.2, is represented by the error bars.

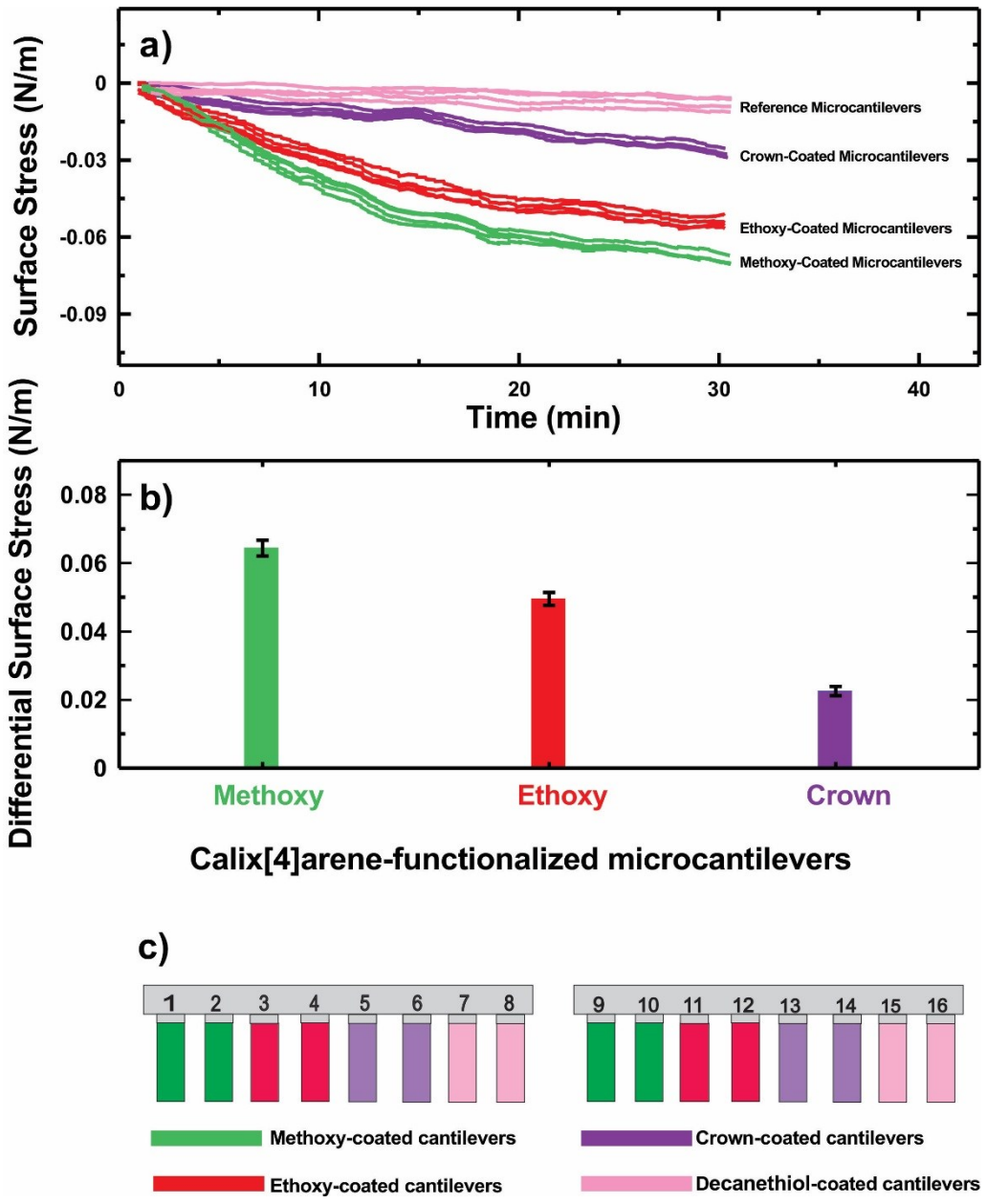

Figure 7.3: (a) The surface stress changes in methoxy (green), ethoxy (red) and crown (purple) calix[4]arene-coated microcantilevers in response to 10^{-6} M aqueous solution of $CaCl_2$. (b) The differential signals representing the net surface stress caused by the binding between calix[4]arenes and Ca^{2+} ions, along with their associated errors. (c) Functionalization scheme of microcantilever arrays used in this experiment.

The differential surface stress values for methoxy, ethoxy and crown calix[4]arenes were found to be approximately 0.065±0.002 N/m, 0.049±0.002 N/m and 0.022±0.001 N/m respectively. These small uncertainties which range from 4% to 6% indicate the excellent reproducibility obtained with the new microcantilever array system.

The large surface stress difference seen between methoxy and crown calix[4]arenes in Figure 7.3b are in qualitative agreement with the results obtained with the single microcantilever system (see Figures 5.12 and 5.16). The differential surface stress shown by methoxy calix[4]arene towards the Ca^{2+} ions was the highest of the three sensing layers, and was approximately 25% greater than that of ethoxy calix[4]arene. On the other hand, both methoxy and ethoxy were much more sensitive towards Ca^{2+} than the crown which showed differential surface stress roughly 45% and 70 % lower than ethoxy and methoxy calix[4]arenes respectively. The high sensitivity obtained with ethoxy is not in fact surprising as ethoxy shares the same structure (i.e.: binding site) as methoxy except that the lower rim of methoxy (OCH_3) was replaced with ethoxy (OCH_2CH_3) (see Figures 4.3 and 4.6). Complexation studies performed using NMR spectroscopy, conducted by Dr. Paris Georghiou's group in the Chemistry Department, of methoxy and ethoxy calix[4]arenes with 14 different metal ions also revealed that these two calix[4]arenes bind selectively to Ca^{2+} ions [202]. In these experiments, stock solutions of calix[4]arenes and metal ions were prepared in a 4:1 CD_3OD:$CDCL_3$ solvent mixture. Metal ion solutions were then added to the calix[4]arene solution and the NMR spectra was recorded after each addition. The complexation constants [K] which are indicative of

the binding strength between the metal ion and calix[4]arene were then determined. Based on these results, it was surmised that methoxy and ethoxy calix[4]arenes would also have similar binding affinity towards other target ions. As will be shown later (see Figure 7.4), this prediction was however incorrect for when Sr^{2+}. The binding affinity of ethoxy calix[4]arene towards Sr^{2+} ions was found to be significantly larger than that exhibited by methoxy calix[4]arene. It was in fact found by the NMR studies, mentioned above, that for some metal ions the binding affinity of ethoxy calix[4]arene was approximately 3-fold higher than methoxy calix[4]arene [202]. Accordingly, both NMR spectroscopy and microcantilever sensors results, although conducted under different experimental conditions (i.e.: solvent system), suggest that despite the slight difference in the structures between methoxy and ethoxy calix[4]arenes, their sensitive recognition towards target ions is not necessarily the same. According to the discussion provided in chapter 5, the reaction mechanism of calix[4]arene sensing layers can be affected by other factors other than the cavity size and ionic radii of target ions, which could possibly explain the difference seen between methoxy and ethoxy towards Sr^{2+}.

In a subsequent experiment, two Au-coated microcantilevers were functionalized in the same manner as the previous arrays. In this experiment, the functionalized arrays were subjected to 10^{-6} M aqueous solution of $SrCl_2$. In contrast to the results shown in Figure 7.3 where methoxy calix[4]arene-coated microcantilevers showed the highest sensitivity towards Ca^{2+} ions, ethoxy calix[4]arene-coated microcantilevers induced the largest surface stress towards Sr^{2+} over the surface stress observed with both methoxy and crown

calix[4]arenes. As shown in Figure 7.4a, the four microcantilevers coated with ethoxy calix[4]arenes, represented by the red curves, consistently experienced larger surface stress while the other microcantilevers responded with smaller end surface stress signals. The pink curves in Figure 7.4a show the response of the decanethiol-coated microcantilevers (i.e.: reference microcantilevers), displaying marginal surface stress changes to Sr^{2+} solution. The differential signal of the average surface stress changes of the four curves for each calix[4]arenes sensing layer with the corresponding standard deviation (i.e.: error bars) is plotted in Figure 7.4b. As discussed earlier, it was initially expected, based on the results shown in Figure 7.3, that methoxy and ethoxy-coated microcantilevers would be comparably responsive to all target ions. However this was not observed in the case of Sr^{2+} ions where the end surface stress variation of microcantilevers coated with methoxy calix[4]arene was smaller than that of ethoxy. The former result is in fact in close agreement with the result reported in Figure 5.11, where it was shown that the deflection response of methoxy calix[4]arene to Sr^{2+} ion was very small. In an analogous manner, the surface stress changes of methoxy calix[4]arene-coated microcantilevers towards Sr^{2+} ion were found to be small. The difference in the surface stress response observed between methoxy and ethoxy towards Sr^{2+} raise an important aspect of calix[4]arene sensing layers, which is the lack of selectivity. This aspect is discussed in further detail in section 7.3 of this chapter.

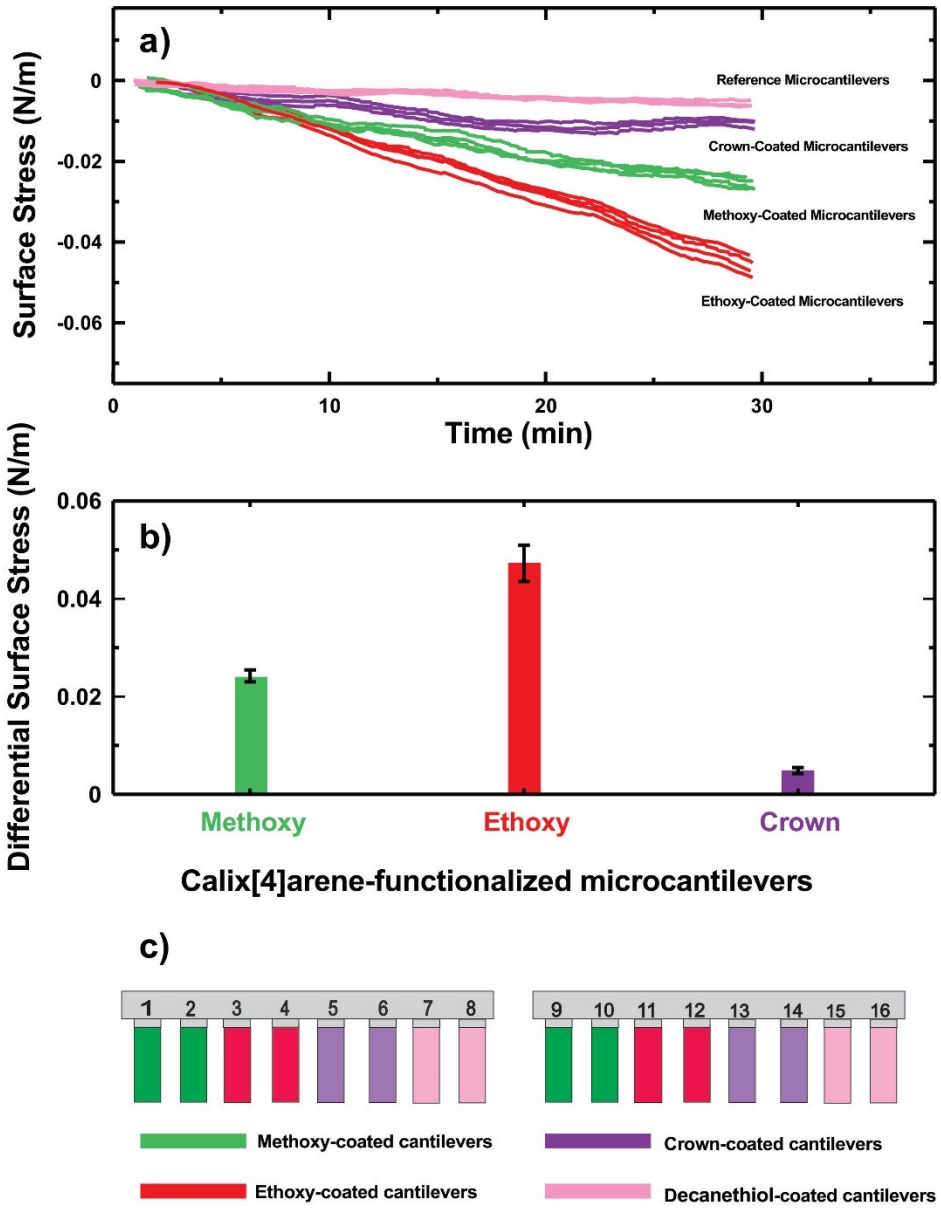

Figure 7.4: (a) The surface stress changes in methoxy (green), ethoxy (red) and crown (purple) calix[4]arene-coated microcantilevers in response to 10^{-6} M aqueous solution of $SrCl_2$. (b) The differential surface stress signals for the three calix[4]arene sensing layers. Each error bar represents the standard deviation obtained from each four identically coated microcantilevers. (c) Functionalization scheme of microcantilever array used in this experiment.

Furthermore, one of the intriguing observations from the data shown in Figure 7.4 is the large variation in the surface stress magnitude, as seen by the error bars, of the ethoxy calix[4]arene-coated microcantilevers, compared to other curves in the same plot where the responses of microcantilevers were very consistent and close to each other. The uncertainty in surface stress signal of ethoxy calix[4]arene-coated microcantilevers was found to be approximately 10% in contrast to that of methoxy which was calculated to be approximately 5%. This large variation was expected to be caused by the percentage difference in the spring constant values of ethoxy calix[4]arene-coated microcantilevers (microcantilevers 3,4,11,12). Although ethoxy calix[4]arene-coated microcantilevers were found to have a larger difference in their spring constant values that other microcantilevers, other factors may also contribute to such difference in microcantilever curves coated with the same sensing layer. We speculate that the difference in the response of identically functionalized microcantilevers can, besides the variation in spring constant values, also be caused by the way in which the target solution is presented to the microcantilevers in the fluid cell. As mentioned previously, fluid dynamics studies were conducted on the single microcantilever cell where the rate of detection of each microcantilever in the cell was determined. For the fluid cell used in the new experimental setup where fluid follows a linear path, fluid dynamics studies are needed in order to understand how particles move within the new experimental fluid cell. These studies should ultimately allow to correlate the surface stress changes of each individual microcantilever in the array with its rate of detection for target analytes.

An experiment was subsequently conducted to investigate the sensitivity of the three calix[4]arene sensing layers towards Cs^+ ions. Two Au-coated microcantilever arrays, prepared similarly as previous arrays, were subjected to an aqueous 10^{-6} M solution of CsCl. The response of the 16 functionalized microcantilevers within the array is shown in Figure 7.5a. The differential surface stress (shown in Figure 7.5b) of the functionalized microcantilevers exposed to aqueous 10^{-6} M solution of CsCl demonstrated that crown calix[4]arene was more receptive to Cs^+ than methoxy and ethoxy. The reliability and reproducibility of the surface stress responses of functionalized microcantilevers were also demonstrated in Figure 7.5b by the small magnitude of the uncertainty values illustrated by the error bars. As with the previous plot, uncertainties in the end surface stress change observed with the curves in Figure 7.5a (6.21%, 6.46% and 7.01% for crown, ethoxy and methoxy calix[4]arenes, respectively), although being small, show the need of considering the motion of particles inside the fluid cell. It is also noteworthy to mention that bending curves produced by crown and methoxy calix[4]arene sensing layers in response to the introduction of Cs^+ ions were in excellent qualitative agreement with the results obtained from the single microcantilever system which were shown in Figures 5.12 and 5.16.

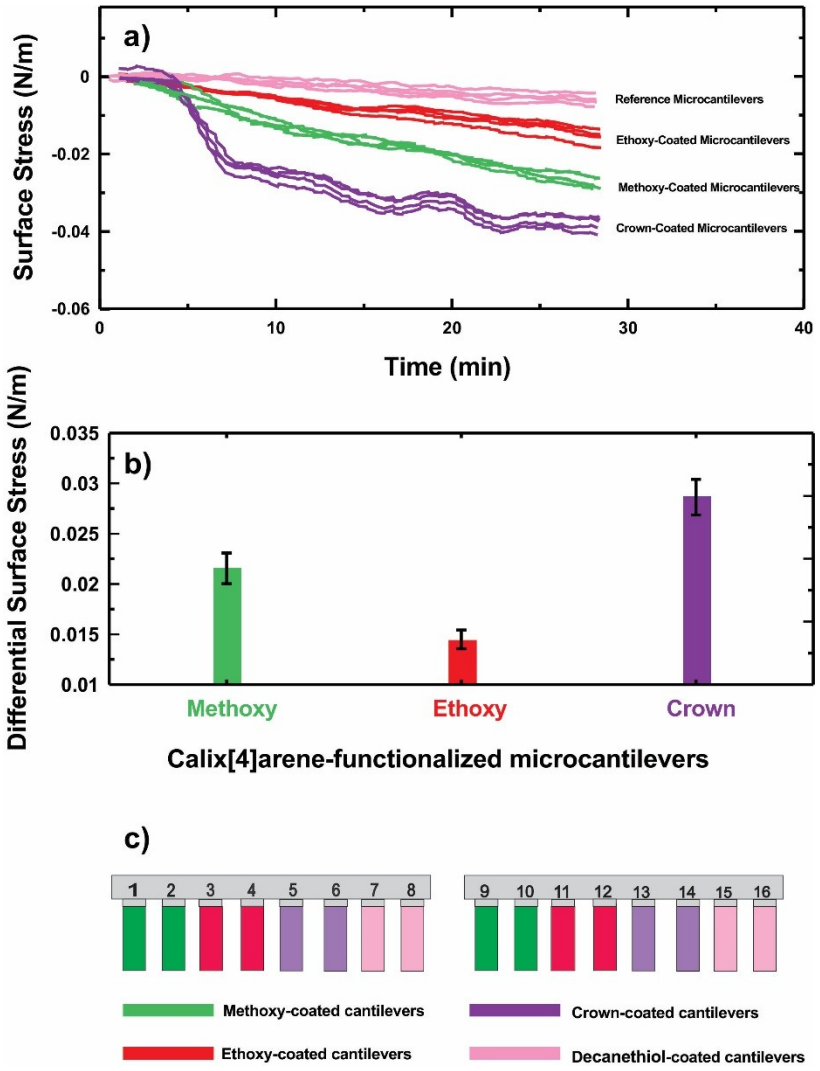

Figure 7.5: (a) The surface stress changes in methoxy (green), ethoxy (red) and crown (purple) calix[4]arene-coated microcantilevers in response to 10^{-6} M aqueous solution of CsCl. (b) The differential surface stress signals plotted as a function of the three calix[4]arene compounds. Each error bar corresponds to the standard deviation associated with the surface stress change of four microcantilevers coated with the same sensing layer. (c) Functionalization scheme of microcantilever array used in this experiment.

7.3 Summary

Investigating the capability of the newly developed 16-microcantilever system to recognize the interaction events between the three calix[4]arene compounds and selected metal ions was the main focus of the present chapter. The new experimental system was first tested by monitoring the response of methoxy calix[4]arene-coated microcantilevers to the introduction of Ca^{2+} solutions. It was also demonstrated that by using the new microcantilever array system it was feasible to simultaneously examine the sensitivity of methoxy, ethoxy and crown calix[4]arene-coated microcantilevers towards selected metal ions. The feature of parallel monitoring of multiple sensing layers can save time and efforts considerably. More importantly, the simultaneous monitoring allows the use of reference microcantilevers within the same array leading to accurate differential deflection signals. One of the important issues that was addressed by the experimental results conducted with the new experimental system was the possibility of evaluating the reproducibility of the data. The reproducibility has been one of the factors limiting the performance and viability of the microcantilever sensor technology [203]. It can be claimed that based on the experimental findings reported in this chapter that the use of microcantilever arrays can improve the overall reliability of microcantilever sensors.

One of the remarkable findings found was the variation of spring constant values of microcantilevers in the same array. The variation in spring constant was believed to be one of the causes behind the difference in surface stress signals between microcantilevers coated with the same sensing layer.

It was also shown in this chapter that methoxy, ethoxy and crown calix[4]arene sensing layers have high binding affinity for Ca^{2+}, Sr^{2+} and Cs^{+} respectively. Despite the high sensitivity of these calix[4]arene layers, the selectivity towards specific target ions was poor. As shown by all results reported in this chapter and in chapter 5, each calix[4]arene sensing layer has a definite preference for a particular target ion, but also was found to bind, although to a lesser extent, to other ionic species. This lack of selectivity makes the use of these particular calix[4]arenes limiting as chemical sensors on their own as it is impossible to determine whether or not a small amount of, for example $CaCl_2$, can be detected in the presence of, for example, Sr^{2+} ions. This obstacle however, can, in principle, be overcome by incorporating different podand groups that bind more selectively with cations of choice [128, 204].

Hence we conclude that the inherent stability of calixarene-based receptors and their apparent sensitivity makes such molecules potentially significant receptive layers if properly functionalized to eliminate their lack of selectivity.

Chapter 8 Conclusion and Future Prospects

8.1 Summary

One of the primary objectives of this thesis was to investigate the binding capabilities of three new bimodal calix[4]arenes sensing layers (methoxy, ethoxy and crown) immobilized on microcantilever sensors towards selected metal ions. The second primary objective of this work was the development of a new experimental sensing platform where the response of 16-microcantilevers can be simultaneously monitored. In this thesis, microcantilever sensors were, for the first time, used to characterize and probe the interactions between thioacetate-bearing calix[4]arenes and various metal ions where both the effect of the cations and their counterion on these interactions were investigated.

Results presented in Part I of this thesis showed that thioacetate-modified calix[4]arenes form well-ordered SAMs onto the Au surface as was characterized using the STM. Results in Part I also showed that cleaning method, incubation time and the thickness of gold film play a key role in affecting the sensitivity of microcantilever sensors and hence need to be optimized before conducting sensing experiments. In Part II of this thesis, we have shown how the new microcantilever array experimental system was designed, constructed and commissioned. We have also discussed the development of the three VB softwares used to monitor the motion of the translation stage, collect the data from the 2D

PSD and analyze the output data. Part II also discussed the results that show the high degree of reproducibility we have come to obtain with the new experimental system.

The experimental findings presented herein which were conducted in both experimental systems have ascertained the capability of calix[4]arene-modified microcantilevers of detecting the presence of selected metal ions in solution. Results obtained from both experimental sensing platforms used in this work showed that methoxy calix[4]arenes-functionalized microcantilevers were capable of detecting Ca^{2+} ions in aqueous solutions of $CaCl_2$ at concentrations as low as 10^{-12} M, which is sufficiently low for most applications. The methoxy calix[4]arene sensing layer also showed a definite preference towards the binding with Ca^{2+} ions over other ionic species such as Mg^{2+} and Sr^{2+}. On the other hand, ethoxy calix[4]arene microcantilevers showed higher sensitivity to aqueous Sr^{2+} and to a lesser-extent to Ca^{2+} and a negligible response to Cs^{+}. Microcantilevers functionalized with crown calix[4]arenes were found to preferentially bind with Cs^{+} over other ions tested such as Ca^{2+}, Rb^{+} and K^{+}. The testing of various metal ions from the same group and from other groups in the period table was also paralleled by investigating the effect of their counteranion on the microcantilever response. It was found that the role of the counteranion in the binding between calix[4]arene-modified microcantilevers and cations cannot be neglected and thus the deflection response of these modified microcantilevers should be attributed to the target ion as a whole instead of assuming the effect of only the presence of the cation or anion. Such studies aimed at providing a better understanding about the mechanism that drives the binding interactions of calixarenes

with target ions which in turn causes the formation of surface stress in the microcantilever. Despite their lack of selectivity, the structure of calix[4]arenes have made them potential host platforms for the sensitive binding with a variety of ion guests.

Lastly, it is worthwhile to state that significant steps have been taken in this work towards our long term goal of developing a portable device for making measurements of heavy metals in fresh water. In this work we showed that calixarenes are excellent foundation molecules for constructing sensing layers for cantilever sensors. Although the calixarenes investigated here were not found to be selective enough to be used as sensing layers, they have given great insight in their host/guest binding mechanism and more importantly point the way to necessary future changes that need to be implemented and effectuated in order to reach our long term goal.

8.2 Future work

As was shown by the results in this thesis, all three calix[4]arene sensing layers exhibited high sensitivity to specific metal ions but were also responsive to other ionic species. This was most likely due to the nature of the binding mechanism where the calix[4]arene cavity can be suitable to more than one metal ion. In order for calix[4]arene-functionalized microcantilevers to be used for practical and selective detection of metal ions in fresh-water environments, calix[4]arenes need to be developed with more selective binding groups. It has been reported that one way of improving calixarene

selectivity can be made by fine-tuning the atomic arrangement of the binding groups to be suitable for optimum dimensions of the target ions of interest [203, 205].

An important future recommendation is to make further investigations into the effect of the gold thickness on the microcantilever sensitivity. In this work we have addressed the role of the varying gold film thicknesses on the microcantilever sensitivity. The associated RMS roughness value was also calculated for each thickness. RMS roughness values alone do not however provide a conclusive characterization of the surface features. Therefore, efforts are needed to identify a definitive relationship between the role of gold nanostructure and the surface roughness on the microcantilever sensitivity.

One of the future considerations for this work is to develop a new functionalization unit to allow 8 microcantilevers be simultaneously modified. This development would help in shortening the time required for microcantilever surface modification and can reduce the potential effect of air contaminants.

The features offered by microcantilever arrays such as the high sensitivity, the possibility of measuring the response of active and reference sensing layers simultaneously, and fast response time could significantly aid the advancement towards the viability and commercialization of microcantilever technology. Nevertheless, further efforts are still to be made in order to optimize the performance of microcantilever sensors. One of these efforts is to gain a better understanding about the origin and mechanism of surface stress

due to receptor-target interactions. In addition, tackling and understanding the equilibrium state issue which was partially addressed in this thesis is also significant for the successful future employment of microcantilever sensors in practical applications. Furthermore, one of the suggestions that can be made to develop a better understanding of the performance of microcantilever arrays is to conduct a systematic study of the variation of spring constant. It will also be helpful to investigate the effect of the gold film thickness on the spring constant of the microcantilever. Finding the gold thickness that has a minimal effect on the spring constant of the microcantilever is also important for improving the microcantilever performance. Another possible future work is to also use arrays consisting of microcantilevers with different spring constants. Monitoring the response of identically functionalized microcantilevers with different spring constants can also allow for a larger range of target concentrations to be detected.

One important potential future work is to conduct fluid dynamics simulations on the motion of particles within the 16-microcantilever sensor cell. This step is critical especially for linear systems where fluid follows a linear path as they move in the sensor cell. Understanding the distribution of particulates within the sensor cell can help to improve the rate of particle detection and the overall sensitivity of microcantilevers.

Bibliography

1. Oehme, F. W. (1978). Toxicity of heavy metals in the environment. 1. 2. *Marcel Dekker, Inc*.
2. Athar, M., & Vohora, S. B. (1995). Heavy metals and environment. *New Age International*.
3. Förstner, U., & Wittmann, G. T. (2012). Metal pollution in the aquatic environment. *Springer Science & Business Media.*
4. Bradl, H. (Ed.). (2005). Heavy metals in the environment: origin, interaction and remediation: origin, interaction and remediation (Vol. 6). *Academic Press*.
5. Duruibe, J. O., Ogwuegbu, M. O. C., & Egwurugwu, J. N. (2007). Heavy metal pollution and human biotoxic effects. *International Journal of Physical Sciences*, *2*(5), 112-118.
6. Sarkar, B. (2002). Heavy metals in the environment. *CRC Press.*
7. Abollino, O., Aceto, M., Malandrino, M., Mentasti, E., Sarzanini, C., & Barberis, R. (2002). Distribution and mobility of metals in contaminated sites. Chemometric investigation of pollutant profiles. *Environmental Pollution*, *119*(2), 177-193.
8. Weaver, C. M., & Heaney, R. P. (Eds.). (2007). Calcium in human health. *Springer Science & Business Media*.
9. Carrier, J. C., & Evans, D. H. (1976). The role of environmental calcium in freshwater survival of the marine teleost, Lagodon rhomboides. *The Journal of Experimental Biology*, *65*(3), 529-538.
10. Wang, S., Forzani, E. S., & Tao, N. (2007). Detection of heavy metal ions in water by high-resolution surface plasmon resonance spectroscopy combined with anodic stripping voltammetry. *Analytical Chemistry*, *79*(12), 4427-4432.
11. Cherian, S., Gupta, R. K., Mullin, B. C., & Thundat, T. (2003). Detection of heavy metal ions using protein-functionalized microcantilever sensors. *Biosensors and Bioelectronics*, *19*(5), 411-416.

12. Hoang, C. V., Oyama, M., Saito, O., Aono, M., & Nagao, T. (2013). Monitoring the presence of ionic mercury in environmental water by plasmon-enhanced infrared spectroscopy. *Scientific Reports*, *3*.
13. Tokalioğlu, Ş., Kartal, Ş., & Elci, L. (2000). Determination of heavy metals and their speciation in lake sediments by flame atomic absorption spectrometry after a four-stage sequential extraction procedure. *Analytica Chimica Acta*, *413*(1), 33-40.
14. Faraji, M., Yamini, Y., Saleh, A., Rezaee, M., Ghambarian, M., & Hassani, R. (2010). A nanoparticle-based solid-phase extraction procedure followed by flow injection inductively coupled plasma-optical emission spectrometry to determine some heavy metal ions in water samples. *Analytica Chimica Acta*, *659*(1), 172-177.
15. Knopp, R., Scherbaum, F. J., & Kim, J. I. (1996). Laser induced breakdown spectroscopy (LIBS) as an analytical tool for the detection of metal ions in aqueous solutions. *Fresenius' Journal of Analytical Chemistry*, *355*(1), 16-20.
16. McComb, J. Q., Rogers, C., Han, F. X., & Tchounwou, P. B. (2014). Rapid screening of heavy metals and trace elements in environmental samples using portable X-ray fluorescence spectrometer, A comparative study. *Water, Air, & Soil Pollution*, *225*(12), 1-10.
17. Baysal, A., Ozbek, N., & Akman, S. (2013). Determination of Trace Metals in Waste Water and Their Removal Processes. *INTECH Open Access Publisher*.
18. Shtenberg, G., Massad-Ivanir, N., & Segal, E. (2015). Detection of trace heavy metal ions in water by nanostructured porous Si biosensors. *Analyst*, *140*(13), 4507-4514.
19. Li, M., Gou, H., Al-Ogaidi, I., & Wu, N. (2013). Nanostructured sensors for detection of heavy metals: a review. *ACS Sustainable Chemistry & Engineering*,*1*(7), 713-723.
20. Forzani, E. S., Zhang, H., Chen, W., & Tao, N. (2005). Detection of heavy metal ions in drinking water using a high-resolution differential surface plasmon resonance sensor. *Environmental science & technology*, *39*(5), 1257-1262.

21. Thundat, T., Brown, G. M., & Ji, H. F. (2005). Environmental monitoring using microcantilever sensors. In *ACS symposium series* (Vol. 904, pp. 284-305). *Oxford University Press.*
22. Szurdoki, F., Ren, D., & Walt, D. R. (2000). A combinatorial approach to discover new chelators for optical metal ion sensing. *Analytical chemistry*,*72*(21), 5250-5257.
23. Wang, J. (2001). Glucose biosensors: 40 years of advances and challenges. *Electroanalysis*, *13*(12), 983.
24. Taylor, R. F., & Schultz, J. S. (Eds.). (1996). Handbook of chemical and biological sensors. *CRC Press*.
25. Nomngongo, P. N., Ngila, J. C., Nyamori, V. O., Songa, E. A., & Iwuoha, E. I. (2011). Determination of selected heavy metals using amperometric horseradish peroxidase (HRP) inhibition biosensor. *Analytical Letters*, *44*(11), 2031-2046.
26. Borisov, S. M., & Wolfbeis, O. S. (2008). Optical biosensors. *Chemical reviews*,*108*(2), 423-461.
27. Huang, G. S., Wang, M. T., Su, C. W., Chen, Y. S., & Hong, M. Y. (2007). Picogram detection of metal ions by melanin-sensitized piezoelectric sensor. *Biosensors and Bioelectronics*, *23*(3), 319-325.
28. Malhotra, B. D., & Turner, A. (Eds.). (2003). Advances in biosensors: Perspectives in biosensors (Vol. 5). *Elsevier*.
29. Malhotra, B. D., Singhal, R., Chaubey, A., Sharma, S. K., & Kumar, A. (2005). Recent trends in biosensors. *Current Applied physics*, *5*(2), 92-97.
30. Beeby, S. (2004). MEMS mechanical sensors. *Artech House*.
31. Judy, J. W. (2001). Microelectromechanical systems (MEMS): fabrication, design and applications. *Smart Materials and Structures*, *10*(6), 1115.
32. Waggoner, P. S., & Craighead, H. G. (2007). Micro-and nanomechanical sensors for environmental, chemical, and biological detection. *Lab on a Chip*,*7*(10), 1238-1255.

33. Lavrik, N. V., Sepaniak, M. J., & Datskos, P. G. (2004). Cantilever transducers as a platform for chemical and biological sensors. *Review of Scientific Instruments*, *75*(7), 2229-2253.
34. Lindroos, V., Franssila, S., Tilli, M., Paulasto-Krockel, M., Lehto, A., Motooka, T., & Airaksinen, V. M. (Eds.). (2009). Handbook of silicon based MEMS materials and technologies. *Elsevier*.
35. Boisen, A., Dohn, S., Keller, S. S., Schmid, S., & Tenje, M. (2011). Cantilever-like micromechanical sensors. *Reports on Progress in Physics*, *74*(3), 036101.
36. Datar, R., Kim, S., Jeon, S., Hesketh, P., Manalis, S., Boisen, A., & Thundat, T. (2009). Cantilever sensors: nanomechanical tools for diagnostics. *Mrs Bulletin*,*34*(06), 449-454.
37. Lam, Y., Abu-Lail, N. I., Alam, M. S., & Zauscher, S. (2006). Using microcantilever deflection to detect HIV-1 envelope glycoprotein gp120.*Nanomedicine: Nanotechnology, Biology and Medicine*, *2*(4), 222-229.
38. Alodhayb, A., Brown, N., Rahman, S. S., Harrigan, R., & Beaulieu, L. Y. (2013). Towards detecting the human immunodeficiency virus using microcantilever sensors. *Applied Physics Letters*, *102*(17), 173106.
39. Zhang, Y., Venkatachalan, S. P., Xu, H., Xu, X., Joshi, P., Ji, H. F., & Schulte, M. (2004). Micromechanical measurement of membrane receptor binding for label-free drug discovery. *Biosensors and Bioelectronics*, *19*(11), 1473-1478.
40. Bashir, R., Hilt, J. Z., Elibol, O., Gupta, A., & Peppas, N. A. (2002). Micromechanical cantilever as an ultrasensitive pH microsensor. *Applied Physics Letters*, *81*(16), 3091-3093.
41. Senesac, L., & Thundat, T. G. (2008). Nanosensors for trace explosive detection. *Materials Today*, *11*(3), 28-36.
42. Álvarez, M., Carrascosa, L. G., Moreno, M., Calle, A., Zaballos, Á., Lechuga, L. M., Martínez-A, C., & Tamayo, J. (2004). Nanomechanics of the formation of DNA self-assembled monolayers and hybridization on microcantilevers. *Langmuir*,*20*(22), 9663-9668.

43. Yue, M., Stachowiak, J. C., Lin, H., Datar, R., Cote, R., & Majumdar, A. (2008). Label-free protein recognition two-dimensional array using nanomechanical sensors. *Nano Letters*, *8*(2), 520-524.

44. Ilic, B., Czaplewski, D., Zalalutdinov, M., Craighead, H. G., Neuzil, P., Campagnolo, C., & Batt, C. (2001). Single cell detection with micromechanical oscillators. *Journal of Vacuum Science & Technology B*, *19*(6), 2825-2828.

45. Chapman, P. J., Long, Z., Datskos, P. G., Archibald, R., & Sepaniak, M. J. (2007). Differentially ligand-functionalized microcantilever Arrays for metal ion identification and sensing. *Analytical chemistry*, *79*(18), 7062-7068.

46. Yoshikawa, G., Lang, H. P., Akiyama, T., Aeschimann, L., Staufer, U., Vettiger, P., Masakazu, A., & Gerber, C. (2009). Sub-ppm detection of vapors using piezoresistive microcantilever array sensors. *Nanotechnology*, *20*(1), 015501.

47. Yue, M., Lin, H., Dedrick, D. E., Satyanarayana, S., Majumdar, A., Bedekar, A. S., Jenkins, J., & Sundaram, S. (2004). A 2-D microcantilever array for multiplexed biomolecular analysis. *Microelectromechanical Systems, Journal of*, *13*(2), 290-299.

48. Tabard-Cossa, V., Godin, M., Burgess, I. J., Monga, T., Lennox, R. B., & Grütter, P. (2007). Microcantilever-based sensors: effect of morphology, adhesion, and cleanliness of the sensing surface on surface stress. *Analytical chemistry*, *79*(21), 8136-8143.

49. Godin, M., Williams, P. J., Tabard-Cossa, V., Laroche, O., Beaulieu, L. Y., Lennox, R. B., & Grütter, P. (2004). Surface stress, kinetics, and structure of alkanethiol self-assembled monolayers. *Langmuir*, *20*(17), 7090-7096.

50. Mertens, J., Calleja, M., Ramos, D., Tarýn, A., & Tamayo, J. (2007). Role of the gold film nanostructure on the nanomechanical response of microcantilever sensors. *Journal of Applied Physics*, *101*(3), 034904.

51. Lavrik, N. V., Tipple, C. A., Sepaniak, M. J., & Datskos, P. G. (2001). Enhanced chemi-mechanical transduction at nanostructured interfaces. *Chemical Physics Letters*, *336*(5), 371-376.

52. Kosaka, P. M., Tamayo, J., Ruz, J. J., Puertas, S., Polo, E., Grazu, V., Jesús, M., & Calleja, M. (2013). Tackling reproducibility in microcantilever biosensors: a statistical approach for sensitive and specific end-point detection of immunoreactions. *Analyst*, *138*(3), 863-872.

53. Bietsch, A., Zhang, J., Hegner, M., Lang, H. P., & Gerber, C. (2004). Rapid functionalization of cantilever array sensors by inkjet printing. *Nanotechnology*, *15*(8), 873.

54. Barnes, J. R., Stephenson, R. J., Woodburn, C. N., O'shea, S. J., Welland, M. E., Rayment, T., Gimzewski, J., & Gerber, C. (1994). A femtojoule calorimeter using micromechanical sensors. *Review of Scientific Instruments*, *65*(12), 3793-3798.

55. Berger, R., Gerber, C., Gimzewski, J. K., Meyer, E., & Güntherodt, H. J. (1996). Thermal analysis using a micromechanical calorimeter. *Applied Physics Letters*, *69*(1), 40-42.

56. Raiteri, R., Grattarola, M., Butt, H. J., & Skládal, P. (2001). Micromechanical cantilever-based biosensors. *Sensors and Actuators B: Chemical*, *79*(2), 115-126.

57. Vashist, S. K. (2007). A review of microcantilevers for sensing applications. *Journal of Nanotechnology*, *3*, 1-18.

58. Cha, B. H., Lee, S. M., Park, J. C., Hwang, K. S., Kim, S. K., Lee, Y. S., ... & Kim, T. S. (2009). Detection of Hepatitis B Virus (HBV) DNA at femtomolar concentrations using a silica nanoparticle-enhanced microcantilever sensor. *Biosensors and Bioelectronics*, *25*(1), 130-135.

59. Yang, Y. T., Callegari, C., Feng, X. L., Ekinci, K. L., & Roukes, M. L. (2006). Zeptogram-scale nanomechanical mass sensing. *Nano Letters*, *6*(4), 583-586.

60. Gupta, A., Akin, D., & Bashir, R. (2004). Single virus particle mass detection using microresonators with nanoscale thickness. *Applied Physics Letters*, *84*(11), 1976-1978.

61. Ilic, B., Craighead, H. G., Krylov, S., Senaratne, W., Ober, C., & Neuzil, P. J. (2004). Attogram detection using nanoelectromechanical oscillators. *Journal of Applied Physics*, *95*(7), 3694-3703.

62. Calleja, M., Tamayo, J., Johansson, A., Rasmussen, P., Lechuga, L. M., & Boisen, A. (2003). Polymeric cantilever arrays for biosensing applications. *Sensor Letters*, *1*(1), 20-24.

63. Tenje, M., Keller, S., Dohn, S., Davis, Z. J., & Boisen, A. (2010). Drift study of SU8 cantilevers in liquid and gaseous environments. *Ultramicroscopy*, *110*(6), 596-598.

64. Manning, K. Y., Butt, N. R., Alodhayb, A., Saika-Voivod, I., & Beaulieu, L. Y. (2013). Modeling the motion and detection of particles in microcantilever sensor cells. *Journal of Applied Physics*, *113*(11), 114501.

65. Carrascosa, L. G., Moreno, M., Álvarez, M., & Lechuga, L. M. (2006). Nanomechanical biosensors: a new sensing tool. *TrAC Trends in Analytical Chemistry*, *25*(3), 196-206.

66. Sadava, D. E., Hillis, D. M., Heller, H. C., & Berenbaum, M. (2009). Life: the science of biology (Vol. 2). *Macmillan*.

67. Hammond, K. S., Hollows, J. W., Townsend, C. R., & Lokman, P. M. (2006). Effects of temperature and water calcium concentration on growth, survival and moulting of freshwater crayfish, Paranephrops zealandicus. *Aquaculture*, *251*(2), 271-279.

68. Cairns, A., & Yan, N. (2009). A review of the influence of low ambient calcium concentrations on freshwater daphniids, gammarids, and crayfish. *Environmental Reviews*, *17*(NA), 67-79.

69. Jeziorski, A., Yan, N. D., Paterson, A. M., DeSellas, A. M., Turner, M. A., Jeffries, D. S., Keller, B., Weeber, S., McNicol, D., Palmer, M., McIver, K., Arseneau, K., Ginn, B., Cumming, B., & Smol, J. P. (2008). The widespread threat of calcium decline in fresh waters. *Science*, *322*(5906), 1374-1377.

70. Suzuki, K., Watanabe, K., Matsumoto, Y., Kobayashi, M., Sato, S., Siswanta, D., & Hisamoto, H. (1995). Design and synthesis of calcium and magnesium ionophores based on double-armed diazacrown ether compounds and their application to an ion

sensing component for an ion-selective electrode. *Analytical Chemistry*, *67*(2), 324-334.

71. Oh, B. K., Kim, C. Y., Lee, H. J., Rho, K. L., Cha, G. S., & Nam, H. (1996). One-component room temperature vulcanizing-type silicone rubber-based calcium-selective electrodes. *Analytical chemistry*, *68*(3), 503-508.
72. Vale. (2005). Long Harbour Commercial Nickel Processing Plant. *Environmental Impact Statement.*
73. Nolan, E. M., & Lippard, S. J. (2003). A "turn-on" fluorescent sensor for the selective detection of mercuric ion in aqueous media. *Journal of the American Chemical Society*, *125*(47), 14270-14271.
74. Blake, D. A., Jones, R. M., Blake, R. C., Pavlov, A. R., Darwish, I. A., & Yu, H. (2001). Antibody-based sensors for heavy metal ions. *Biosensors and Bioelectronics*, *16*(9), 799-809.
75. Oehme, I., & Wolfbeis, O. S. (1997). Optical sensors for determination of heavy metal ions. *Microchimica Acta*, *126*(3-4), 177-192.
76. Cammarata, R. C., & Sieradzki, K. (1994). Surface and interface stresses. *Annual Review of Materials Science*, *24*(1), 215-234.
77. Haiss, W. (2001). Surface stress of clean and adsorbate-covered solids. *Reports on Progress in Physics*, *64*(5), 591.
78. Bach, C. E., Giesen, M., Ibach, H., & Einstein, T. L. (1997). Stress relief in reconstruction. *Physical Review Letters*, *78*(22), 4225.
79. Berger, R., Delamarche, E., Lang, H. P., Gerber, C., Gimzewski, J. K., Meyer, E., & Güntherodt, H. J. (1997). Surface stress in the self-assembly of alkanethiols on gold. *Science*, *276*(5321), 2021-2024.
80. Pohl, K., Bartelt, M. C., De La Figuera, J., Bartelt, N. C., Hrbek, J., & Hwang, R. Q. (1999). Identifying the forces responsible for self-organization of nanostructures at crystal surfaces. *Nature*, *397*(6716), 238-241.
81. Besenbacher, F. (1996). Scanning tunnelling microscopy studies of metal surfaces. *Reports on Progress in Physics*, *59*(12), 1737.

82. Thayer, G. E., Bartelt, N. C., Ozolins, V., Schmid, A. K., Chiang, S., & Hwang, R. Q. (2002). Linking surface stress to surface structure: measurement of atomic strain in a surface alloy using scanning tunneling microscopy. *Physical Review Letters*, *89*(3), 036101.

83. Thompson, C. V., & Carel, R. (1996). Stress and grain growth in thin films. *Journal of the Mechanics and Physics of Solids*, *44*(5), 657-673.

84. Ibach, H. (1997). The role of surface stress in reconstruction, epitaxial growth and stabilization of mesoscopic structures. *Surface Science Reports*, *29*(5), 195-263.

85. Takeuchi, N., Chan, C. T., & Ho, K. M. (1991). Au (111): A theoretical study of the surface reconstruction and the surface electronic structure. *Physical Review B*, *43*(17), 13899.

86. Ocko, B. M., Gibbs, D., Huang, K. G., Zehner, D. M., & Mochrie, S. G. J. (1991). Structure and phases of the Au (001) surface: Absolute x-ray reflectivity. *Physical Review B*, *44*(12), 6429.

87. Bott, M., Hohage, M., Michely, T., & Comsa, G. (1993). Pt (111) reconstruction induced by enhanced Pt gas-phase chemical potential. *Physical Review Letters*,*70*(10), 1489.

88. Ledbetter, H., & Kim, S. (2001). Handbook of elastic properties of solids, liquids, and gases.

89. Gibbs, J. W. (1906). The scientific papers of J. Willard Gibbs (Vol. 1). *Longmans, Green and Company*.

90. Müller, P., Saùl, A., & Leroy, F. (2014). Simple views on surface stress and surface energy concepts. *Advances in Natural Sciences: Nanoscience and Nanotechnology*, *5*(1), 013002.

91. Shuttleworth, R. (1950). The surface tension of solids. *Proceedings of the Physical Society. Section A*, *63*(5), 444.

92. Sang, S., Zhao, Y., Zhang, W., Li, P., Hu, J., & Li, G. (2014). Surface stress-based biosensors. *Biosensors and Bioelectronics*, *51*, 124-135.

93. Butt, H. J. (1996). A sensitive method to measure changes in the surface stress of solids. *Journal of Colloid and Interface Science*, *180*(1), 251-260.

94. Ndieyira, J. W., Kappeler, N., Logan, S., Cooper, M. A., Abell, C., McKendry, R. A., & Aeppli, G. (2014). Surface-stress sensors for rapid and ultrasensitive detection of active free drugs in human serum. *Nature Nanotechnology*, *9*(3), 225-232.

95. Solomon, J. E., & Paul, M. R. (2006). The kinetics of analyte capture on nanoscale sensors. *Biophysical Journal*, *90*(5), 1842-1852.

96. Cherian, S., Mehta, A., & Thundat, T. (2002). Investigating the mechanical effects of adsorption of Ca^{2+} ions on a silicon nitride microcantilever surface. *Langmuir*, *18*(18), 6935-6939.

97. Fiorentini, V., Methfessel, M., & Scheffler, M. (1993). Reconstruction mechanism of fcc transition metal (001) surfaces. *Physical Review Letters*, *71*(7), 1051.

98. Ackland, G. J., & Finnis, M. W. (1986). Semi-empirical calculation of solid surface tensions in body-centred cubic transition metals. *Philosophical Magazine A*, *54*(2), 301-315.

99. Wasserman, H. J., & Vermaak, J. S. (1972). On the determination of the surface stress of copper and platinum. *Surface Science*, *32*(1), 168-174.

100. Needs, R. J., & Mansfield, M. (1989). Calculations of the surface stress tensor and surface energy of the (111) surfaces of iridium, platinum and gold. *Journal of Physics: Condensed Matter*, *1*(41), 7555.

101. Mays, C. W., Vermaak, J. S., & Kuhlmann-Wilsdorf, D. (1968). On surface stress and surface tension: II. Determination of the surface stress of gold. *Surface Science*, *12*(2), 134-140.

102. Dundon, M. L., & Mack Jr, E. (1923). The solubility and surface energy of calcium sulfate. *Journal of the American Chemical Society*, *45*(11), 2479-2485.

103. Milling, A. J. (Ed.). (1999). Surface characterization methods: principles, techniques, and applications (Vol. 87). *CRC Press*.

104. Stoney, G. G. (1909). The tension of metallic films deposited by electrolysis. *Proceedings of the Royal Society of London. Series A, Containing Papers of a Mathematical and Physical Character*, *82*(553), 172-175.

105. Godin, M., Tabard-Cossa, V., Grütter, P., & Williams, P. (2001). Quantitative surface stress measurements using a microcantilever. *Applied Physics Letters*, *79*(4), 551-553.

106. Raiteri, R., Butt, H. J., & Grattarola, M. (2000). Changes in surface stress at the liquid/solid interface measured with a microcantilever. *Electrochimica Acta*, *46*(2), 157-163.

107. Zhang, Y., Ren, Q., & Zhao, Y. P. (2004). Modelling analysis of surface stress on a rectangular cantilever beam. *Journal of Physics D: Applied Physics*, *37*(15), 2140.

108. Lachut, M. J., & Sader, J. E. (2012). Effect of surface stress on the stiffness of thin elastic plates and beams. *Physical Review B*, *85*(8), 085440.

109. Fritz, J., Baller, M. K., Lang, H. P., Rothuizen, H., Vettiger, P., Meyer, E., Güntherodt , H., Gerber, Ch., & Gimzewski, J. K. (2000). Translating biomolecular recognition into nanomechanics. *Science*, *288*(5464), 316-318.

110. Fang, W., & Wickert, J. A. (1996). Determining mean and gradient residual stresses in thin films using micromachined cantilevers. *Journal of Micromechanics and Microengineering*, *6*(3), 301.

111. Walmsley, B. A., Liu, Y., Hu, X. Z., Bush, M. B., Winchester, K. J., Martyniuk, M., Dell, M., & Faraone, L. (2005). Effects of deposition temperature on the mechanical and physical properties of silicon nitride thin films. *Journal of applied physics*, *98*(4), 044904.

112. Young, W. C., & Budynas, R. G. (2002). Roark's formulas for stress and strain (Vol. 7). *New York: McGraw-Hill*.

113. Godin, M. (2002). Surface stress, kinetics, and structure of alkanethiol self-assembled monolayers. *Ph.D. Thesis*, *McGill University*, Canada.

114. Da Silva, V. D. (2005). *Mechanics and strength of materials*. Springer Science & Business Media.

115. Ulman, A. (1996). Formation and structure of self-assembled monolayers. *Chemical reviews*, *96*(4), 1533-1554.

116. Love, J. C., Estroff, L. A., Kriebel, J. K., Nuzzo, R. G., & Whitesides, G. M. (2005). Self-assembled monolayers of thiolates on metals as a form of nanotechnology. *Chemical reviews*, *105*(4), 1103-1170.

117. Chaki, N. K., & Vijayamohanan, K. (2002). Self-assembled monolayers as a tunable platform for biosensor applications. *Biosensors and Bioelectronics*, *17*(1), 1-12.

118. Schaeferling, M., Schiller, S., Paul, H., Kruschina, M., Pavlickova, P., Meerkamp, M., Giammasi, C., & Kambhampati, D. (2002). Application of self-assembly techniques in the design of biocompatible protein microarray surfaces. *Electrophoresis*, *23*(18), 3097-3105.

119. Schreiber, F. (2004). Self-assembled monolayers: from'simple'model systems to biofunctionalized interfaces. *Journal of Physics: Condensed Matter*, *16*(28), R881.

120. Chaki, N. K., Aslam, M., Sharma, J., & Vijayamohanan, K. (2001). Applications of self-assembled monolayers in materials chemistry. *Journal of Chemical Sciences*, *113*(5-6), 659-670.

121. Tsukruk, V. V. (2001). Molecular Lubricants and Glues for Micro-and Nanodevices. *Advanced materials*, *13*(2), 95-108.

122. Cyr, D. M., Venkataraman, B., & Flynn, G. W. (1996). STM investigations of organic molecules physisorbed at the liquid-solid interface. *Chemistry of Materials*, *8*(8), 1600-1615.

123. Barth, J. V., Weckesser, J., Cai, C., Günter, P., Bürgi, L., Jeandupeux, O., & Kern, K. (2000). Building supramolecular nanostructures at surfaces by hydrogen bonding. *Angewandte Chemie International Edition*, *39*(7), 1230-1234.

124. Flink, S., van Veggel, F. C., & Reinhoudt, D. N. (2001). Functionalization of self-assembled monolayers on glass and oxidized silicon wafers by surface reactions. *Journal of Physical Organic Chemistry*, *14*(7), 407-415.

125. Poirier, G. E., & Pylant, E. D. (1996). The self-assembly mechanism of alkanethiols on Au (111). *Science*, *272*(5265), 1145-1148.

126. Schreiber, F. (2000). Structure and growth of self-assembling monolayers. *Progress in Surface Science*, *65*(5), 151-257.

127. Dubois, L. H., Zegarski, B. R., & Nuzzo, R. G. (1990). Fundamental studies of microscopic wetting on organic surfaces. 2. Interaction of secondary adsorbates with chemically textured organic monolayers. *Journal of the American Chemical Society*, *112*(2), 570-579.

128. Ludwig, R., & Dzung, N. T. K. (2002). Calixarene-based molecules for cation recognition. *Sensors*, *2*(10), 397-416.

129. Fenter, P., Eisenberger, P., Li, J., Camillone III, N., Bernasek, S., Scoles, G., Ramanarayanan, T., & Liang, K. S. (1991). Structure of octadecyl thiol self-assembled on the silver (111) surface: an incommensurate monolayer. *Langmuir*, *7*(10), 2013-2016.

130. Poirier, G. E. (1997). Mechanism of formation of Au vacancy islands in alkanethiol monolayers on Au (111). *Langmuir*, *13*(7), 2019-2026.

131. Dubois, L. H., & Nuzzo, R. G. (1992). Synthesis, structure, and properties of model organic surfaces. *Annual Review of Physical Chemistry*, *43*(1), 437-463.

132. Anselmetti, D., Baratoff, A., Güntherodt, H. J., Delamarche, E., Michel, B., Gerber, C., Kang, H., Wolf, H., & Ringsdorf, H. (1994). Domain and molecular superlattice structure of dodecanethiol self-assembled on Au (111). *EPL (Europhysics Letters)*, *27*(5), 365.

133. Strong, L., & Whitesides, G. M. (1988). Structures of self-assembled monolayer films of organosulfur compounds adsorbed on gold single crystals: electron diffraction studies. *Langmuir*, *4*(3), 546-558.

134. Yourdshahyan, Y., Zhang, H. K., & Rappe, A. M. (2001). n-alkyl thiol head-group interactions with the Au (111) surface. *Physical Review B*, *63*(8), 081405.

135. Hayashi, T., Morikawa, Y., & Nozoye, H. (2001). Adsorption state of dimethyl disulfide on Au (111): Evidence for adsorption as thiolate at the bridge site. *The Journal of Chemical Physics*, *114*(17), 7615-7621.

136. Schwartz, D. K. (2001). Mechanisms and kinetics of self-assembled monolayer formation. *Annual Review of Physical Chemistry*, *52*(1), 107-137.

137. Godin, M., Tabard-Cossa, V., Miyahara, Y., Monga, T., Williams, P. J., Beaulieu, L. Y., Lennox , R.,& Grutter, P. (2010). Cantilever-based sensing: the origin of surface stress and optimization strategies. *Nanotechnology*, *21*(7), 075501.

138. Chen, C. S., Chou, C. C., & Chang, S. W. (2013). Multiscale analysis of adsorption-induced surface stress of alkanethiol on microcantilever. *Journal of Physics D: Applied Physics*, *46*(3), 035301.

139. Huang, E., Zhou, F., & Deng, L. (2000). Studies of surface coverage and orientation of DNA molecules immobilized onto preformed alkanethiol self-assembled monolayers. *Langmuir*, *16*(7), 3272-3280.

140. Wu, G., Ji, H., Hansen, K., Thundat, T., Datar, R., Cote, R., Hagan, M., Chakraborty, A., & Majumdar, A. (2001). Origin of nanomechanical cantilever motion generated from biomolecular interactions. *Proceedings of the National Academy of Sciences*, *98*(4), 1560-1564.

141. Mertens, J., Rogero, C., Calleja, M., Ramos, D., Martín-Gago, J. A., Briones, C., & Tamayo, J. (2008). Label-free detection of DNA hybridization based on hydration-induced tension in nucleic acid films. *Nature Nanotechnology*, *3*(5), 301-307.

142. Watari, M., Galbraith, J., Lang, H. P., Sousa, M., Hegner, M., Gerber, C., Horton, M., & McKendry, R. A. (2007). Investigating the molecular mechanisms of in-plane mechanochemistry on cantilever arrays. *Journal of the American Chemical Society*, *129*(3), 601-609.

143. Beaulieu, L. Y., Godin, M., Laroche, O., Tabard-Cossa, V., & Grütter, P. (2007). A complete analysis of the laser beam deflection systems used in cantilever-based systems. *Ultramicroscopy*, *107*(4), 422-430.

144. Beaulieu, L. Y., Godin, M., Laroche, O., Tabard-Cossa, V., & Grütter, P. (2006). Calibrating laser beam deflection systems for use in atomic force microscopes and cantilever sensors. *Applied physics letters*, *88*(8), 083108.

145. Tabard-Cossa, V., Godin, M., Beaulieu, L. Y., & Grütter, P. (2005). A differential microcantilever-based system for measuring surface stress changes induced by electrochemical reactions. *Sensors and Actuators B: Chemical*, *107*(1), 233-241.

146. Mishra, R., Grange, W., & Hegner, M. (2011). Rapid and reliable calibration of laser beam deflection system for microcantilever-based sensor setups. *Journal of Sensors*, *2012*.

147. Peterson, J. P., & Peterson, R. B. (2006). Laser triangulation for liquid film thickness measurements through multiple interfaces. *Applied Optics*, *45*(20), 4916-4926.

148. Dohn, S., Greve, A., Svendsen, W. E., & Boisen, A. (2010). The influence of refractive index change and initial bending of cantilevers on the optical lever readout method. *Review of Scientific Instruments*, *81*(6), 065104.

149. Láng, G. G., & Seo, M. (2000). On the electrochemical applications of the bending beam method. *Journal of Electroanalytical Chemistry*, *490*(1), 98-101.

150. Láng, G. G., & Barbero, C. A. (2012). Optical Detection of the Deformation. In*Laser Techniques for the Study of Electrode Processes* (pp. 75-113). Springer Berlin Heidelberg.

151. Rokob, T. A., & Láng, G. G. (2005). Remarks on the electrochemical application of optical methods for the determination of stress in electrodes. *Electrochimica Acta*, *51*(1), 93-97.

152. Xiao, X., & Schleh, D. (2010). Refractive error correction for in situ curvature measurement using laser beam deflection method. *Journal of Applied Physics*, *107*(1), 013508.

153. Putman, C. A., De Grooth, B. G., Van Hulst, N. F., & Greve, J. (1992). A detailed analysis of the optical beam deflection technique for use in atomic force microscopy. *Journal of Applied Physics*, *72*(1), 6-12.

154. Huber, F., Lang, H. P., Backmann, N., Rimoldi, D., & Gerber, C. (2013). Direct detection of a BRAF mutation in total RNA from melanoma cells using cantilever arrays. *Nature nanotechnology*, *8*(2), 125-129.

155. Chapman, B. (1980). Glow discharge processes: sputtering and plasma etching. *Wiley-Inter Science*.

156. Binnig, G., & Rohrer, H. (2000). Scanning tunneling microscopy. *IBM Journal of Research and Development*, *44*(1/2), 279.

157. Binnig, G., Quate, C. F., & Gerber, C. (1986). Atomic force microscope. *Physical Review Letters*, *56*(9), 930.

158. Magonov, S. N., & Whangbo, M. H. (2008). Surface analysis with STM and AFM: experimental and theoretical aspects of image analysis. *John Wiley & Sons*.

159. Yang, C. W., Hwang, S., Chen, Y. F., Chang, C. S., & Tsai, D. P. (2007). Imaging of soft matter with tapping-mode atomic force microscopy and non-contact-mode atomic force microscopy. *Nanotechnology*, *18*(8), 084009.

160. Cleveland, J. P., Manne, S., Bocek, D., & Hansma, P. K. (1993). A nondestructive method for determining the spring constant of cantilevers for scanning force microscopy. *Review of Scientific Instruments*, *64*(2), 403-405.

161. Gibson, C. T., Weeks, B. L., Lee, J. R., Abell, C., & Rayment, T. (2001). A nondestructive technique for determining the spring constant of atomic force microscope cantilevers. *Review of Scientific Instruments*, *72*(5), 2340-2343.

162. Gutsche, C. D. (2008). Calixarenes: an introduction. *Royal Society of Chemistry*.

163. Mokhtari, B., Pourabdollah, K., & Dalali, N. (2011). Molecule and ion recognition of nano-baskets of calixarenes since 2005. *Journal of Coordination Chemistry*, *64*(5), 743-794.

164. Kim, H. J., Lee, M. H., Mutihac, L., Vicens, J., & Kim, J. S. (2012). Host–guest sensing by calixarenes on the surfaces. *Chemical Society Reviews*, *41*(3), 1173-1190.

165. Alodhayb, A., Rahman, S. S., Rahman, S., Valluru, G. K., Georghiou, P. E., & Beaulieu, L. Y. (2014). Detection of calcium ions using gold-coated micro-cantilever

sensors using upper-and lower-rim functionalized calix [4] arenes. *Sensors and Actuators B: Chemical*, 203, 766-773.

166. Arora, V., Chawla, H. M., & Singh, S. P. (2007). Calixarenes as sensor materials for recognition and separation of metal ions. *Arkivoc*, *2*, 172-200.

167. Ishikawa, Y., Kunitake, T., Matsuda, T., Otsuka, T., & Shinkai, S. (1989). Formation of calixarene monolayers which selectively respond to metal ions. *Journal of the Chemical Society, Chemical Communications*, (11), 736-738.

168. Ikeda, A., & Shinkai, S. (1997). Novel cavity design using calix [n] arene skeletons: toward molecular recognition and metal binding. *Chemical reviews*, *97*(5), 1713-1734.

169. Asfari, M. Z., Böhmer, V., Harrowfield, J., & Vicens, J. (Eds.). (2007). Calixarenes 2001. *Springer Science & Business Media*.

170. Steed, J. W., Turner, D. R., & Wallace, K. (2007). Core concepts in supramolecular chemistry and nanochemistry. *John Wiley & Sons*.

171. Georghiou, P. E., Rahman, S., Valluru, G., Dawe, L. N., Rahman, S. S., Alodhayb, A. N., & Beaulieu, L. Y. (2013). Synthesis of an upper-and lower-rim functionalized calix [4] arene for detecting calcium ions using a microcantilever sensor. *New Journal of Chemistry*, *37*(5), 1298-1301.

172. Valluru, G., Rahman, S., Georghiou, P. E., Dawe, L. N., Alodhayb, A. N., & Beaulieu, L. Y. (2014). Synthesis of a cone-conformer bimodal calix [4] arene-crown-5 which forms a sensitive cesium ion sensing layer on gold-coated microcantilevers. *New Journal of Chemistry*, *38*(12), 5868-5872.

173. Grönbeck, H., Curioni, A., & Andreoni, W. (2000). Thiols and disulfides on the Au (111) surface: The headgroup-gold interaction. *Journal of the American Chemical Society*, *122*(16), 3839-3842.

174. Pensa, E., Cortés, E., Corthey, G., Carro, P., Vericat, C., Fonticelli, M. H., Benítez, G., Rubert, A., & Salvarezza, R. C. (2012). The chemistry of the sulfur–gold interface: in search of a unified model. *Accounts of Chemical Research*, *45*(8), 1183-1192.

175. Fischer, J. A., Zoldan, V. C., Benitez, G., Rubert, A. A., Ramirez, E. A., Carro, P., Salvarezza , R., Pasa, A., & Vela, M. E. (2012). Sulfidization of Au (111) from Thioacetic Acid: An Experimental and Theoretical Study. *Langmuir*, *28*(43), 15278-15285.

176. Kern, W. (1993). Handbook of semiconductor wafer cleaning technology. *New Jersey: Noyes Publication*, 111-196.

177. Pan, G. B., Bu, J. H., Wang, D., Liu, J. M., Wan, L. J., Zheng, Q. Y., & Bai, C. L. (2003). Adlayer structures of calixarenes on Au (111) surface studied with STM. *The Journal of Physical Chemistry B*, *107*(47), 13111-13116.

178. Calleja, M., Kosaka, P. M., San Paulo, Á., & Tamayo, J. (2012). Challenges for nanomechanical sensors in biological detection. *Nanoscale*, *4*(16), 4925-4938.

179. Genorio, B., He, T., Meden, A., Polanc, S., Jamnik, J., & Tour, J. M. (2008). Synthesis and self-assembly of thio derivatives of calix [4] arene on noble metal surfaces. *Langmuir*, *24*(20), 11523-11532.

180. Hayden, V. C., Rahman, S. S., & Beaulieu, L. Y. (2013). Computational analysis of the effect of surface roughness on the deflection of a gold coated silicon micro-cantilever. *Journal of Applied Physics*, *113*(5), 054501.

181. Zhao, Y. (2014). Surface stress detection and mechanism study with microcantilever based sensor for biomolecular monolayers. *Graduate Theses and Dissertations. Paper 13690*. http://lib.dr.iastate.edu/etd/13690.

182. Desikan, R., Lee, I., & Thundat, T. (2006). Effect of nanometer surface morphology on surface stress and adsorption kinetics of alkanethiol self-assembled monolayers. *Ultramicroscopy*, *106*(8), 795-799.

183. Ayoub, S., & Beaulieu, L. Y. (2013). The surface morphology of thin Au films deposited on Si (001) substrates by sputter deposition. *Thin Solid Films*, *534*, 54-61.

184. Beckett, G. J., Walker, S. W., & Rae, P. W. H. (1998). Lecture notes on clinical biochemistry (pp. 15-34). *Edinburgh: Blackwell Science*.

185. Ji, H. F., & Thundat, T. (2002). In situ detection of calcium ions with chemically modified microcantilevers. *Biosensors and Bioelectronics*, *17*(4), 337-343.

186. Ji, H. F., Finot, E., Dabestani, R., Thundat, T., Brown, G. M., & Britt, P. F. (2000). A novel self-assembled monolayer (SAM) coated microcantilever for low level caesium detection. *Chemical Communications*, (6), 457-458.

187. Zhang, X., Yang, M., Vafai, K., & Ozkan, C. S. (2003). Design and analysis of microcantilevers for biosensing applications. *Journal of the Association for Laboratory Automation*, *8*(2), 90-93.

188. McKendry, R., Zhang, J., Arntz, Y., Strunz, T., Hegner, M., Lang, H. P., Baller, M., Certa, U., Meyer, E., Güntherodt, H., & Gerber, C. (2002). Multiple label-free biodetection and quantitative DNA-binding assays on a nanomechanical cantilever array. *Proceedings of the National Academy of Sciences*, *99*(15), 9783-9788.

189. Sleem, H. F., Dawe, L. N., & Georghiou, P. E. (2012). A tetraamido isophthaloyl-based macrocyclic calcium chloride and strontium chloride tritopic receptor. *New Journal of Chemistry*, *36*(12), 2451-2455.

190. Howe, E. N., Bhadbhade, M., & Thordarson, P. (2014). Cooperativity and complexity in the binding of anions and cations to a tetratopic ion-pair host. *Journal of the American Chemical Society*, *136*(20), 7505-7516.

191. Rai, A., Singh, A., Ahmad, A., & Sastry, M. (2006). Role of halide ions and temperature on the morphology of biologically synthesized gold nanotriangles. *Langmuir*, *22*(2), 736-741.

192. Molecular modeling calculations on the anions were determined using Spartan'10 software by Wavefunction, Inc. Irvine, CA, USA.

193. Steed, J. W., & Atwood, J. L. (2013). Supramolecular chemistry. *John Wiley & Sons*.

194. Patra, S., Maity, D., Gunupuru, R., Agnihotri, P., & Paul, P. (2012). Calixarenes: Versatile molecules as molecular sensors for ion recognition study. *Journal of Chemical Sciences*, *124*(6), 1287-1299.

195. Çiçek, B., & Yıldız, A. (2011). Synthesis, metal ion complexation and computational studies of thio oxocrown ethers. *Molecules*, *16*(10), 8670-8683.

196. Ivan, I. A., Ardeleanu, M., & Laurent, G. J. (2012). High dynamics and precision optical measurement using a position sensitive detector (PSD) in reflection-mode: application to 2D object tracking over a smart surface. *Sensors*, *12*(12), 16771-16784.

197. Sader, J. E., Larson, I., Mulvaney, P., & White, L. R. (1995). Method for the calibration of atomic force microscope cantilevers. *Review of Scientific Instruments*, *66*(7), 3789-3798.

198. Miyatani, T., & Fujihira, M. (1997). Calibration of surface stress measurements with atomic force microscopy. *Journal of Applied Physics*, *81*(11), 7099-7115.

199. Auernhammer, G., Butt, H. J., & Vollmer, D. (Eds.). (2008). Surface and interfacial forces-from fundamentals to applications (Vol. 134). *Springer*.

200. Holbery, J. D., & Eden, V. L. (2000). A comparison of scanning microscopy cantilever force constants determined using a nanoindentation testing apparatus. *Journal of Micromechanics and Microengineering*, *10*(1), 85.

201. Hamilton, G. R., Sahoo, S. K., Kamila, S., Singh, N., Kaur, N., Hyland, B. W., & Callan, J. F. (2015). Optical probes for the detection of protons, and alkali and alkaline earth metal cations. *Chemical Society Reviews*.

202. Valluru, G. (2015). Synthesis and applications of some upper- and lower-rim functionalized calix[4]arenes and calix[4]naphthalene derivatives. *Ph.D. Thesis*, *Memorial University*, Canada.

203. Loizeau, F., Akiyama, T., Gautsch, S., Vettiger, P., Yoshikawa, G., & de Rooij, N. F. (2015). Comparing membrane-and cantilever-based surface stress sensors for reproducibility. *Sensors and Actuators A: Physical*, *228*, 9-15.

204. Sliwa, W., & Deska, M. (2011). Functionalization reactions of calixarenes. *Arkivoc*, *1*, 496-551.

205. Jain, A. K., Gupta, V. K., & Raisoni, J. R. (2004). Strontium (II)-selective potentiometric sensor based on ester derivative of 4-tert-butylcalix (8) arene in PVC matrix. *Sensors*, *4*(8), 115-124.